Mechanical Properties of Extrusion-Based Additive Manufacturing of Shape Memory Polymers

by

Danesh Zonoobi

A thesis submitted in partial fulfillment of the requirements for the degree of

Master of Science

Department of Mechanical Engineering
University of Alberta

Abstract

Extrusion-Based Additive Manufacturing (EBAM), also known as Fused Deposition Modeling (FDM) or three-dimensional (3D) printing, is a manufacturing technique in which a desired object is formed by repetitive process of extrusion and deposition of thin layers of molten material through a nozzle in different paths in a selective manner. Availability of low cost EBAM devices plus versatility of materials that can be manufactured by EBAM lead to exponential growth of EBAM in numerous applications. Among the materials that can be used in EBAM, shape memory polymers (SMPs) are in spotlight due to their unique ability to return from a deformed state to their original shape with an external stimulus. Manufacturing of SMP objects through an EBAM process, also known as four dimensional (4D) printing, has a great potential for different applications; however, mechanical properties of SMP end-products manufactured by EBAM need to be thoroughly analyzed before any functional application can be developed.

This thesis investigates and reports the mechanical properties of SMP end-products manufactured by EBAM. The effects of major printing parameters (print orientation and infill percentage) on five mechanical properties, namely, elastic modulus, yield strength, maximum elongation, resilience and toughness are investigated.

Additionally, an analytical model based on Classical Laminated Plate Theory (CLPT) was used in order to predict the elastic modulus of EBAM parts. Predicted results of the model are compared with the experimental results. Due to the poor agreement between predicted and experimental data in some cases, a modified model is developed that matches the experimental results with less than 5% difference.

Keywords: extrusion-based additive manufacturing, fused deposition modelling, mechanical properties, shape memory polyurethanes, smart materials, 3D printing, raster angle, infill percentage.

Preface

This thesis is an original work by 'Danesh Zonobi'. No part of this thesis has been previously published.

Acknowledgements

Working in this thesis has been a wonderful as well as challenging experience, which would not have been possible without the guidance and support of many different people around me.

First of all, I would like to thank Dr. Ben Jar for his mentorship throughout this project, for being patient with me and for trusting my abilities to overcome any challenges that appeared through this project.

I would like to thank my family for always being there for me and their unconditional moral support.

I would like to thank Irina Garces, for the help and advice that they provided in experimental setups.

Table of Contents

List of Tables

List of Figures

List of Symbols

CC_{SSD} sum of squared differences (SSD) correlation coefficient

E elastic modulus (Young's modulus)

E_1 longitudinal elastic modulus of a single layer

E_2 lateral elastic modulus of a single layer

E_b elastic modulus of extruded beads

E_w elastic modulus of the weak phase

E_w^{mod} modified elastic modulus of the weak phase

$EL\%$ maximum elongation

G_w shear modulus of extruded beads

G_w shear modulus of the weak phase

G_{12} in-plane shear modulus

h total thickness

h_l layer thickness

$I(x, y)$ intensity of the image at location x, y

k index of ply

M applied moments

N applied force

n	total number of plies
Q	stiffness matrix of a single layer
U_r	elastic deformation energy (resilience)
U_T	total deformation energy (toughness)
v_b	volume fraction of extruded beads
v_w	volume fraction of the weak phase
$\bar{Q}$	transformed reduced stiffness matrix
$\Delta\nu$	compensation parameter for Poisson's ratio
$\Delta\theta$	difference between raster angles of neighboring layers
ϵ^0	mid-plane strain
κ	mid-plane curvature
λ	scaling factor between 0 and 1
ν	material Poisson's ratio
ν_{12}	major Poisson's ratio
ν_{12}^{mod}	modified Poisson's ratio
$\Phi(\cdot)$	scaling function between 0 and 1
$\Psi_E(\cdot)$	compensation function of E_w
$\Psi_G(\cdot)$	compensation function of G_w
σ_y	yield strength
θ_k	raster angle of the k-th layer

Glossary of Terms

AM Additive Manufacturing.

CAD Computer Aided Design.

CC Cross Correlation.

CLPT Classical Laminated Plate Theory.

CPT Classical Plate Theory.

DIC Digital Image Correlation.

EBAM Extrusion-based Additive Manufacturing.

FDM Fused Deposition Modeling.

ROI Region of Interest.

SMP Shape Memory Polymer.

SSD Sum of squared differences.

Chapter 1

Introduction

1.1 Motivation

Additive manufacturing (AM) is a manufacturing technique in which products are built by continuously adding and/or fusing material layer by layer [1]. extrusion-based additive manufacturing (EBAM), which is also known as fused deposition modeling (FDM), or 3D printing, is one of the most common AM methods. In this method semi molten polymeric materials is extruded and selectively dispensed through a nozzle onto a platform layer by layer [2].

EBAM was first developed as a cost-effective rapid prototyping technology in order to fabricate prototypes for product development within industry [3]. However, due to the recent improvements in this technique, fabrication of functional parts using EBAM is gaining interest in different fields [4, 5]. Moreover, over the past few years, the range of materials manufactured by EBAM method has increased by a large extent. Shape memory polymers (SMP) are among the materials that has been in the spotlight recently [6]. SMPs are polymers that can rapidly change their shape from a temporary form to their original form [7]. Such polymers are stimuli-responsive which means that shape recovery occurs upon exposure to external stimuli such as heat. Hence, SMPs can be categorized according to the type of external stimuli that trigger the shape recovery process [8]. Thermo-responsive SMPs are among the most common types of SMPs [9], which offer enormous advantages including high strain

recovery, lightweight, low cost, good controllability over the recovery temperature and simple procedure for programming of shapes [6, 10]. These characteristics motivates use of SMP parts produced by EBAM in a range of scientific studies [6, 9–11].

In order to design and create a viable functional end-product using EBAM method with SMPs, it is crucial to have a deep understanding of mechanical behaviour of fabricated part. Thus, in this thesis a set of experiments are designed to investigate and characterize the mechanical behaviour of a SMPs produced by EBAM with respect to fabrication parameters.

Moreover, analytical analysis of mechanical behaviour of EBAM parts is included since the experimental approach is not always the best answer to achieve a general understanding of mechanical behaviour of materials. This is due to the benefits that analytical approach offers compared to experimental approach. First of all, the experimental investigation process is time consuming and it requires a significant amount of effort to be devoted on that. Secondly, experimental setups are often expensive and obtaining meaningful experimental results is generally costly and challenging. In addition, with experimental data, it is often difficult to extrapolate the behaviour of the product under different circumstances [12]. These benefits, motivates inclusion of an analytical model based on classical laminated plate theory (CLPT), in addition to experimental investigations, in order to predict the mechanical behaviour of the specimens.

1.2 Thesis Objectives

In this thesis consistent SMP samples with EBAM technique are created for investigating the influence of raster angle and infill percentage on mechanical properties of these samples. The specimens are tested at three different infill percentage levels: 85%, 100% and 115%. At 115% infill level, 0° and 90° raster angles are investigated. At 85% and 100% infill levels, 30° and 60° raster angles are investigated in addition to 0° and 90° due to the increased sensitivity of mechanical properties to the raster angle

at these infill percentages. The mechanical properties examined are elastic modulus, yield strength, maximum elongation, modulus of resilience and tensile toughness. The objectives of experimental investigation are:

- To provide a general understanding of mechanical behaviour of the SMP samples made with EBAM method.
- To extend the knowledge on the influence of two main fabrication parameters, raster angle and infill percentage, on mechanical properties of SMP parts.
- To provide suggestions on the suitable combination of raster angle and infill percentage for different applications.

In addition, elastic modulus of the SMP samples produced by EBAM is investigated analytically. First, the applicability of CLPT was investigated to the produced samples. Later, a modified CLPT model was proposed and discussed.

1.3 Thesis Outline

This thesis is organized into five chapters. Chapter 2 describes a brief background on the extrusion-based additive manufacturing (EBAM), shape memory polymers (SMPs), classical laminated plate theory (CLPT) and the procedures required to produce the test samples in this thesis. In Chapter 3, a set of experiments are designed to investigate mechanical behaviour of EBAM parts with respect to raster angle and infill percentage. Experimental results and observations on mechanical properties including elastic modulus, yield strength, maximum elongation, modulus of resilience and tensile toughness are reported in this chapter. Chapter 4 describes the utilization of an analytical model based on CLPT to predict the elastic modulus of EBAM end-parts. Also, the predicted values are compared to the experimental results of Chapter 3 to examine the accuracy of the model. Some empirical modifications are suggested for CLPT model of SMP material to improve the predictions. Finally, a

brief conclusion on the entire thesis, together with promising future research directions are presented in Chapter 5.

Chapter 2

Background

This chapter provides a brief overview of extrusion-based additive manufacturing (EBAM) system followed by the procedures required to produce the test samples from shape memory polymer pellets in this thesis. Additionally, a brief introduction to some concepts used in this thesis such as digital image correlation is presented. At the end, recent related works in EBAM of SMPs are reviewed and the gap in the research is highlighted.

2.1 Extrusion-Based Additive Manufacturing

2.1.1 Description

Extrusion-based additive manufacturing (EBAM), also known as fused deposition modeling (FDM)[1], is an additive manufacturing (AM) process which is most commonly known as "3D printing". In this method semi molten material is extruded and dispensed through a nozzle in a selective manner [2]. EBAM was first developed in the 1980's as a cost-effective rapid prototyping technology in order to fabricate prototypes and basic representation of product development within industry [3]. However, due to the recent improvements including reduced cost and manufacturing time as well as higher quality parts produced by this technique, fabrication of functional end-products using EBAM is gaining interest in different fields [4, 5]. The main advantage

[1]Other commonly used names are: fused layer manufacturing (FLM), fused filament fabrication (FFF), modeling extrusion (ME) and fused layer manufacturing (FLM).

of this manufacturing technique is the capability of EBAM to produce highly engineered parts with complex geometry [6]. Moreover, no costly molds are required in this method which means that a digital design can turn into a physical end-product in a matter of hours. This also enables manufacturers to produce customizable parts.

2.1.2 EBAM Manufacturing Procedure

First step in EBAM manufacturing procedure is creating a digitally designed model. The digital model is mainly produced with the help of a 3D computer aided design (CAD) software[2]. Nowadays, designing a digital model is a relatively easy task, thanks to the availability of numerous CAD software which are becoming more prevalent and easy to use.

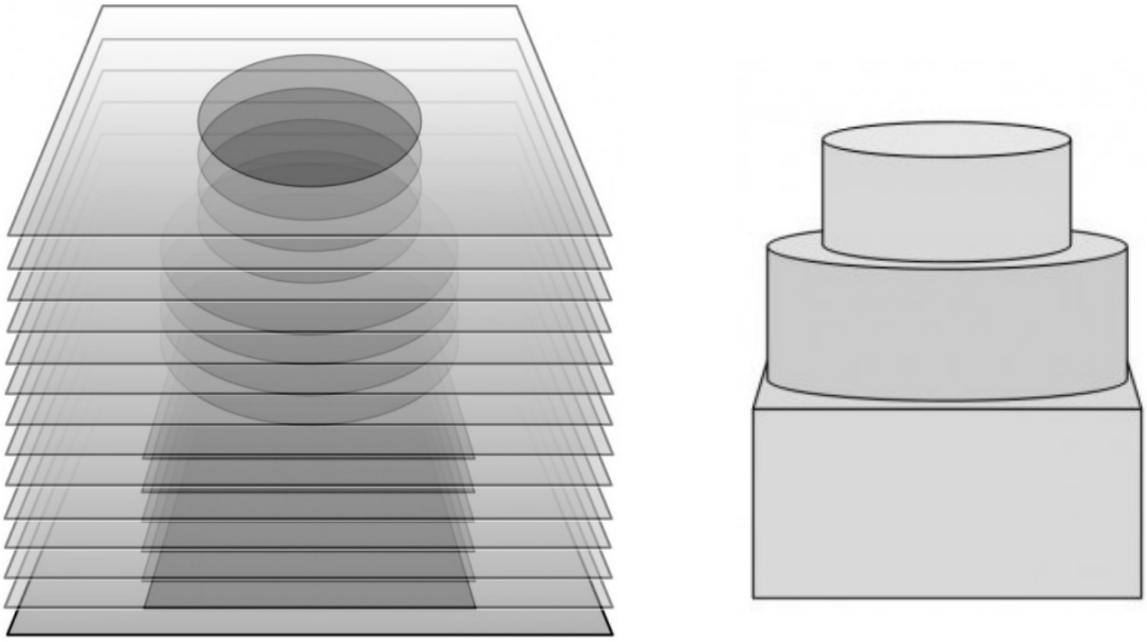

Figure 2.1: Slicing process transforms an object (right) to a series of thin layers (left).

Then the 3D model, needs to be sectioned into thin cross-sectional layers in a horizontal plane as shown in Figure 2.1. The process of dividing a model into horiz ontal layers is known as "slicing". Slicing process also defines the extrusion path which

[2]For EBAM, digital model is required to be in STL file format which describes the external closed surface of the digital model

forms the cross-sectional layers. There are numerous slicing software available for EBAM such as Cura[14], Simplify 3D[15] and Slic3r[16]. Each slicing software has different slicing parameters to provide users with control over the slicing process. Common parameters available in most of slicing software are [2]: layer thickness/height, nozzle diameter or bead width, flow rate, deposition speed, infill percentage, raster orientation/angle, raster pattern, air gaps (raster to raster, perimeter to raster), number of contours/perimeters, contour width, top thickness, bottom thickness; extrusion temperature, bed or platform temperature and building orientation. Figure 2.2 shows the schematic illustration of some of these parameters.

Each of the slicing parameters mentioned above does affect the mechanical behaviour of the resultant EBAM end-part. However, the impact over the mechanical properties of the product is not equal among all slicing parameters. Hence, most of the studies on this matter are mainly focused on some of the key parameters such as layer thickness/height, infill, raster orientation/angle, raster pattern, air gaps and building orientation [2].

Beside the slicing parameters, one of the most important factors in the EBAM process is the manufacturing material. In this thesis, a shape memory polymer called MM4520 is used. A brief background on shape memory materials in general and MM4520 in particular are presented in the following section.

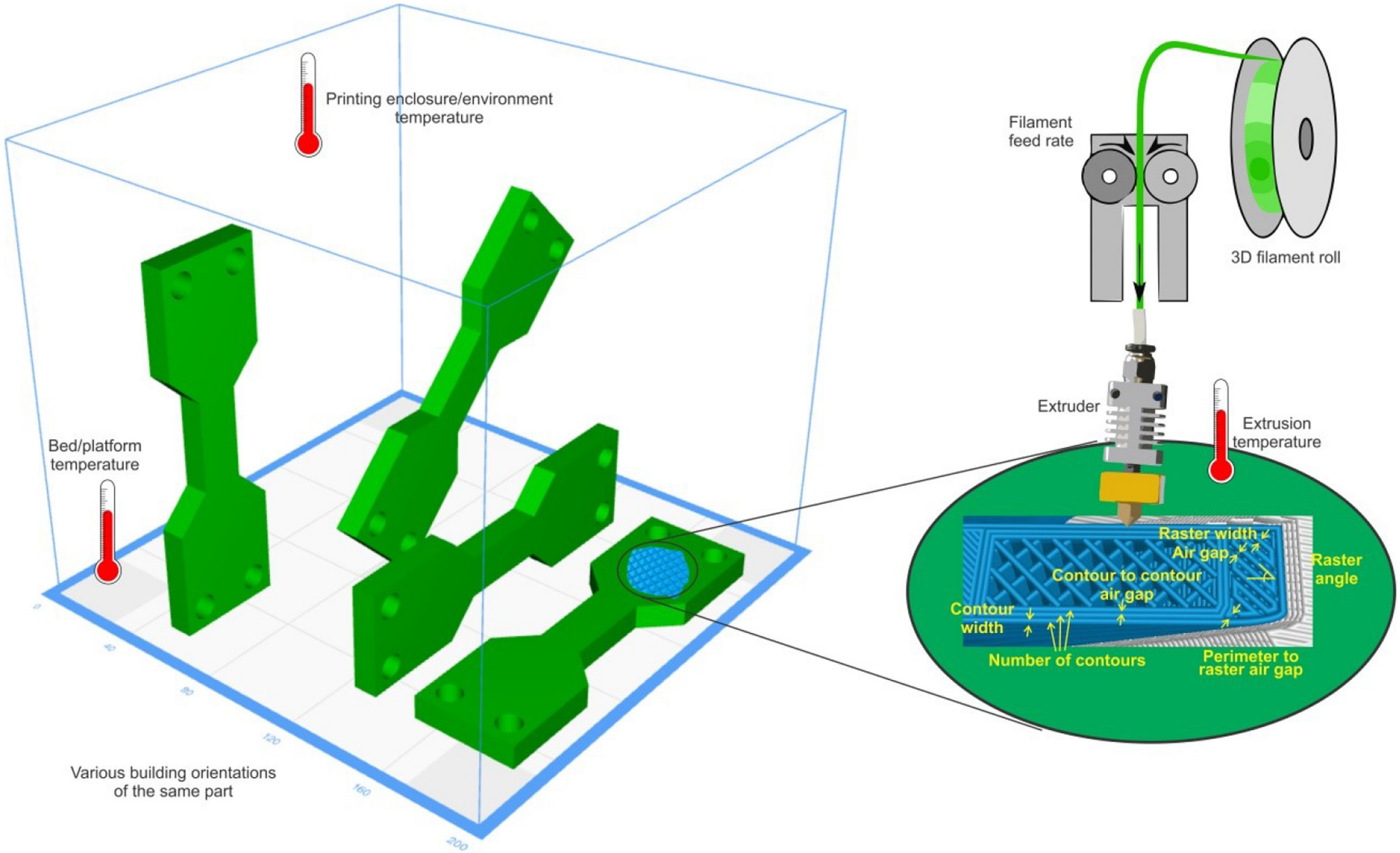

Figure 2.2: A schematic illustration of slicing parameters [13].

2.2 Shape Memory Polymers

Shape memory polymers (SMPs) represent a class of smart materials that can recover deformation and/or apply force in response to an stimulus. In other words, SMPs can change their shape from a temporary form to their original form [7]. Due to this unique behaviour, these polymers are commonly known to be able to "memorize" a permanent shape. The first publication mentioning the phrase "shape memory" effects in polymers is due to L. B. Vernon in 1941 in a United States patent [17] which claimed a material made of methacrylic acid ester resin has an "elastic memory". It was used for dental purposes and could recover its original shape upon heating. After that, the use of SMPs continued to grow in a number of publications with different applications. The physical properties of the material which is used for this purpose has a tremendous influence on the production. As a result, dozens of polymers have been designed to demonstrate shape-memory properties for diverse applications areas ranging from outer space and morphing aircraft systems to biomedical devices [18–21]. Nowadays such polymers are commercially available and widely used [19]. Consequently, there has been a significant increase in investigation of variety of materials and several promising shape memory effects have been developed over the past decade [22–24].

SMPs are stimuli-responsive which means that shape recovery occurs upon exposure to external stimuli such as heat, electricity, stress, light, moisture, solvent, etc. Hence, SMPs can be categorized according to the type of external stimuli that trigger the shape recovery process [8]. Thermo-responsive shape memory polymers are among the most common types of SMPs which respond to heat as a stimuli [9]. The permanent shape of a thermo-responsive thermoplastic SMP is assigned during the manufacturing processes such as EBAM, electro spinning or melt electro spinning. Using extrusion-based additive manufacturing (EBAM) as a production technique for thermo-responsive SMPs lead to an innovative concept of production technology

known as 4D printing [6]. Skylar Tibbits[25] introduced the term "4D printing" for the first time in his TED conference talk [6]. While in EBAM, static structures are produced from a digital model in 3 dimensional coordinates, 4D printing (EBAM with SMPs) adds the potential of the change in the produced structure over time as the fourth dimension [6]. As mentioned above, this process depends on environmental stimuli.

The SMP used in this thesis is a semi-crystalline thermoplastic polyurethane shape memory polymer (MM4520) which is purchased from SMP Technologies Inc., Japan. The manufacturer specified glass transition temperature is 45 C° [26].

Since raw material was received in the form of pellets, a manufacturing process was needed to transfer the raw material into the filaments in order to be fed into the EBAM machine. The process of polymer extrusion from pellets, used in this thesis, is described next.

It is known that polyurethane SMPs absorb humidity and thus the water absorbed in polyurethane SMPs may cause bubbles in the extruded filaments [28]. Hence, in the first step, the pellets were dried in a vacuum oven[3] according to the procedure presented in [29]. This step prevents bubbles from forming inside the filament. After the drying process, polymer extrusion process was started. This process consists of five stages which are feeding, melting, shaping, cooling and winding. Figure 2.3 shows the filament extrusion production line setup in the laboratory. As it is shown in Figure 2.4 (top), a single screw extruder (C.W. Brabender Instruments, Inc.) attached to a drive system is used to extrude filaments.

In the first stage the raw polymer is placed in a hopper which feeds the barrel of the extruder. This stage is called feeding stage. Next stage is melting which occurs in the extruder. The extruder has four continuous heating zones as shown in Figure 2.4 (bottom). The pellets are added into the hopper which is placed on top of a rotating screw. With the rotation of the screw, the material gradually melts as it is pushed

[3]Thermo Scientific, Lindberg Blue.

towards the subsequent zones in the melting barrel.

Temperature of these sequential heating zones are controlled independently to maintain the advancement of the polymer down the barrel with a constant rate. The third stage is the shaping stage. At this stage the molten polymer is forced through a die. In this thesis, a 3 mm diameter die is used.

The material that is exiting the die, extrudate, enters the cooling stage. In the cooling stage, different cooling mechanisms can be used to decrease the temperature of the product. The most common ones used in industry are temperature controlled water baths, forced air cooling and cooling rolls. At the beginning of the cooling procedure water spray is used and after that, the filament is cooled down by temperature controlled water bath at 25°C. At the end of the procedure, there is a roller on which the filament is wound through a pulling mechanism. The pulling mechanism provides a constant take-up speed (2.8 meters per minute) to the filament that ensures the consistency of the diameter of the filament and prevents formation of any air bubble before complete cooling.

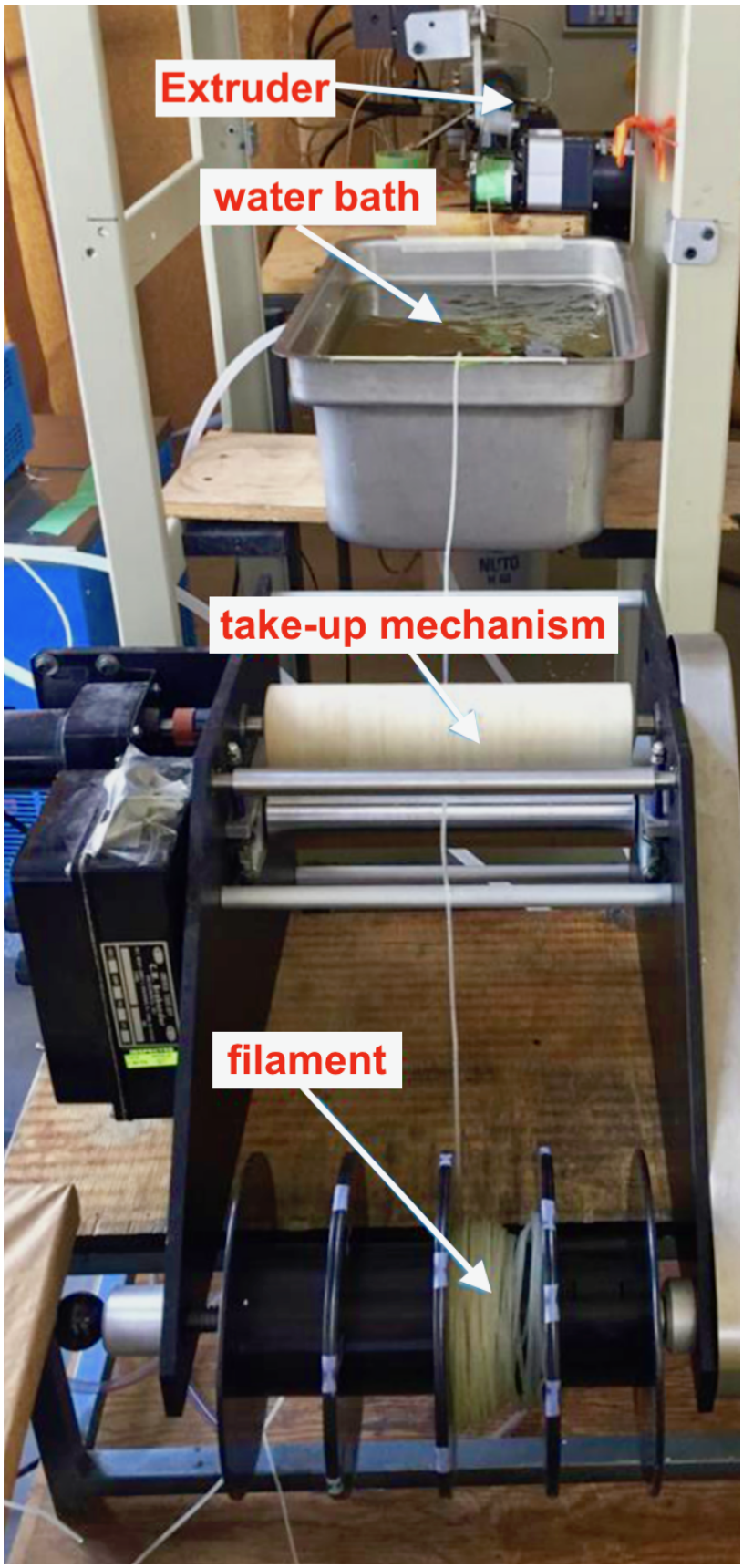

Figure 2.3: Set-up for the extrusion of SMP filament in the lab [27].

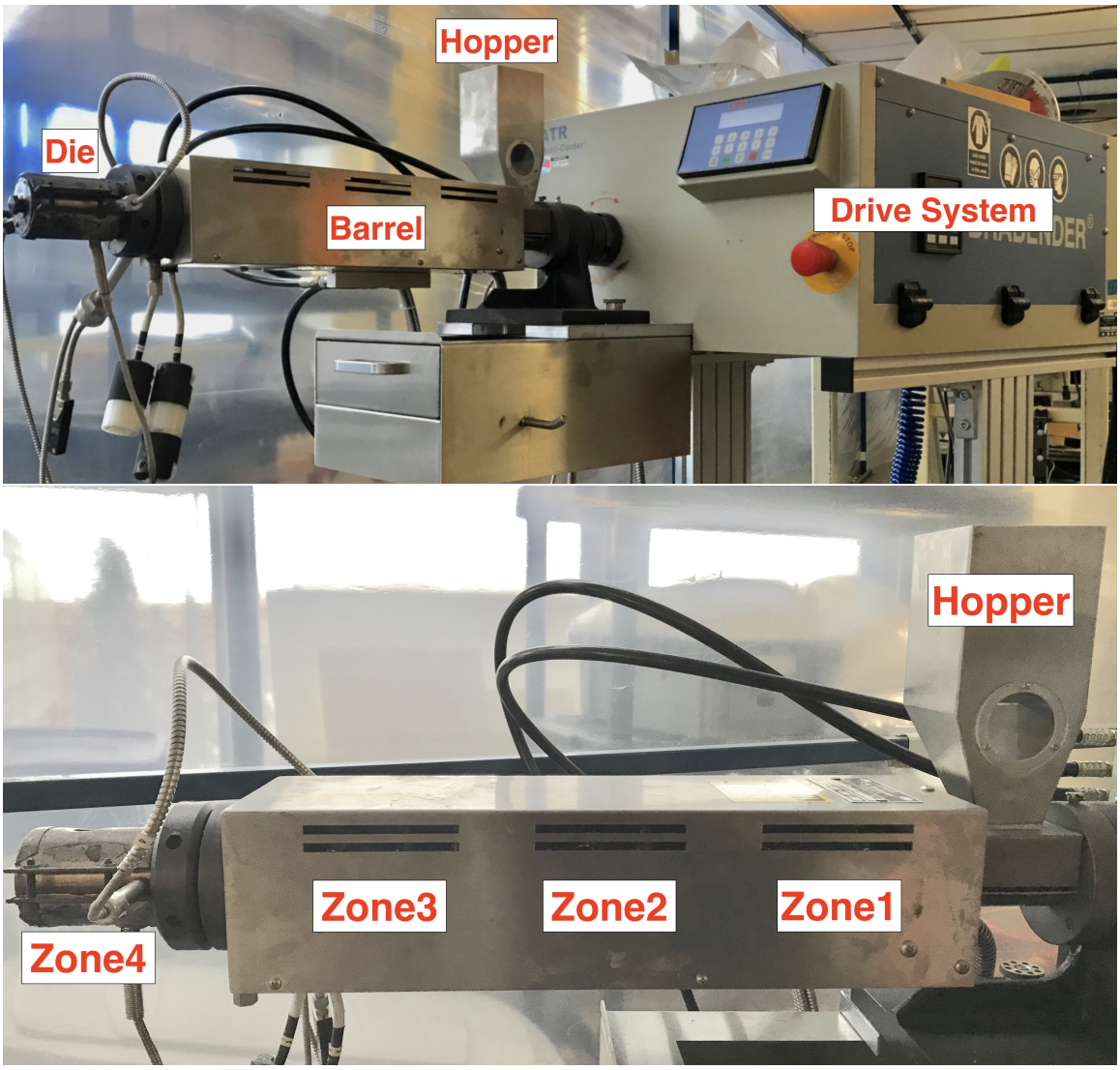

Figure 2.4: Illustration of Brabender Inc. drive system attached to the extruder (top), side view of extruder melting barrel with four heating zones (bottom).

2.3 Digital Image Correlation (DIC)

Digital image correlation (DIC) is an optical measurement method that uses image registration and tracking techniques. This method was originally developed in 1970's for the purpose of producing accurate 2D and 3D measurements of dislocations in digital images [30, 31]. Due to the considerable potential of this method, utilization of DIC technique in the field of mechanics started shortly after the development, back in the early 1980's [32–34]. In the following years after 1980's, the application of DIC method in experimental mechanics has been improved and optimized significantly [35].

Today, DIC is a state-of-the-art technique that can be used for accurate strain measurement [36]. Because of its capability for fast data acquisition, this technique is well suited for the characterization of material properties both in the elastic and plastic ranges [36]. It also offers a variety of advantages. First of all, using DIC, deformation and strain of any desired position that is speckled can be measured. Moreover, no physical contact with samples is required in DIC which means that this type of measurement does not make any impact on the samples during the experiment [37]. Additionally, it is know that DIC is capable of producing highly reliable strain measurement results [36]. In other words, DIC offers full field, non-contact, and considerably high accuracy for displacement and strain measurements.

2.3.1 Basics of DIC

Digital image correlation works based on the comparison of two images acquired at different states, one before deformation and the other after. These two images are referred as "reference image" and "deformed image". After acquisition by a camera, these images are digitized and stored in a computer hard disk for analyses. Two subsets of images, also known as Region of Interest (ROI), are chosen respectively from the reference and deformed images for correlation calculation. ROI is referred to

the portion of an image that is subjected to the image tracking in DIC process [38]. The algorithm of correlation, detecting the local displacements u and v by comparing the two subsets in reference image and deformed image, is described next.

Given an arbitrary subset, a $n \times m$ pixel area, from the reference image and a reference point (x_0, y_0) as well as a nearby point (x, y) is selected from this subset, the position (x', y') of the nearby point after the deformation is described as [39]

$$x' - x = u + \frac{\partial u}{\partial x}dx + \frac{\partial u}{\partial y}dy \tag{2.1}$$

$$y' - y = v + \frac{\partial v}{\partial x}dx + \frac{\partial v}{\partial y}dy \tag{2.2}$$

where (u, v) are the displacements of the reference point, and (dx, dy) are the position differences between the reference point and the nearby point before deformation.

Generally, the positions of the reference point and the nearby point after deformation are not exactly located at pixel points of the digital image taken after deformation, and there are no grey level values for these points. Hence, interpolation is necessary to retrieve their grey level values such that the intensity pattern of the subset could be obtained. A bi-linear interpolation is commonly used to obtain the the grey level value $I(x, y)$ at a point located between four nearby pixel points [39]:

$$I(x, y) = a_1\, x + a_2\, y + a_3\, x\, y + a_4\,,$$

where a_i's are constants obtained from the positions and the grey level values of the four nearby pixel points.

With this, the goal is to find a subset of deformed image that is correspondent to the subset of reference image by considering the displacements and its gradients. To represent the correlation of these two subsets, a cross-correlation (CC) coefficient is commonly used [36]. In this thesis, a commonly used correlation coefficient called sum of squared differences (SSD) correlation is used and is defined as [39]:

$$CC_{SSD}(x, y, u, v) = \sum_{i=\frac{-n}{2}}^{\frac{n}{2}} \sum_{j=\frac{-m}{2}}^{\frac{m}{2}} \left[I_{\text{ref}}(x + i, y + j) - I_{\text{def}}(x + u + i, y + v + j)\right]^2 \tag{2.3}$$

where $I_{\text{ref}}(\cdot,\cdot)$ and $I_{\text{def}}(\cdot,\cdot)$ denote the intensities of the points in the subsets of reference image and the deformed image, respectively. In addition, it is also customary to normalize the intensity values to offset the difference in the brightness of the images.

Now the DIC is converted into an optimization problem in which the correlation coefficient is to be minimized and the optimization variables are the two displacements and the four displacement gradients as described in Equations (2.1) and (2.2) [39].

There are several software packages available that solve the DIC optimization problem iteratively such as Avizo, Correlated Solutions, CorreliSTC, Dantec Dynamics and Digital Image Correlation Engine (DICe). In this thesis, an open source DIC tool called Digital Image Correlation engine (DICe) [40] is used to compute the strain from the post-processed images as DICe is freely available and commonly used.

For DIC to work effectively, the pixel blocks (subsets) need to be random and unique with a range of contrast and intensity levels. Hence a speckle pattern is required to be sprayed on the surface of the samples. The preparation of samples for DIC is described in details in Section 3.2.2 of Chapter 3.

2.4 Classical Laminated Plate Theory (CLPT)

Classical laminated plate theory (CLPT) also known as classical laminate theory (CLT) is the simplest Equivalent Single Layer (ESL) model which is a direct extension of the classical plate theory (CPT) [41]. CLPT is a well known and commonly used predictive tool. This theory was evolved in the 1960s [42]. CLPT employs simplifying assumptions to be able to compute elastic properties of a multi-layer anisotropic material [43]. CLPT requires some properties of a single layer as an input to the model [44]. The required parameters for each layer are: longitudinal and lateral elastic modulus (E_1, E_2), major Poisson's ratio (ν_{12}), shear modulus (G_{12}) and its thickness (t_k).

Using the five aforementioned parameters, reduced stiffness matrix $\bar{Q}$ of each layer can be calculated. CLPT use $\bar{Q}$ of each layer to develop the equivalent stiffness

matrix of a stack of layers [12]. The key assumption used in CLPT calculation of ESL stiffness matrix is called Kirchhoff - Love hypothesis which comes from CPT [44]. Kirchhoff–Love hypothesis assumes that after bending and stretching, A straight line perpendicular to the mid-plane remain i) straight and ii) perpendicular to the mid-plane. Other assumptions used in CLPT are as follows [44]:

- Each layer is assumed to be homogeneous in such a way that its effective properties can be calculated.
- Plane-stress condition is applied.
- The displacement components are continuous through the entire thickness which means that no slip occurs between the adjacent layers and the layer are perfectly bonded to each other.
- Each layer is either isotropic or orthotropic or transversely isotropic.

The CLPT model is a widely known and implemented method which has been employed for a variety of different multi-layer materials [12].

2.5 State of the Art

There have been numerous research studies on the influence of different parameters on EBAM mechanical properties. One of the main challenges in this domain is that their findings could not be compared to each other since the manufacturing conditions are different. Therefore, additional studies to completely understand the key tenets of these factors are required. Some different researches have been described as below.

Using different materials and softwares, Tanikella et al. [45] showed that the building orientations have impacts on the mechanical properties of the 3D printing end-parts. Having investigated the mechanical properties of RepRap 3D printed parts using a commercial open-source RepRap (Lulzbot TAZ) for a wide range of materials

including: Ninjaflex (5 colors), SemiFlex (4 colors), HIPS (5 colors), T-Glase (5 colors), polycarbonate (1 color), Nylon (2 Types), and ABS (1 color), their researches showed that the variance in the color of the same material does not significantly impact the tensile strength, but it is important when different materials are compared. They also found that the most flexible material was Ninjaflex, which did not break after an extension of about 800%. The tensile stress for Ninjaflex at 800% extension was over 12 MPa (average of all colors). Nylon materials were shown to be stronger than Ninjaflex and SemiFlex, and much more flexible than ABS, HIPS, T-Glase, and polycarbonate, which provides a good balance between strength and flexibility.

A similar trend was also observed by Tymark et al., [46]. Their study quantifies the basic tensile strength/stress, and elastic modulus of printed components using realistic environmental conditions for standard users of a selection of low-cost, open-source 3-D printers. Working with different layer thicknesses including of 0.2, 0.3 and 0.4 mm, they proved that decreasing layer thickness increases the strength. They results showed that the specimens printed with a 0.2 mm layer thickness had the greatest tensile strength, while specimens at 0.4mm layer height had the greatest elastic modulus. For these layer thicknesses, tensile strength averages varied by 11.9 MPa, or 22%, between 0.3 mm and 0.2 mm layer heights while elastic modulus varied by 194 MPa, or 6%, between 0.4 mm and 0.2 mm layer height. According to the other researches, some other parameters such as raster angles, raster-to-raster gap, perimeter-to-raster gap and layer thickness [47] as well as the model temperature [48] have been shown to have influence on the tensile strength. The effects of these mentioned parameters will be described elaborately as follows.

But these factors' influences on mechanical parameters are not at the same level. For example in the research conducted by Durgun and Ertan [49], the building orientation, as a case in point, showed a more significant influence on the surface roughness and mechanical properties of the resulting fused deposition part, than raster angle. The results suggested that the surface roughness has a very close relationship with

the mechanical properties.

The interactions of these key factors play a very critical role on the mechanical properties [50, 51]. For instance, raster angel, as one of the most important process parameters impacting mechanical behavior, affects the anisotropy of the EBAM parts' strength [47, 52, 53].

In the research done by Ahn et al. [48], the different parameters such as the raster orientation and the air gap were examined and the tensile strengths and compressive strengths of directionally fabricated specimens were measured. According to their investigation, the FDM parts that were made with a 0.003 inch overlap between the roads, had the typical tensile strength ranged between 65 and 72 percent of the strength of injection molded ABS P400. They showed that the air gaps and infills are the factors that determine the dimension of the contact zone between extruded beads, and as the consequence they affect the bond strength and the mechanical properties [48, 54].

Among the important process parameters, temperature also has a significant impact. However its interaction with the other process parameters has not been investigated enough so far [48, 55–57].

Considering the process cost, with the overall goal of customizing the infill design parameters for providing the largest cost-efficiency along with favorable mechanical properties, Baich et al. [58] studied the relationship between layer in fill and compression strength, flexural strength and tensile strength. Using different levels of density, they found that printing solid infill is beneficial in the case of bending and compression samples comparing to non-solid infill patterns.

In line with [58], Onwubolu et al. [59] found that the layer thickness and raster width should be minimal in order to improve the tensile strength of ABS specimens. A similar conclusion was also reached by Durgun and Ertan [49]. Likewise, in other researches, a better tensile strength of PLA speciments for small values of layer thickness has been observed [60–62]. The same conclusion was also presented for ABS (poly

acrylonitrile butadiene styrene) [50] and PEEK (polyether ether ketone) [57].

Regrading the other important factors, Hernandez et al. [63] noted the influence of the raster angle on specimens' flexural properties. Their results showed a significant increase in compressive and flexure strengths of the material at 0 degrees in the XY plane. Their findings also showed that printing 90 degrees resulted in the highest tensile strength compared to the other orientations.

Ziemian et al. [2, 64] showed the highest tensile strength could be obtained when the raster is aligned along the longest dimension. Fatimatuzahraa et al. [65] observed that in terms of the strength, 0°/90° orientation is similar to 45°/-45° orientation. The same results for 0° raster were also demonstrated by Tymrak et al. [46].

Several researches have been done on the highest strength of EBAM parts [49, 50, 63, 65, 66]. Ziemian et al. [2, 64] also studied the flexural strength, and their results showed the highest ultimate strength value at the 0° fiber orientation, followed by 45°/-45°, and 90° orientation. They showed that raster orientation has a significant influence on the fatigue performance of FDM ABS components. Aligning FDM fibers along the axis of the applied stress provides ameliorated fatigue life.

Fatimatuzahraa et al. [65] showed that 45°/-45° raster orientation provides better flexural strength than 0°/90° orientations. In the research that was done by Durgun et al. [49], the surface roughness, tensile strength and flexural strength were tested for five different raster angles (0°, 30°, 45°, 60° and 90°) and three different orientations (horizontal, vertical and perpendicular). Their results showed that the specimen build with 0° raster angle and in horizontal direction presented optimal mechanical properties, with the optimum production time and cost. They also showed that the the flexural strength was higher than tensile strength for all their experimental runs.

There are also a lot of researches on the impact strength [2, 50, 65–68]. Alvarez et al. [68], analyzed the influence of the infill percentage on the mechanical properties. Their findings indicated that the maximum tensile force (1438N), tensile stress (34,57MPa) and the maximum impact resistance were obtained in 100% infill. More-

over the higher effective printing time and the smaller tensile strength and impact resistance were also observed with a 100% infill.

Additionally, Fatimatuzahraa et al. [65] noted that the value of impact strength is higher when the orientation is criss-cross at (45°/-45°). Having tested the specimens under several experiments such as tensile test, beam deflection test, bending test and impact test to find out the best result, they showed crisscross sample had higher strength value for most of the tests (deflection, flexural and impact test) making it stronger than cross orientation. For tensile test result, cross able to exert higher strength as the result of its cross-section structure. In fact, the structure of criss-cross orientation (45°/-45°) resulted in higher surface roughness at the edge of sample causing it to fracture easily. They mentioned that stress concentration takes place at the edge of the sample. Therefore, that is the main reason that the cross sample has higher tensile strength comparing to crisscross sample.

The numbers of the contours' (perimeters) are also the other factors that affect the mechanical properties [69–71] by influencing the specimen stiffness and strength.

Another process parameter that highly influences the mechanical properties, is the building orientation. Different studies have presented this relationship for various materials and building directions [2, 50, 53, 72–76]. Motaparti et al. [74], as one of these studies, noted that 0° and 90° raster angles have higher yield strength comparing to those with (45°/-45°). Additionally, building orientation influence is considered in combination with raster angle and raster pattern in [49, 50, 59, 73]. Raster orientation and its pattern are the other parameters that have effects on the mechanical properties [2, 46, 64, 65, 77, 78]. In the study conducted by Letcher et al. [78], the best tensile strength was observed at the 0° raster orientation. Their flexural test results showed that the vertical build direction exhibits 15-30% higher yield strength compared to the horizontal direction for specimens which were built with solid and sparse build coupons. Moreover, the compression test results indicated that the horizontal build direction presented 15- 40% higher compressive strength compared to vertical build

direction. Their findings also indicated the 5-10% increase of flexural strength for both horizontal and vertical build coupons, (0, 90) raster angle in comparison to the (45, -45) raster angle. The similar result was also presented by Tymrak et al. [46].

In the context of polymer filament bonding, temperature also plays an important role. Ahn et al. [48] showed that the temperature has no effect on mechanical properties. A similar conclusion was also reached by Rodriguez et al. [55].

Contrary to these findings Sun et al. [56] presented the influence of envelope temperature and convective conditions from the building space, on the filament bonding, and therefore, the end-part strength. They showed that the temperature has a great effect on the molding precision of PEEK material. Their result showed that the forming precision of the material can be promoted as the temperature increases. This result ties well with the study which was done by Xiaoyong et al. [57]. They reported that the highest tensile strength was obtained when the platform temperature was high (130 C°) at 25 C° ambient temperature.

2.6 Gap in Research

According to a recent survey on the effect of EBAM production parameters on mechanical properties of the end-product [2], among 49 studies mentioned in this survey, none of them were on SMPs. This is an evidence that effect of fabrication parameters on mechanical properties on SMPs has rarely been studied. Notable exceptions are [11, 27, 79, 80]. Among these four studies only Villacres et al [11] investigates the influence of EBAM parameters on mechanical properties of the SMP product. However, Villacres et al [11] used shell thickness of 0.4 mm as a fixed production parameter. This means that almost one third of the sample cross section in the gauge length was covered with shell area. This can cause a significant impact on the final results, since shell properties are different from the cor infill percentage and region raster angle. Additionally, there is no investigations on infill percentages above 100% [11] while this is a common practice in this field [2, 48, 55–57, 59, 79]. These shortcomings are

addressed in Chapter 3 by providing a comprehensive experimental investigation of effect of two production parameters (infill percentage and raster angle) on four mechanical properties (elastic modulus, yield strength, maximum elongation, modulus of resilience and tensile toughness) of end-part.

Moreover, the majority of studies in this field including four aforementioned works, attempted to tackle this issue by experimental investigation (see the review paper [2] and the references therein). Although empirical approach can provide a comprehensive solution to this matter, it is often associated with several disadvantages. First of all the process is time consuming and it requires a significant amount of effort to be devoted to that. Besides, experimental setups are often expensive and obtaining meaningful experimental results is generally costly. Furthermore, with obtained experimental results, it is quite difficult to extrapolate the results to a different EBAM setting [12]. Thus, a handful of studies in literature develop an analytical model to predict the final mechanical behaviour of the specimens according to some of the production parameters [12, 81]. In this context, to the best of my knowledge, only one study used classical laminated plate theory (CLPT) to describe the mechanical behaviour of EBAM produced parts [12]. However, the model presented in [12] requires the value of shear modulus (G_{12}) and the Poisson's ratio (ν_{12}) as input to their model. These two values are often difficult to obtain experimentally [12].

Additionally, this study only worked on PLA and ABS as EBAM material. Another major drawback of [12] is that their experimental samples were produced in dogbone shape with two contour lines for the shell, similar to [11]. These drawbacks are addressed in this thesis.

2.7 Conclusions

In this chapter, background information on extrusion-based additive manufacturing (EBAM) and performance of shape memory polymers were presented. Given that the shape memory polymer was acquired in the form of pellets, a filament extrusion

process is required. The different stages involved in the filament extrusion process and the settings used at every stage were described in details. A brief overview of DIC and CLPT theory were also presented. At the end of, recent related works in EBAM of SMPs were reviewed and the gap in the research were highlighted.

Chapter 3

Effect of raster angle and infill percentage on mechanical behavior of SMP based EBAM - An experimental investigation

3.1 Introduction

Shape memory polymers (SMP) are getting growing attention in the recent years [9, 82, 83]. Among different techniques used to produce SMP parts, EBAM has been in the spotlight [84]. SMP based EBAM also known as 4D printing offers a variety of promising applications as described in Chapter 2. Creating a viable SMP product with EBAM method needs a general understanding of mechanical behaviour of manufactured parts.

Mechanical properties of EBAM produced parts are highly dependent on the EBAM process parameters [2]. Hence, several studies investigated the relationship between EBAM fabrication parameters and resulted mechanical properties of the produced part [50, 85–89]. However, most of these studies focused on commercial EBAM polymers such as ABS (polyacrylonitrile butadiene styrene) and PLA (polylactic acid). In fact, according to a recent survey on the effect of production parameters of EBAM on mechanical properties of the product [2], among 49 studies mentioned in the survey, none of them was on SMPs. This is an evidence that me-

chanical properties of SMPs based on EBAM fabrication parameters has rarely been studied directly. A few notable exceptions are [11, 27, 79, 80]. Raasch et al. [79] investigated the impact of annealing heat treatments and testing temperatures on the mechanical properties of polyurethane SMPs. Also, Ma conducted creep and bending experiments on polyurethane SMP samples produced by EBAM in order to extend a previously developed model by Tobushi for bending [27]. Additionally, Yang et al. [80] studied the effect of EBAM parameters on dimensional accuracy and surface roughness of SMPs , but no mechanical property was investigated. Finally, Villacres et al [11] examined the effect of raster angle and infill percentage on elastic properties of SMP produced by EBAM. But in this study, shell thickness of 0.4 mm was used as a fixed production parameter. This means that almost one third of the sample cross section in the gauge length is shell area. This can cause a significant error in the final results, since shell properties are different from the core region infill percentage and raster angle. The aim of this chapter, is to obtain a better understanding of effect of infill percentages and raster angle on mechanical behavior of SMP based EBAM parts. Additionally, this work presents the results for a wider range of infill percentage compared to that in [11].

This chapter is organized as follows. Detailed procedures for preparation of the tensile test samples are presented step by step in Section 3.2. This will help future studies to reproduce similar samples. Section 3.3 describes the procedure for calibration of strain measurements using DIC analysis. In Section 3.4, variation of sample density with infill percentage is described. Tensile test results are reported in Section 3.5. At the end, effect of raster angle and infill percentage on four mechanical properties are analyzed and recommendations are provided for manufacturing of EBAM parts.

3.2 Methods and Procedures

3.2.1 Sample Preparation

As described in Section 2.2 extruded filaments used in EBAM process were cooled by soaking them in water bath. Thus 14 hours of drying process is required for filaments. The dried filament diameter is measured before each EBAM production session (14 times in total). The average filament diameter is 2.85 mm with the standard deviation of 0.1 mm. Once filaments are dried they are still able to absorb moisture from environment's humidity. To prevent this, the filaments were kept in a dedicated insulated chamber equipped with silica gel desiccant bead packages as shown in Figure 3.1(a). The chamber was designed in such a way that it enables filaments to be fed directly into a EBAM machine (see Figure 3.1(b)).

(a) (b)

Figure 3.1: Insulated chamber designed for dried filaments (a), Direct feed from chamber into EBAM machine (b).

Throughout this thesis, an Ultimaker 3 equipped with a 0.4 mm print core and a glass bed is used for sample production. Ultimaker is an example of a low cost system used for manufacturing EBAM test parts which has been used in several studies in the past [2, 53]. General specifications of Ultimaker 3 are listed in Table 3.1 [90].

Table 3.1: General specifications of Ultimaker 3.

Printer and printing properties	
Technology	Fused filament fabrication (FFF)
Build volume	XYZ: 215 x 215 x 200 mm
Filament diameter	2.85 mm
Layer resolution	0.4 mm nozzle: 200 - 20 micron
XYZ resolution	12.5, 12.5, 2.5 micron
Print head travel speed	30 - 300 mm/s
Build plate temperature	20 - 100 °C
Nozzle temperature	180 - 280 °C

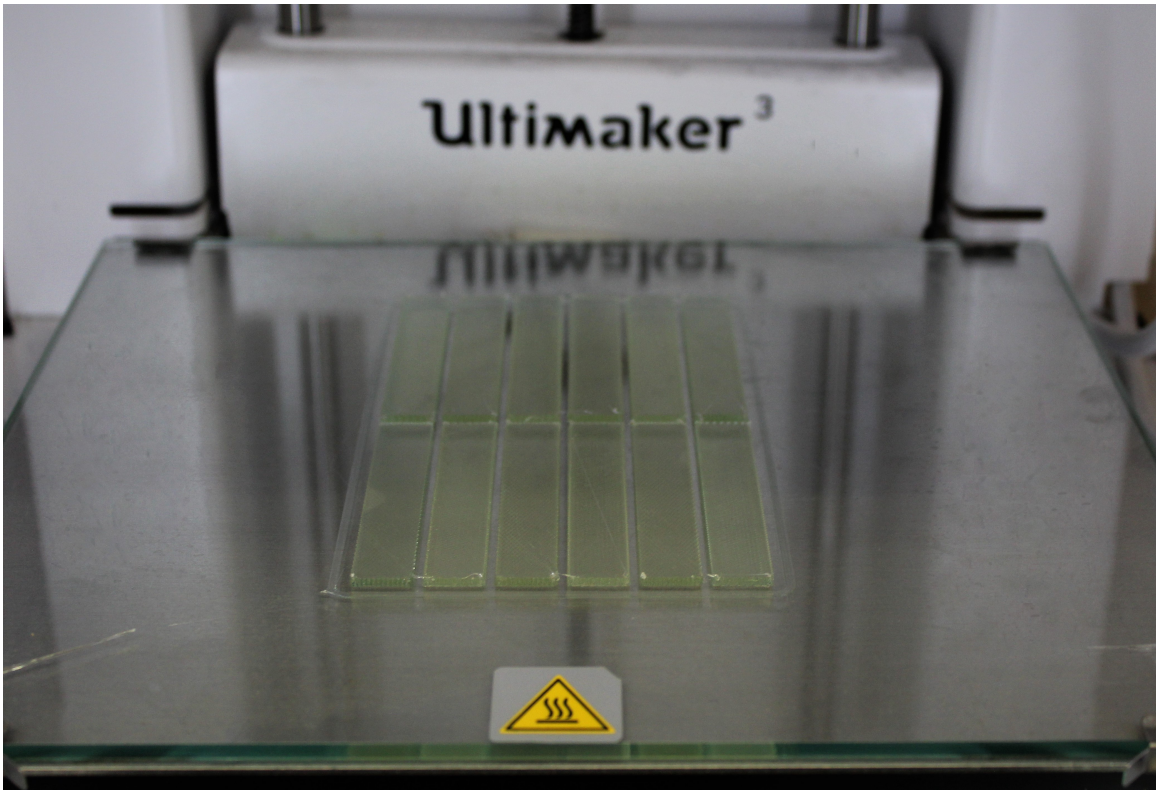

Figure 3.2: A batch of 12 printed samples (115% infill and 45° raster angle)

In each production session, 12 rectangular samples with a specific infill percentage and raster angle have been produced as shown in Figure 3.2. Also infill percentage and raster angle is changed for each EBAM session to investigate the influence of mentioned parameters on the mechanical properties of end-part. The specimens are produced at 3 different infill percentage levels: 85%, 100% and 115%. The primary motivation for including 115% infill samples is based on the density measurements

of 100% infill samples in this study which suggests that the product still contains small air gaps at 100% infill level (see Section 3.4 for more details). Hence, 115% infill percentage is investigated as the infill level that results in a product with the maximum possible density of the infill material. At 115% infill level, 0° and 90° raster angles are investigated. At 85% and 100% infill level, 30° and 60° raster angles are investigated in addition to 0° and 90° due to the increased sensitivity of mechanical properties to the raster angle at these infill percentages. For 30° and 60° raster angels, $[\theta/\text{-}\theta]_{4s}$ stack sequence is used to assure the symmetric build of EBAM samples. In other words, 30° and 60° samples are produced by stacking of layers with the raster angle of θ and $-\theta$ on top of each other. Figure 3.3 shows a schematic illustration of 0°, 30°, 60° and 90° raster angles.

Printed samples dimensions are measured as 12mm × 66mm × 1.6mm with the standard deviation of 0.3mm, 0.3mm and 0.1mm, respectively. Table 3.2 shows the average density and weight of all of the samples used in this work. Note that the density of samples varies with the infill percentages (see Section 3.4 for more details).

Table 3.2: Average weight and density of the printed samples.

Infill Percentage	raster angle	Average weight(gr)	Average Density(gr/cm^3)
85%	0°	1.395	1.101
	30°	1.397	1.103
	60°	1.397	1.103
	90°	1.393	1.101
100%	0°	1.530	1.208
	30°	1.532	1.209
	60°	1.533	1.210
	90°	1.530	1.208
115%	0°	1.596	1.260
	30°	1.599	1.262
	60°	1.597	1.261
	90°	1.597	1.261

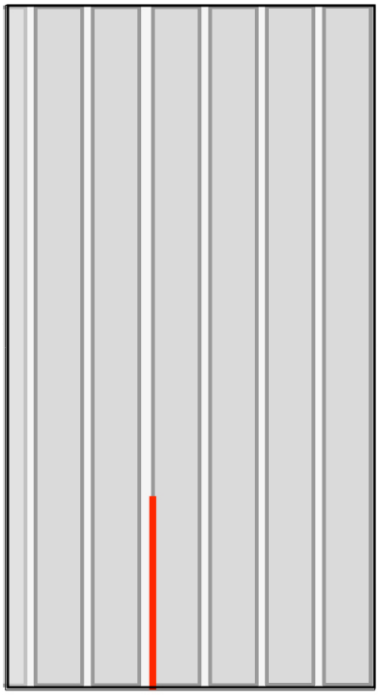

(a) 0° raster angle.

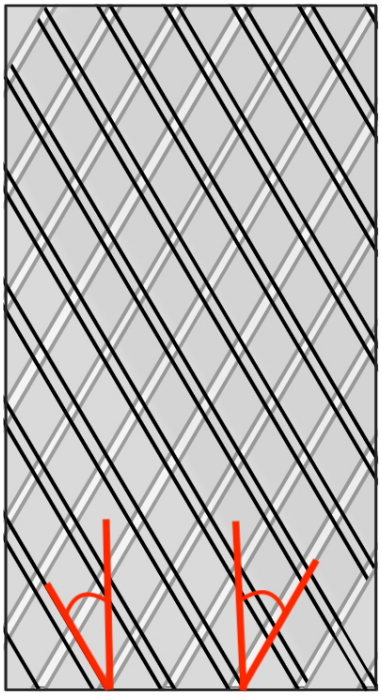

(b) 30° raster angle.

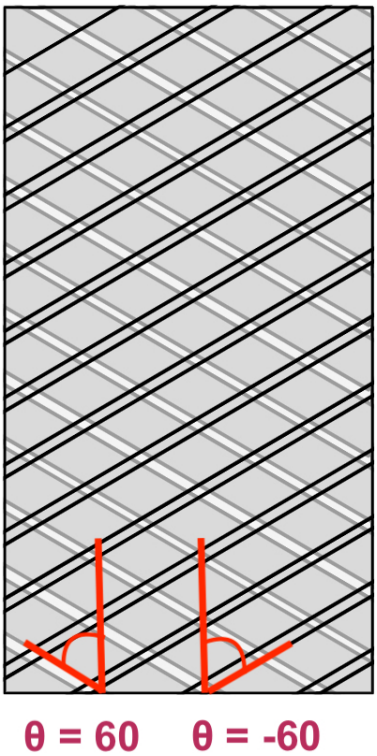

(c) 60° raster angle.

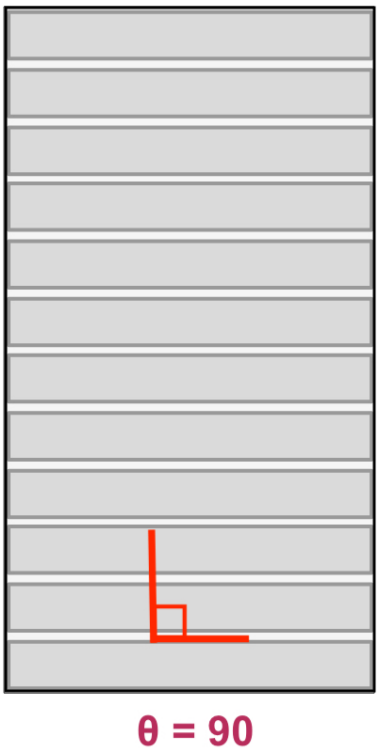

(d) 90° raster angle.

Figure 3.3: Schematic illustrations of different raster angles.

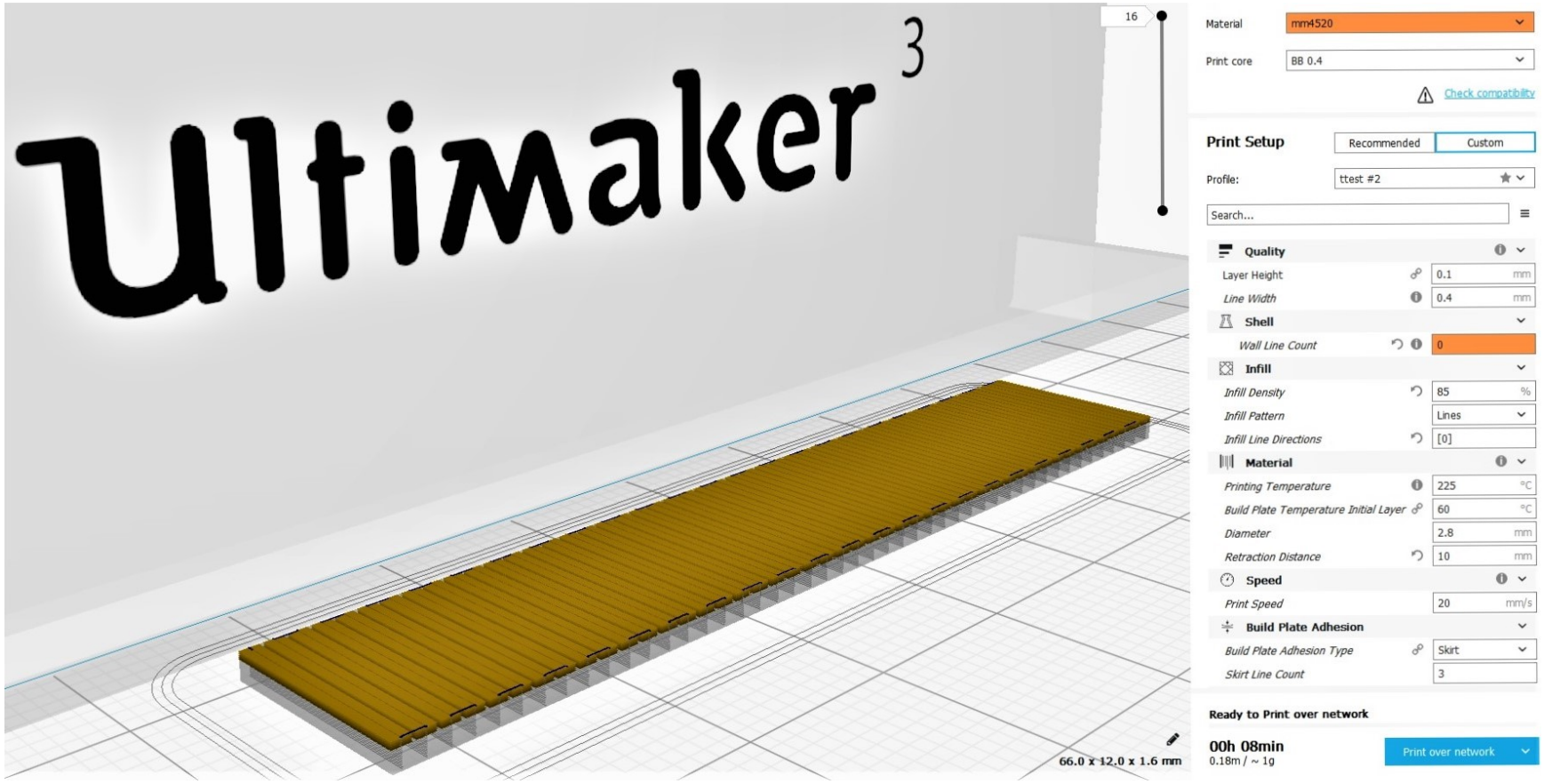

Figure 3.4: Screenshot of Cura that shows the sliced rectangular sample and the specified fabrication parameters.

The model of rectangular samples is created using a CAD software and it is then sliced using an open source 3D printer slicing application called Cura (see Figure 3.4). Essential fabrication parameters, such as the layer height, line width, printing temperature and printing speed are kept constant for every specimen in order to assure the consistency of the results. These values are listed in Table 3.3.

Table 3.3: Fixed fabrication parameters

Parameter	Value
Layer Height	0.1mm
Line Width	0.4mm
Wall Line Count	0
Infill Pattern	Line
Printing Temperature	225°C
Build Plate Temperature	60°C
Filament Diameter	2.8mm
Retraction Distance	10mm
Print Speed	20mm/s

Figure 3.5: Illustration of the CNC machining process.

The samples are then send for machining. The main reason is that in EBAM process, the outer walls of the produced sample have different mechanical properties from the infill. This is mainly due to the large stress concentrations caused by the termination of deposition paths [48]. Moreover, this termination of paths leads to an excessively rough surface at the edges of test sample [91]. A common solution is to use a shell layer to relieve the stress concentrations and improve the surface roughness.

However, this layer is not effected by raster angle or infill percentage, which are the main investigation parameters in this study. Hence, in this thesis, CNC machining is used to machine rectangular specimens into dogbone samples. The main advantage of using machining instead of directly printing dogbones is that it removes the shell layer from the sample edges, leaving the oriented fabricated lines behind. A specific fixture is designed and made for holding specimens in place during the machining process as shown in Figure 3.5. Main machining parameters are listed in Table 3.4.

Table 3.4: Fixed machining parameters

Parameter	Value
Tool Diameter	0.25”
Spindle Speed	3000 RPM
Horizontal Feed Rate	10 in/min
Step Depth	0.02”

Dogbone model dimensions are based on the ASTM D638-14 standard type V [92]. Note that for CNC machining of the dogbone, the G-Code is generated from the solid model created by SolidWorks. As the final step before machining, each sample is marked using a specific stencil and then drilled in order to be prepared to be mounted with screw to the fixture (see Figure 3.6).

(a) After drilling/Before drilling/Stencil

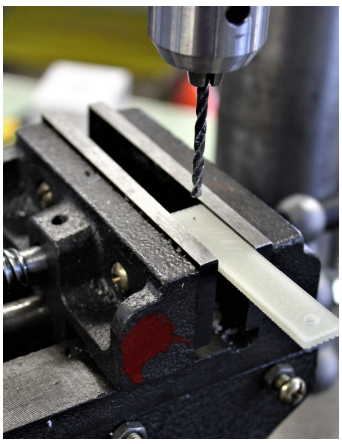

(b) Drilling the marked point

Figure 3.6: Drilling process of a sample.

3.2.2 Preparation for Digital Image Correlation (DIC)

Once the samples are ready, a speckle pattern is painted on each machined sample using a Krylon EZ Touch paint spray[1]. As described in Section 2.3.1, creating a speckle pattern on the sample is the primary step for DIC. In this thesis, DIC is used to provide a reasonable accuracy in strain measurements. Also one sample left unpainted together with another fully painted sample (white) to assure that the paint does not have any impact on the mechanical properties of the polymer. From Figure 3.7 it can be observed that there is no significant difference in mechanical properties of fully painted and unpainted samples from the speckled ones.

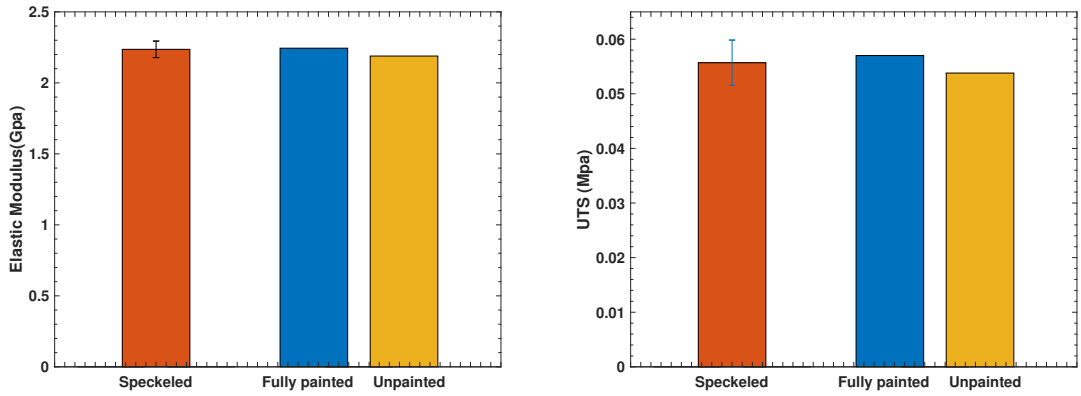

(a) Elastic modulus

(b) Ultimate tensile strength

Figure 3.7: Mechanical properties of speckled samples vs painted and unpainted samples.

It is known that surface pattern can potentially effect DIC results [36]. Thus, the speckled pattern is painted in red to be distinguishable from the surface pattern of samples made by EBAM process (see Figure 3.8). Note that surface pattern will later appear as a black and white pattern in the pictures.

In this work, a Canon EOS Rebel T6i camera equipped with a Canon EF 75-300mm lens was used to capture DIC images with the rate of 4 frames per second. A Matlab code was developed to split each image into its 3 main color channels: blue, green

[1]Krylon EZ Touch paint is specifically designed for painting on plastics

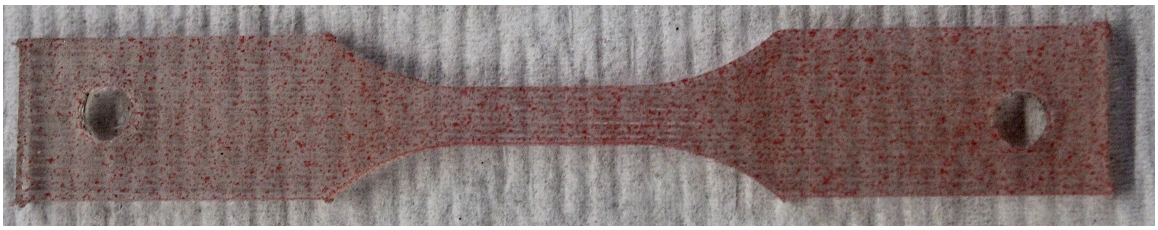

Figure 3.8: An example of speckled sample.

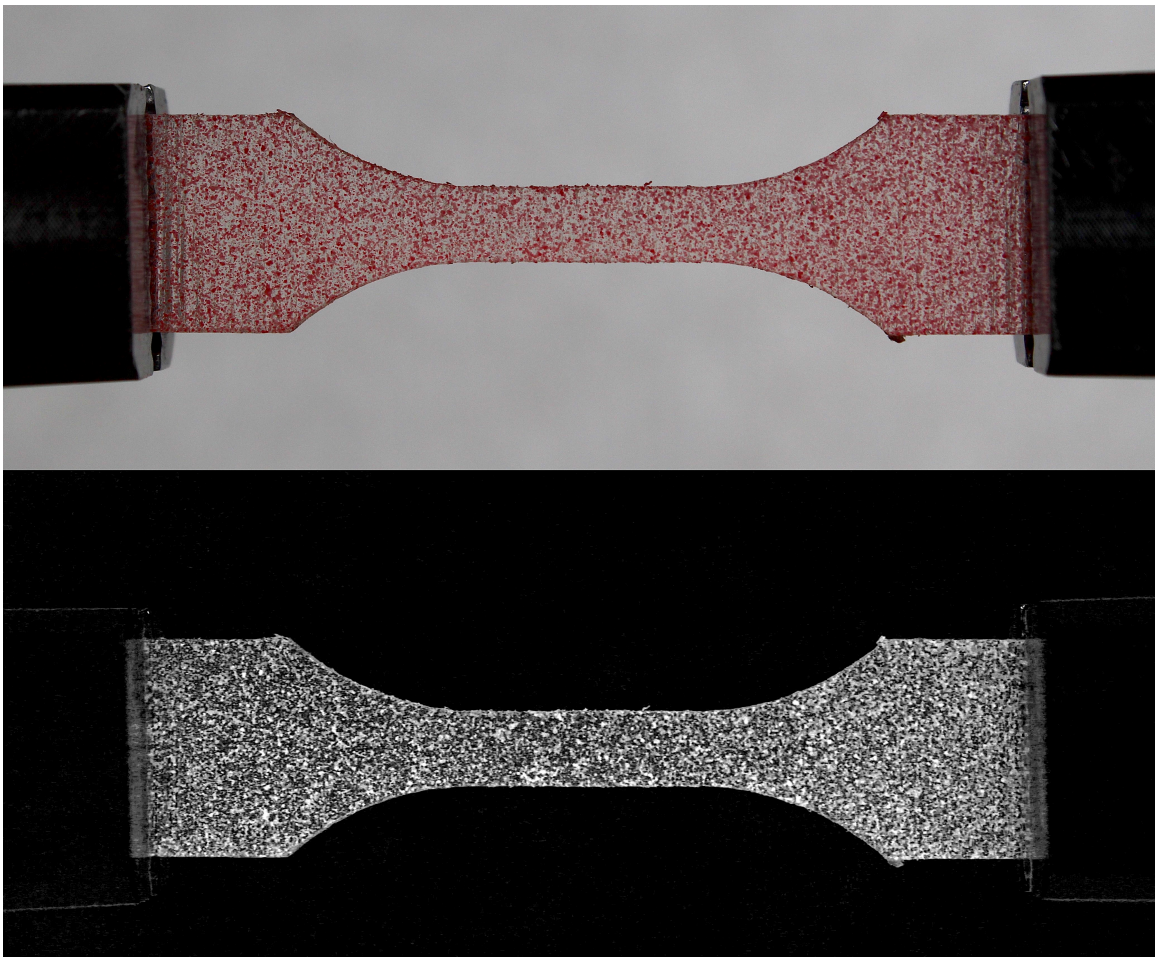

Figure 3.9: An example of captured image for DIC BEFORE pre-processing (top), An example of captured image for DIC AFTER pre-processing (bottom).

and red. In addition, the average of the green and blue channels were deducted from the red channel. This will result in a black and white image which only highlights the red speckled pattern, as shown in Figure 3.9. This means that the surface pattern of the sample, together with the background noise is removed for DIC analysis. An open source DIC tool called Digital Image Correlation engine (DICe) [40] was used

to compute the strain from the post-processed images. In order to produce more accurate results the average strain of 15 different points at the middle of gauge length was calculated for each sample as shown in Figure 3.10.

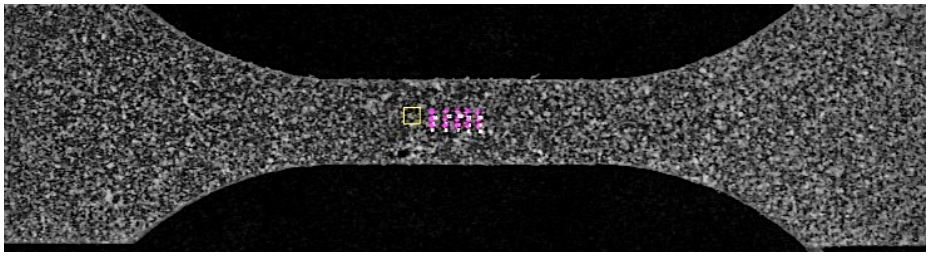

(a) DIC sample with selected points.

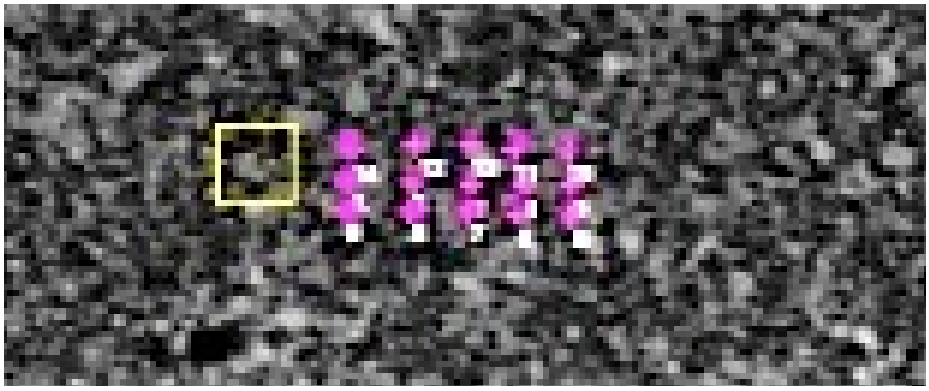

(b) zoom-in view of the points.

Figure 3.10: Illustration of 15 selected points and the subsection size shown on the sample.

3.2.3 Tensile Test Setup

In this study, all the tensile test were performed with a ElectroForce 3200 system manufactured by BOSE equipped with a 450 N load cell. A cross-head speed of 5 mm per minute was used for all samples according to the ASTM D638-14 [92]. Moreover, a torque wrench is used to assure that the upper and lower clamps are tightened to a constant torque of 1300 $N.mm$ for all the samples. A total number of 120 samples was produced and tested in 10 different categories having different infill percentage and raster angle. The results are presented in the following sections.

3.3 Calibration of Strain Measurements with Digital Image Correlation (DIC)

Deformation measurement is one of the most vital stages of tensile test. Along with the well-established strain gauge technique, several non-contact and non-interferometric optical methods such as digital image correlation (DIC) have been developed for this purpose [36]. DIC technique is widely accepted and frequently applied as a deformation measurement tool in different mechanical testing setups [36]. In this method, digital images of the deformed sample are compared with the reference image of undeformed sample to provide full-field strains [36].

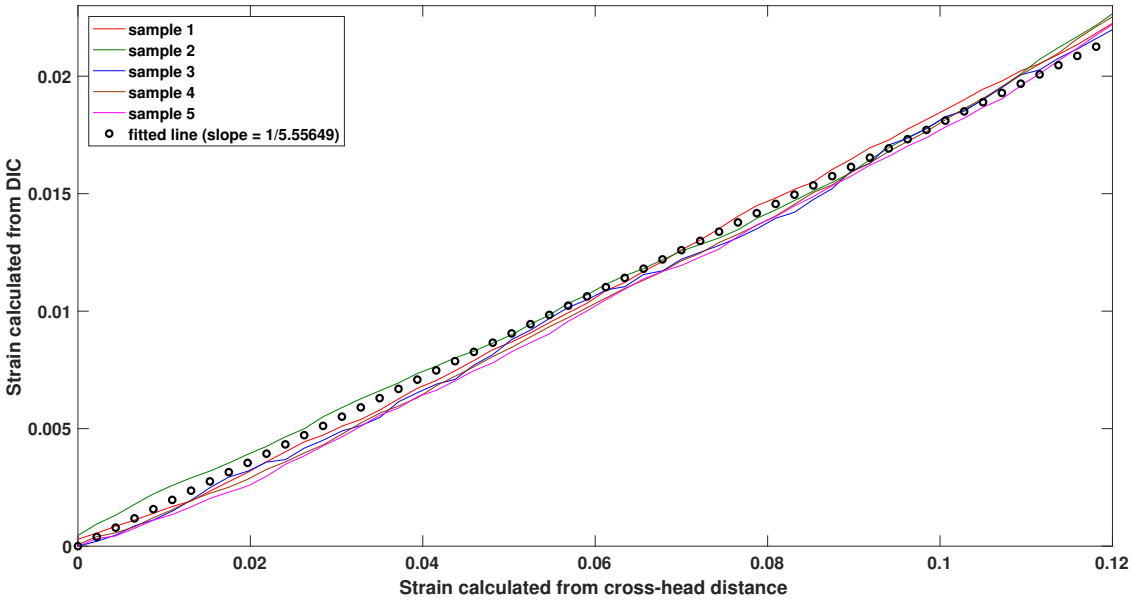

Figure 3.11: Strain calculated in elastic region from DIC analysis (vertical axis) vs. strain calculated from cross-head distance obtained from tensile test machine on 5 different samples with 115% infill and 0 degree raster angle.

In this study, DIC technique was used for strain measurements. As shown in Figures 3.11 and 3.12, in the elastic region, DIC results gives distinctly different values from machine strain values. Here, machine strain value is referred to the strain value calculated from the data obtained from tensile test machine. The difference between

DIC and machine strain is due to the fact that in the elastic region, deformation is not limited in the gauge length. Instead, a non-homogeneous deformation is happening in the entire sample, even outside of the gauge length, as shows in linear section of Figure 3.13. Although DIC strain results are not equal with the machine strain results, the ratio of machine strain to DIC strain remains constant within entire elastic region as shown in Figure 3.11. Same ratio is observed among all other samples with different infill percentage and raster angle in the elastic range as shown in Figure 3.12.

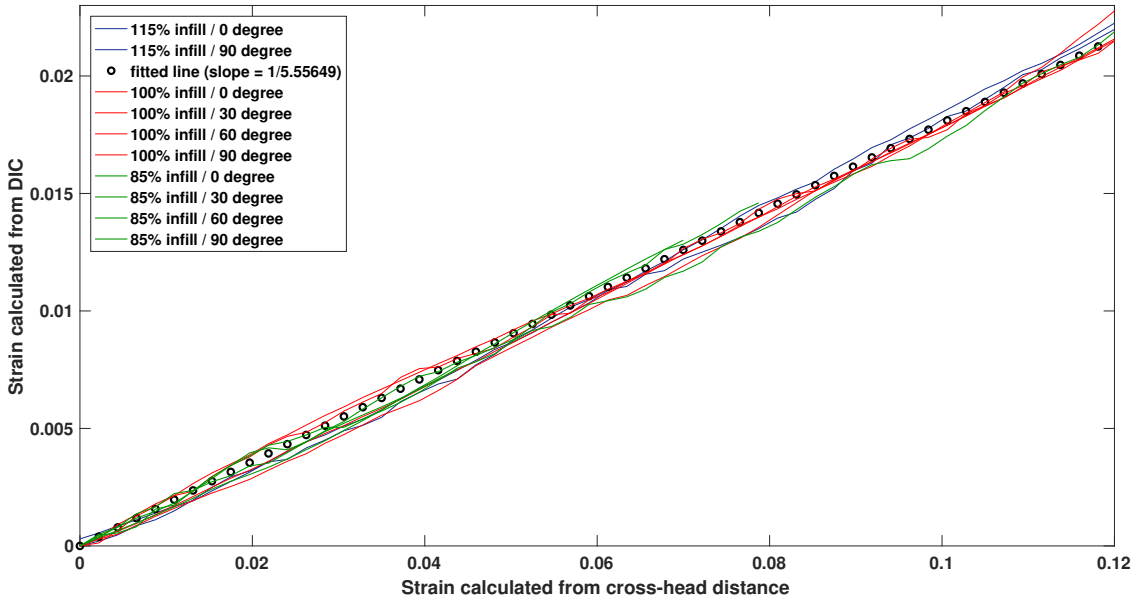

Figure 3.12: Strain calculated in elastic region from DIC analysis (vertical axis) vs. strain calculated from cross-head distance obtained from tensile test machine on 10 different samples with different infill percentages and raster angle.

Hence, it is concluded that the machine strain measurement and DIC measurements are linearly proportional in the elastic range. A linear curve in the least-square sense with $R = 99.47\%$ is fitted to the data in Figures 3.11 and 3.12. The slope of the fitted linear curve is calculated to be 5.556 (the ratio of machine to DIC strain) for the specific sample geometry used in this study.

Although this ratio is applicable for the entire elastic region, from DIC measurements in Figure 3.13, it can be observed that deformation starts to plateau outside

the gauge length. Hence DIC and machine strain values match after yield point. This means that deformations obtained from tensile test machine is reasonably accurate after yield point and thus the aforementioned ratio is equal to 1. The reason is that standard dog-bone specimens are designed in such a way that plastic deformation occurs precisely in the gauge length.

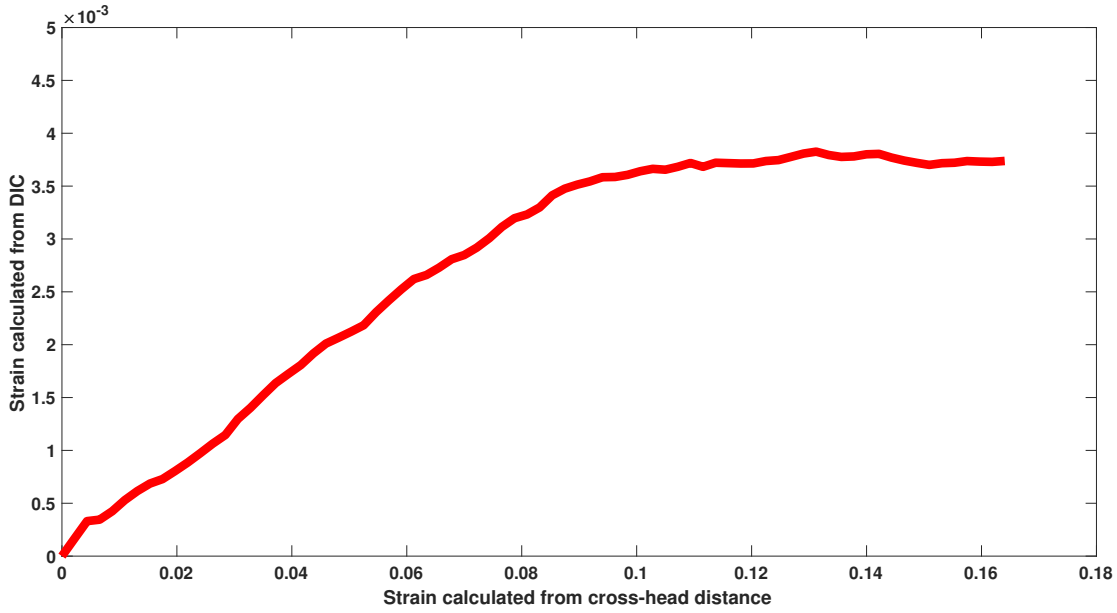

Figure 3.13: DIC strain vs machine strain on grip section of dogbone samples with 85% infill and 60 degree raster angle. DIC strain reaches a plateau after yield point.

In summary, in this thesis strain measurements are derived from machine results. However, in the elastic region deformation is divided by a fixed ratio of 5.556 to calibrate the machine strain measurements based on the DIC results.

3.4 Sample Density vs Infill Percentage in EBAM

In EBAM fabrication the infill percentage parameter can be set for the printer. However, the real density of the produced sample does not linearly increase with the infill percentage [46]. In fact, sample density depends on many other parameters including type of printer, slicing software and type of material used in sample production [46].

A set of experiments were conducted to investigate the correlation between the machine infill percentage and the density of the sample. To this end, rectangular samples ($40\times40\times1.6$ mm^3) were produced under the same fabrication conditions as the ones used for the tensile test with nine different infill percentages.

Table 3.5: Density of samples for different infill percentage

Machine infill percentage	Density (gr/cm^3)
80%	0.90703
85%	0.98398
90%	1.09062
95%	1.16797
100%	1.20547
105%	1.25234
110%	1.29023
115%	1.30937
120%	1.31305

The machine infill range is chosen from 80% to 120% with a 5% step-size in order to cover all the samples used in this study. The density of samples for each infill percentage is measured and the results are presented in Table 3.5. These values are plotted in Figure 3.14 for more illustration.

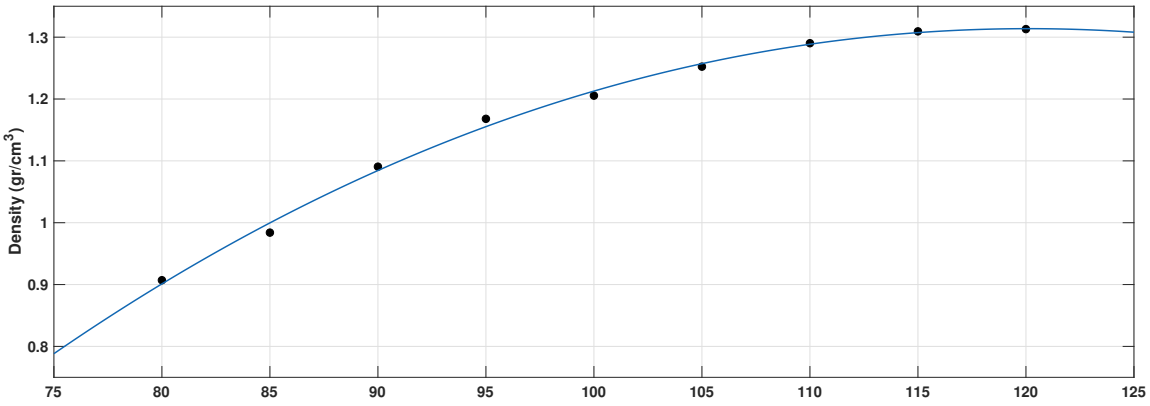

Figure 3.14: Sample density vs machine infill percentage and the third order polynomial curve fitted to the data.

The density of the dried filament is also measured as 1.31 gr/cm^3. As it can be seen from Figure 3.14, sample density reaches a plateau at 115% machine infill

as it gets extremely close to the filament density (1.31 gr/cm^3). Hence, it can be concluded that the void content is almost zero for 115% infill percentage and above. This means that the EBAM produced part with 115% infill percentage is similar to a part produced with injection molding.

3.5 Tensile Test - Results and Discussion

This section presents the experimental results obtained from a total number of 120 tensile test specimens, produced with different infill percentage and raster angle. Different mechanical properties of SMP including elastic modulus (E), yield strength (σ_y), maximum elongation percentage ($EL\%$), modulus of resilience (U_r) and tensile toughness (U_T) are investigated. This is an important step in understanding the relationship between the fabrication parameters, infill percentage and raster angle, and mechanical behaviour of the produced part. To this end, samples are produced in the same conditions but with different infill percentage in three different levels of 85%, 100% and 115% infill. In addition, four different levels of raster angle were chosen for 85% and 100% infill samples namely 0°, 30°/-30°, 60°/-60°and 90°.

Only 0° and 90° raster angles were investigated for 115% infill samples due to the close similarity in mechanical behaviour of 115% infill samples between different raster angles. Except for the two aforementioned parameters, all other production conditions were fixed during this study to preserve the consistency of the results. A representative stress-strain curve of each raster angle and infill % is shown in Figures 3.15 to 3.17.

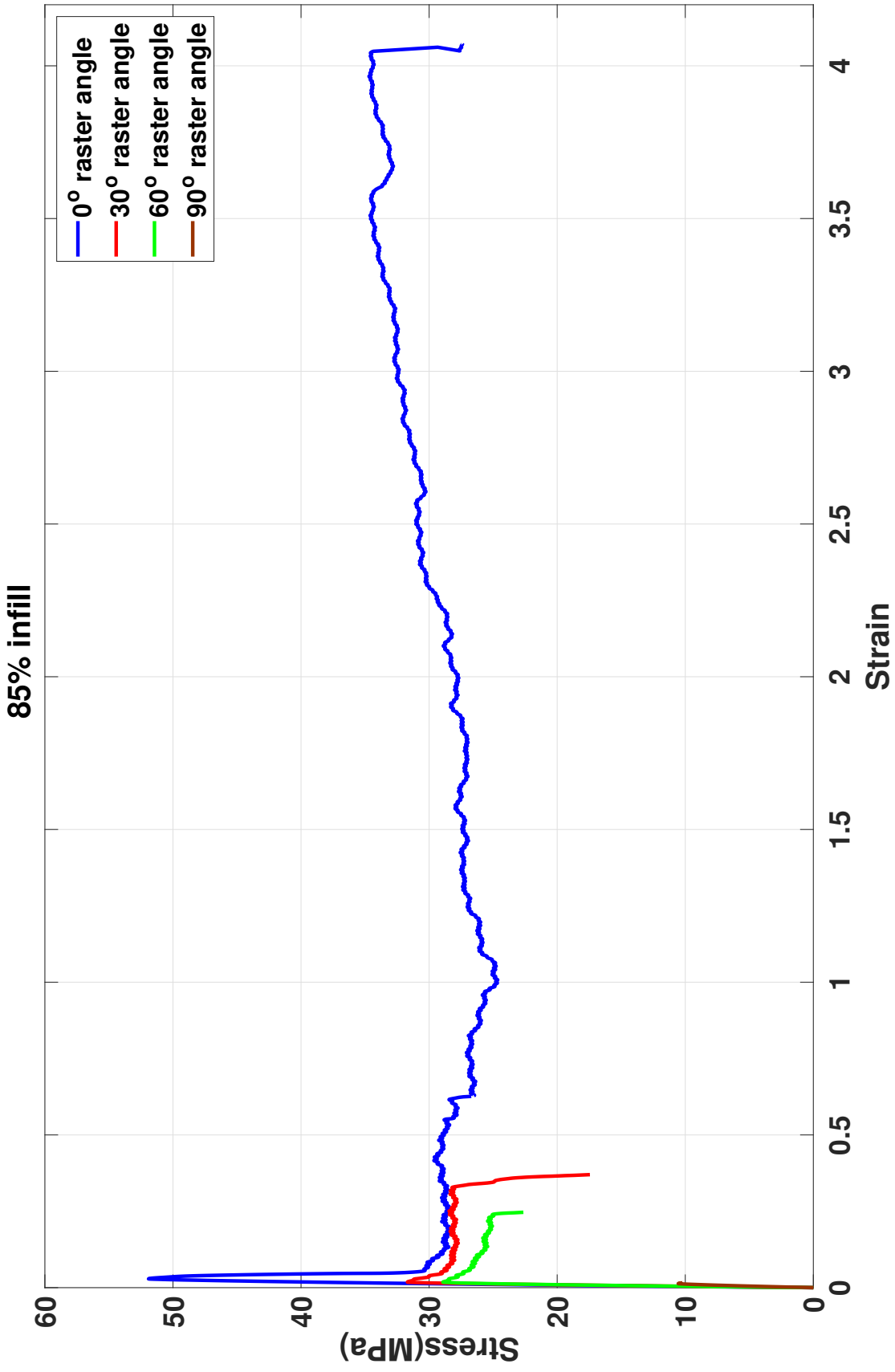

Figure 3.15: Representative stress-strain curves of each raster angle used in this thesis at 85% infill percentage.

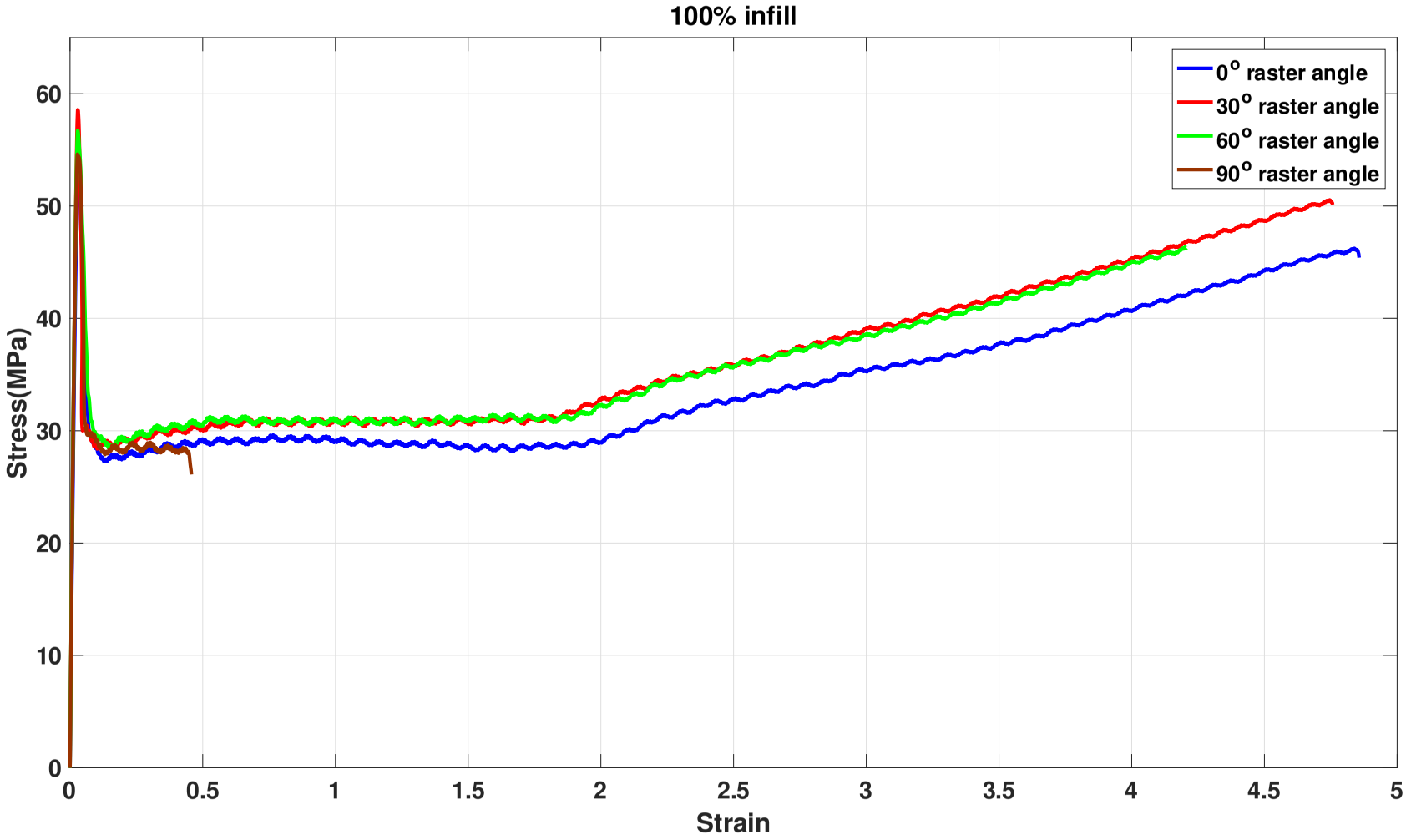

Figure 3.16: Representative stress-strain curves of each raster angle used in this thesis at 100% infill percentage.

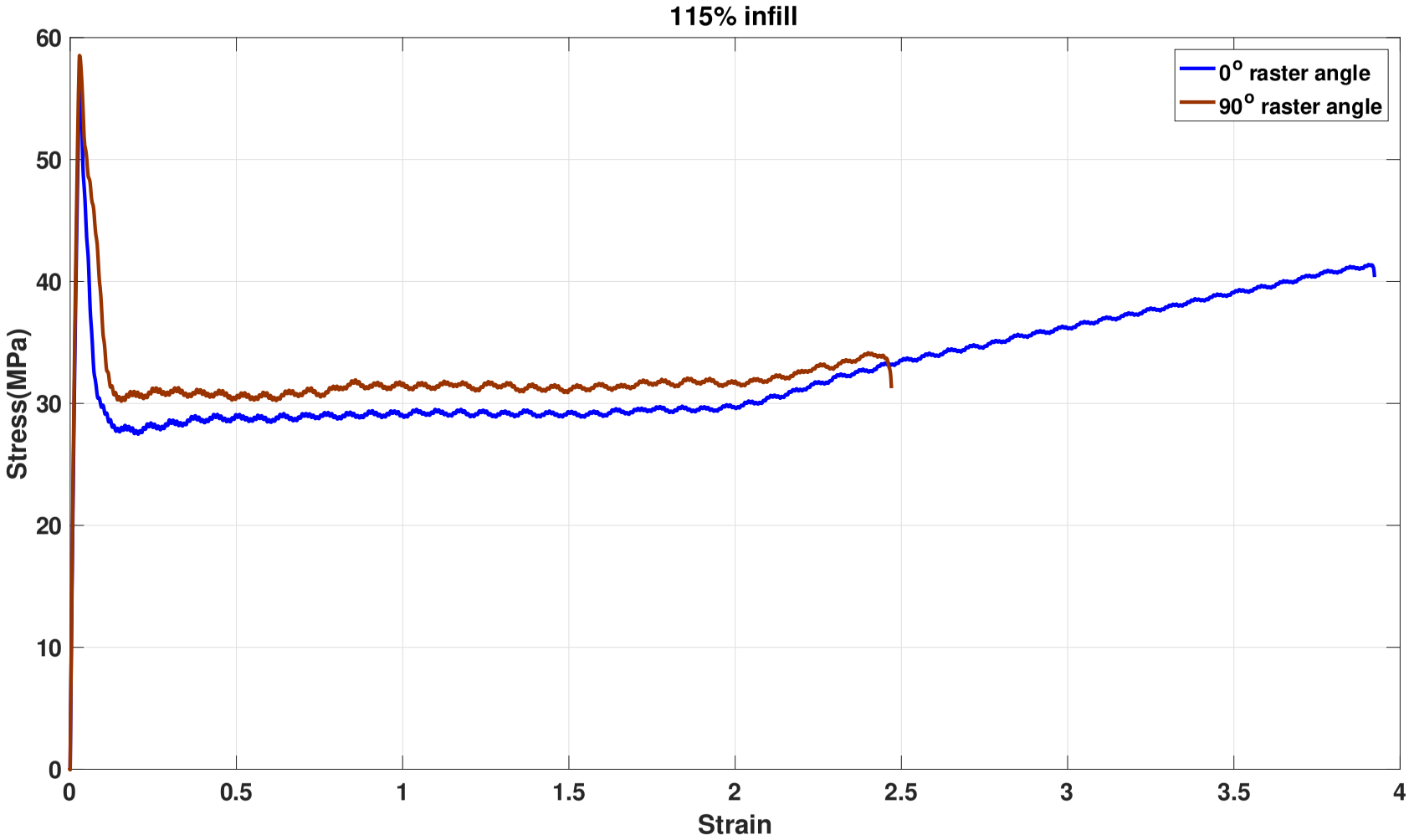

Figure 3.17: Representative stress-strain curves of each raster angle used in this thesis at 115% infill percentage.

3.5.1 Elastic Modulus (E)

Figure 3.18 shows the average and standard deviation of elastic modulus of samples with different raster angle and infill percentage. To better visualize the effect of raster angle, elastic modulus results are grouped under different infill percentages in this figure. The numerical values of Figure 3.18 are presented in Table 3.6.

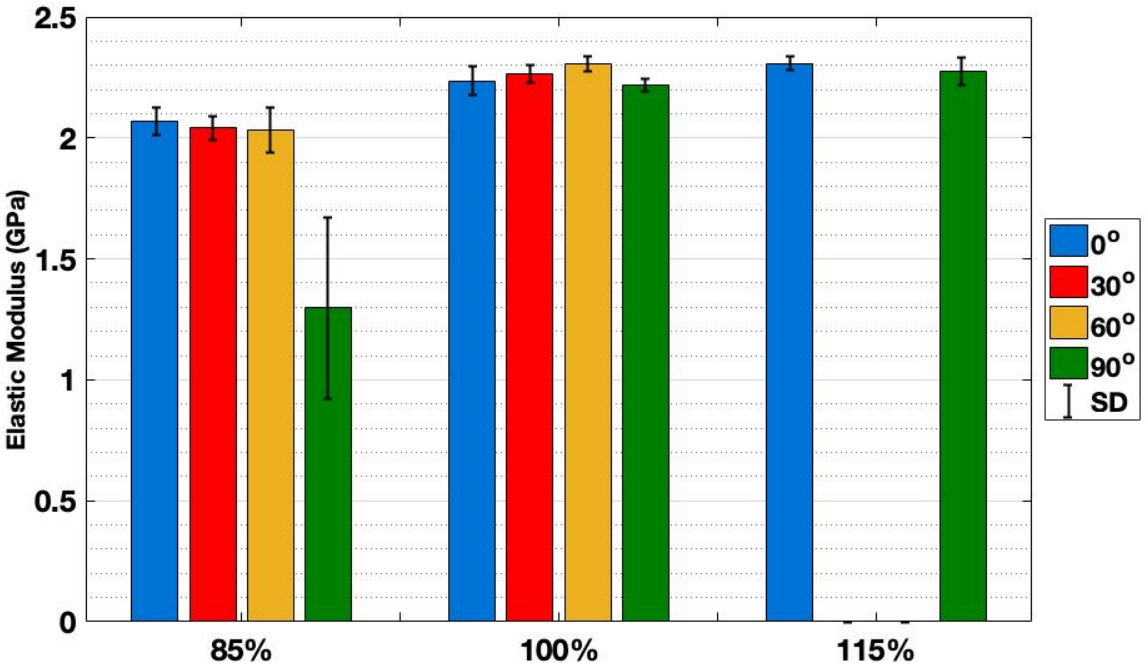

Figure 3.18: Elastic modulus (E) for different raster angle θ, grouped under different infill percentages.

Table 3.6: Average elastic modulus (± standard deviation) for different raster angles and infill percentages. Units are in GPa.

raster angle	85% Infill	100% Infill	115% Infill
0°	2.07 (±0.06)	2.24 (±0.06)	2.31 (±0.03)
30°	2.04 (±0.05)	2.26 (±0.04)	–
60°	2.03 (±0.09)	2.31 (±0.03)	–
90°	1.30 (±0.37)	2.22 (±0.03)	2.29(±0.06)

Considering the average results, 0° raster angle shows higher elastic modulus than 90° raster angle for all infill percentage. At 85% infill percentage, a decreasing trend

for the elastic modulus is observed as raster angle rises from 0° to 30° and 60°. Conversely, at 100% infill level elastic modulus slightly increases from 0° to 30° as well as 30° to 60° raster angle.

However taking standard deviation values into account, at 100% and 115% infill percentage, changing the raster angle between 0° and 90° does not have a statistically significant effect on the elastic modulus. Similarly, no statistical significant difference in elastic modulus is observed between 0°, 30° and 60° raster angle at any infill percentage. At 85% infill, 90° raster angle shows significantly reduced elastic modulus comparing to the 0° raster angle.

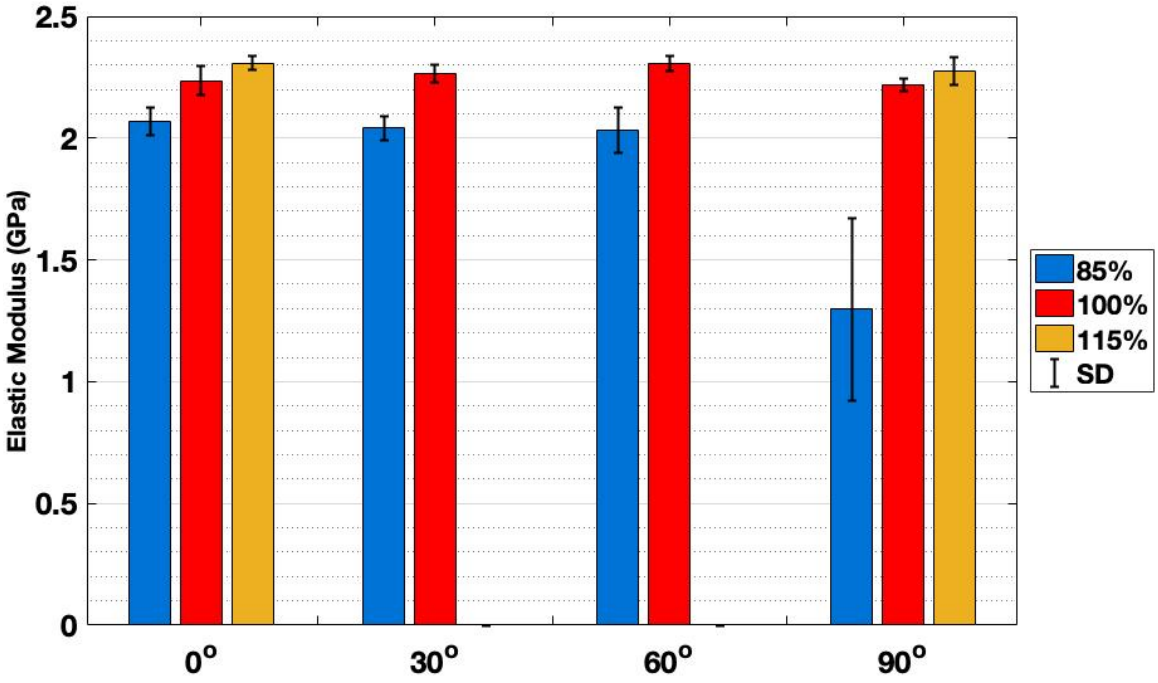

Figure 3.19: Elastic modulus (E) for different infill percentage, grouped under different raster angle.

To further illustrate the effect of infill percentage on elastic modulus, the results of Figure 3.18 are plotted again in Figure 3.19 but this time grouped under different raster angles. From the average values, it can be seen that elastic modulus increases with the increase of infill percentage level, for a fixed raster angle. The same trend is observed for all raster angles.

Moreover, considering standard deviation, it is clear that this trend is statistically significant. Also, the difference between 85% and 100% infill is much larger than the difference between 100% and 115% infill. This is specially more visible for 90° raster angle.

In summary, 0°, 30° and 60° raster angles demonstrate similar elastic modulus values in both 85% and 100% infill levels. In 100% infill even an increasing trend is observed as the raster angle rises from 0° to 60°. However, increasing the raster angle from 60° to 90° results in a significant drop in both 85% and 100% infill percentages. The main cause of this behaviour is the difference of 30° and 60° samples stack sequence from the 0° and 90° samples. For the samples with 0° and 90° raster angle, each layer raster direction is parallel to the rest of the sample layers. On the other hand, 30° and 60° samples are produced by stacking of layers with the raster angle of θ and $-\theta$ on top of each other. This leads to a criss-cross raster pattern of $[\theta/\text{-}\theta]_{4s}$ which is repeated in the 30° and 60° samples. The mentioned design is chosen to develop a symmetric stack sequence for 30° and 60° raster angle. As a result of this stack sequence, in the manufacturing process of 30° and 60° raster angle samples, each extruded filament slides transversely on top of the last layer beads. Since the sample layer height is extremely low (0.1 mm), extruded material partially penetrates into the air gaps which exists in the base layer as the fused material is deposited on top of these air gaps. This can provide reinforcement for the produced layers which leads to a better mechanical behaviour of the sample. Similarly, in many studies in the literature for other materials such as PLA and ABS, reported mechanical properties of criss-cross raster patterns (such as 30° and 60° raster angles) to be higher than axial raster angle (0° raster angle) [2, 50, 65, 67, 93]. Hence, it can be concluded that the reinforcement effect of criss-cross patterns is not restricted to the SMPs. Note that the layer thickness is relatively low (0.1 - 0.15 mm) in this thesis and the aforementioned studies.

Also, a significant drop in elastic modulus is observed between 60° and 90° raster

angle samples as 90° raster angle samples does not benefit from the aforementioned effect. In addition, decreasing infill percentage generally results in elastic modulus reduction with a fixed raster angle. This is due to the expansion of the air gap between neighbouring beads with the decrease in infill percentage.

3.5.2 Yield Strength (σ_y)

Figure 3.20 shows the average and standard deviation of yield stress (σ_y) of samples with different raster angles and infill percentages. To better visualize the effect of raster angle, yield stress results are grouped under different infill percentages in this figure. The numerical values of Figure 3.20 are presented in Table 3.7.

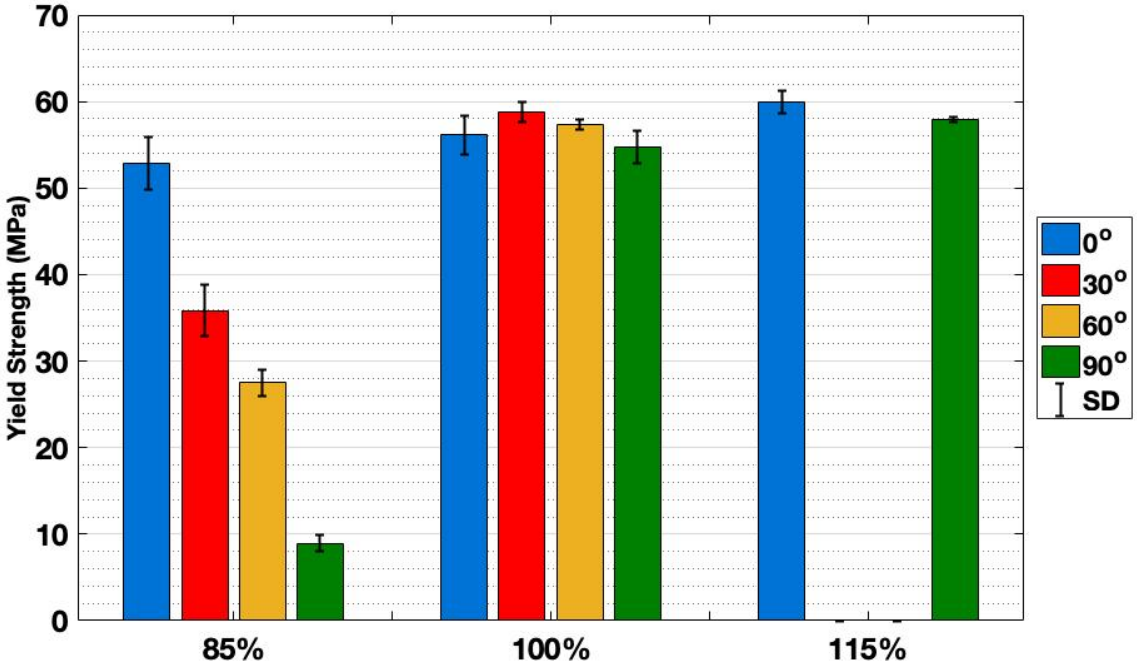

Figure 3.20: Yield strength (σ_y) grouped under different infill percentages.

Considering the average values, at 85% and 115% infill percentage, yield strength decreases with increase of raster angle. But the difference in the yield strength between different raster angles is much larger in 85% infill than that in 115% infill. Hence, this decreasing trend is more obvious for 85% infill percentage samples. 100% infill

Table 3.7: Average yield strength (± standard deviation) for different raster angles and infill percentages. Units are in MPa.

	85% Infill	100% Infill	115% Infill
0° raster angle	52.86 (±3.04)	56.12 (±2.22)	59.94 (±1.26)
30° raster angle	35.86 (±2.95)	58.76 (±1.12)	–
60° raster angle	27.48 (±1.50)	57.38 (±0.605)	–
90° raster angle	8.96 (±0.976)	54.68 (±1.88)	57.94(±0.296)

percentage samples are exception to this trend, where there is a slight increase in yield strength from 0° to 30° raster angle. However, taking standard deviation into consideration, in 100% infill samples there is no significant difference between 0°/60° and 0°/90° raster angles. Beside that, it is concluded that the effect of raster angel on yield strength is statistically significant.

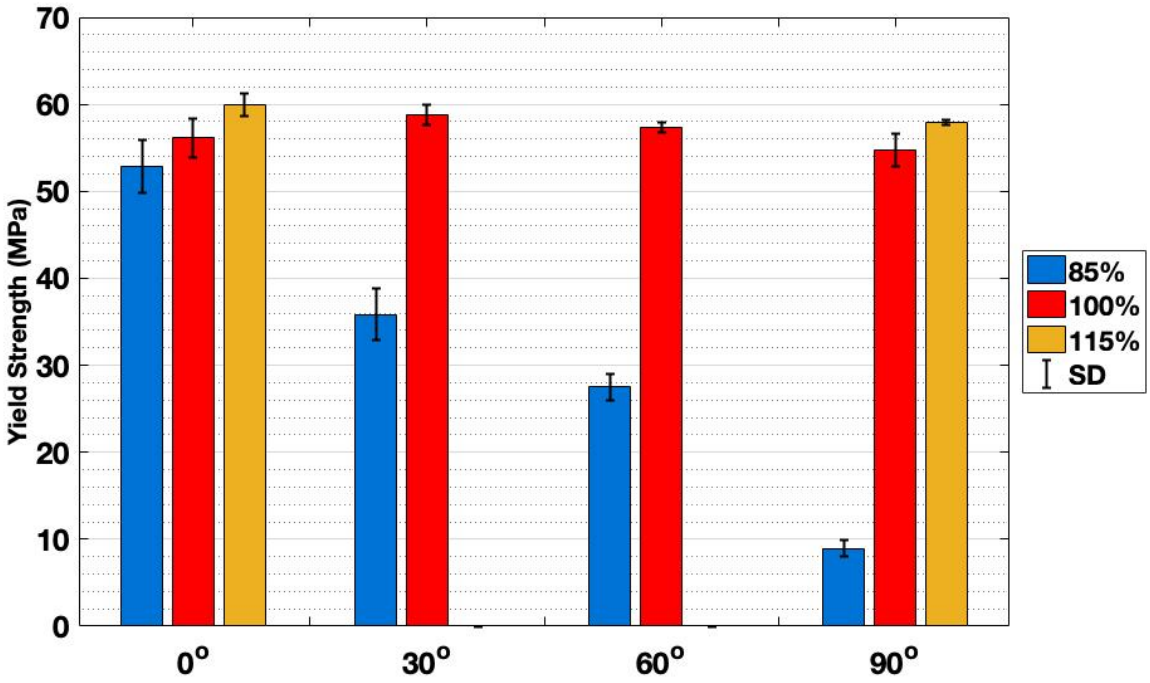

Figure 3.21: Yield strength (σ_y) grouped under different raster angles.

To further illustrate the effect of infill percentage on yield strength (σ_y), the results of Figure 3.20 are plotted again in Figure 3.21 but this time grouped under different raster angles.

Generally, reducing infill percentage leads to a lower yield strength as shown in Figure 3.21. Also, increasing raster angle amplifies the difference in the yield strength between 85% and 100% infill percentage samples. On the other hand, the influence of raster angel does not show a significant impact upon the yield strength contrast between 100% and 115% infill samples. Additionally, considering standard deviation values, there is a significant difference between different infill percentages, except for the difference between the 100% and 115% infill samples with 0° raster angle.

In summary, increasing the infill percentage and decreasing the raster angle are suggested for the applications which require high yield strength. Generally, the extension of the air gap between raster angels results in lower yield strength [94]. Hence, the effect of infill percentage on the yield strength can be explained with the presence of the air gap between neighboring beads which increases with the decrease of infill percentage. In contrary to infill percentage, raster angle does not always follow a similar trend in all infill percentages. For 85% and 115% infill percentage, higher raster angle results in lower yield strength. However, For 100% infill samples slight growth in yield strength is observed from 0° to 30° raster angle. The similar increasing trend can be found in the literature when the infill percentage is close to 100% (see [50] as a comparable example). Thus, it is concluded that criss-cross raster patterns such as 30° and 60° does show slightly better performance in terms of yield strength when the infill is close to 100%. On the other hand, criss-cross raster patterns does not have a significant advantage over parallel raster patterns such as 0° and 90° if the infill percentage below 100%.

3.5.3 Maximum Elongation ($EL\%$)

The effect of raster angle and infill percentage on the maximum elongation ($EL\%$) is shown in Figure 3.22. For better visualization, the results are grouped under different infill percentages. The numerical values of Figure 3.20 are presented in Table 3.8.

As shows in Figure 3.22, it is evident that raster angle plays a vital roll in the

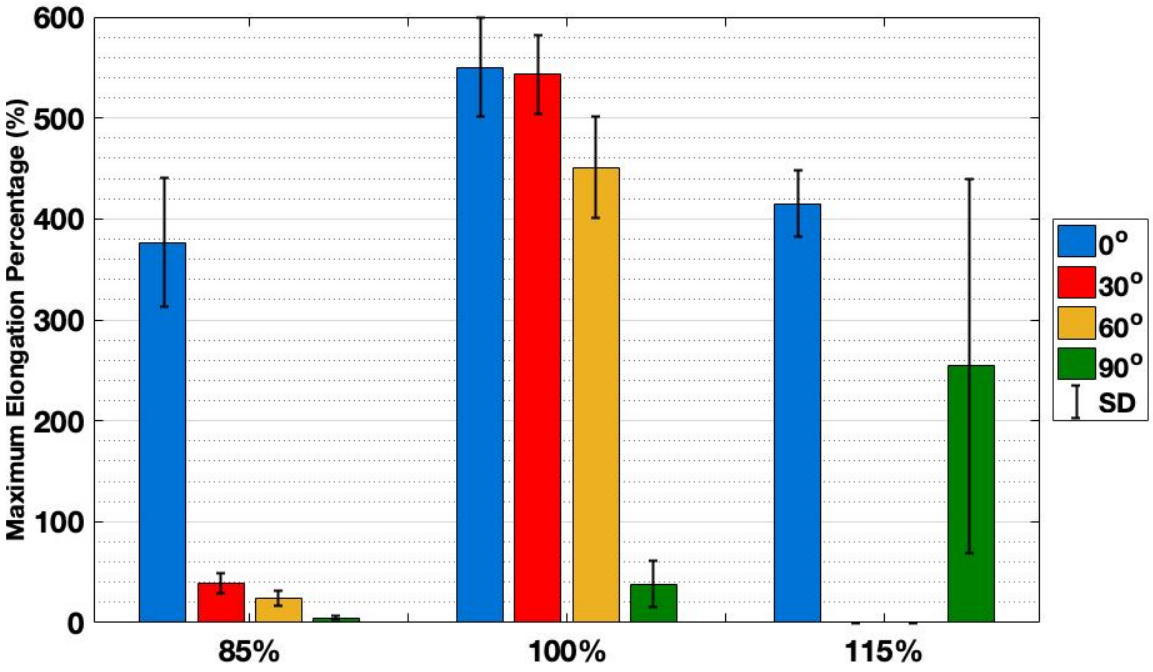

Figure 3.22: Maximum elongation percentage ($EL\%$) grouped under different infill percentages.

Table 3.8: Average maximum elongation percentage (± standard deviation) for different raster angles and infill percentages.

	85% Infill	100% Infill	115% Infill
0° raster angle	376.34 (±63.8)	549.88 (±48.9)	414.92 (±32.9)
30° raster angle	38.84 (±10.1)	543.02 (±39.4)	–
60° raster angle	23.94 (±7.72)	450.88 (±50.4)	–
90° raster angle	4.61 (±2.02)	38.16 (±23.1)	254.48 (±185.3)

maximum elongation of the sample. Although, with respect to the average values rising raster angle always leads to a decline in the maximum elongation without exception. However considering standard deviation, among 100% infill samples, raster angle does not make a significant impact on maximum elongation between 0° and 30°.

Figure 3.23 represent the same values as Figure 3.22 except that the data is grouped under different raster angles for more illustration. Comparing 85% and 100% infill samples demonstrate that 100% infill samples perform better in terms of maximum elongation ($EL\%$) in every raster angle. However the difference between the maximum elongation of 85% and 100% infill sample becomes less significant in 0° raster

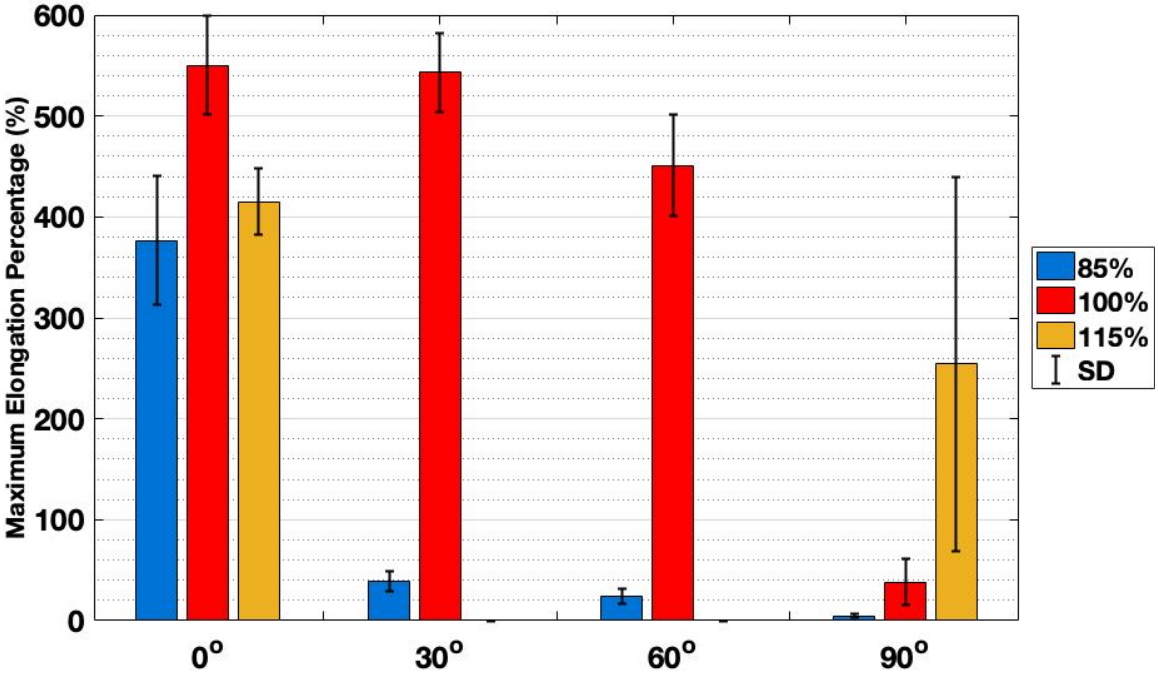

Figure 3.23: Maximum elongation percentage ($EL\%$) grouped under different raster angles.

angle compared to the other raster angles. Similarly, comparing 100% and 115% infill samples in Figure 3.23 indicates the strong impact of the raster angle on the maximum elongation. The raster angle influence is so significant that, in terms of maximum elongation 100% infill samples perform better than 115% infill percentage with 0° raster angle, while with 90° raster angle 100% infill samples reach much lower maximum elongation compared to 115% infill samples. Another notable observation in Figure 3.23 is the significant value of the standard deviation among sample with 90° raster angle compared to the average values. This means that 90° raster angle leads to reduced degree of certainty over maximum elongation percentage.

In summary, increasing raster angle always decreases the maximum elongation ($EL\%$) of the sample. The influence of the raster angel on the maximum elongation is due to the fact that the air gap between neighboring beads can act as a suitable place for crack initiation and growth [95]. Note that as the raster angle increase, a component of the force which is acting along the beads decreases while the compo-

nent of the force which is acting perpendicular to the beads increases. This causes higher probability of crack initiation and growth having greater raster angle. Infill percentage is also another important factor in the maximum elongation of the sample. Highest elongation percentage is observed in 100% infill percentage samples with 0° raster angle. However, this design is not suggested for the application which require high isotropic elasticity due to the low maximum elongation value of 100% infill sample with 90° raster angle. Criss-cross raster angles such as 30° and 60° raster angle samples in this study show less of anisotropic behaviour in 100% infill samples. It is also remarkable that at 100% infill level increasing or decreasing the infill percentage, reduces the ductility of the produced sample. This trend seems to be independent from the used material as similar trends is observed in the literature with different materials (see [66] as a related example). This can be due to the small gaps between neighboring beads at 100% infill percentage which results in less restriction imposed by neighbouring during deformation process. In other words, the deformation condition at 100% infill level is more closer to the plane-stress condition than plane-strain condition, comparing to 115% infill which contains almost no air gaps. On the other hand at 85% infill, the air gap is large enough to cause beads being almost separate from each other. Hence, any instability occurs in one of the beads during the deformation, almost no support is provided by neighboring beads, which makes each bead fail separately at lower elongation comparing to 100% infill level. However, this is a speculation and more investigation is needed to verify it.

3.5.4 Modulus of Resilience (U_r) and Tensile Toughness (U_T)

Elastic deformation energy (U_r), also known as *modulus of resilience*, represents the amount of energy absorbed per unit volume of sample during elastic deformation [96]. On the other hand, total deformation energy (U_T), also known as *tensile toughness*, represents the total amount of energy absorbed per unit volume of sample during the tensile test [96].

U_r and U_T are obtained by computing the area under the strain stress curve till yield strain and failure strain, respectively. These values are shown in Figures 3.24 and 3.25 for different raster angles and infill percentage. The data is grouped under different infill percentages to better illustrate the variations in U_r and U_T with respect to raster angle. Also the same data is shown in Figures 3.26 and 3.27 but grouped under different raster angles to better see the variation of absorbed energy with respect to infill percentage. The numerical values of resilience and toughness are also presented in Tables 3.9 and 3.10, respectively.

Table 3.9: Average values for modulus of resilience U_r ($\pm$ standard deviation) for different raster angles and infill percentages. Units of U_r are in $J/m^3 \times 10^5$.

raster angle	85% Infill	100% Infill	115% Infill
0°	9.1 ($\pm$1.039)	10.22 ($\pm$0.521)	10.25 ($\pm$0.79)
30°	4.6 ($\pm$0.811)	10.42 ($\pm$0.477)	–
60°	2.57 ($\pm$0.354)	10.22 ($\pm$0.124)	–
90°	0.58 ($\pm$0.173)	9.47 ($\pm$0.488)	9.49 ($\pm$0.165)

Table 3.10: Average values for tensile toughness U_T ($\pm$ standard deviation) for different raster angles and infill percentages. Units of U_T are in $J/m^3 \times 10^7$.

raster angle	85% Infill	100% Infill	115% Infill
0°	11.64 ($\pm$1.357)	20.96 ($\pm$2.615)	14.28 ($\pm$1.901)
30°	0.93 ($\pm$0.229)	21.4 ($\pm$1.981)	–
60°	0.46 ($\pm$0.19)	15.89 ($\pm$2.547)	–
90°	0.01 ($\pm$0.007)	0.89 ($\pm$0.641)	8.36 ($\pm$6.577)

Comparing Figure 3.24 with Figure 3.20, similar trends can be observed in U_r and yield strength. However, the effect of raster angle is magnified in U_r among 85% infill samples. Also the effect of infill percentage is slightly different in U_r, compared to yield strength. The difference in U_r between 85% and 100% infill samples is slightly increased compered to yield strength. On the contrary, the U_r values of 100% 115% infill samples of the same raster angle are nearly indistinguishable as shown in Figure 3.26.

On the other hand, as shows in Figure 3.25, U_T generally reflect similar trends

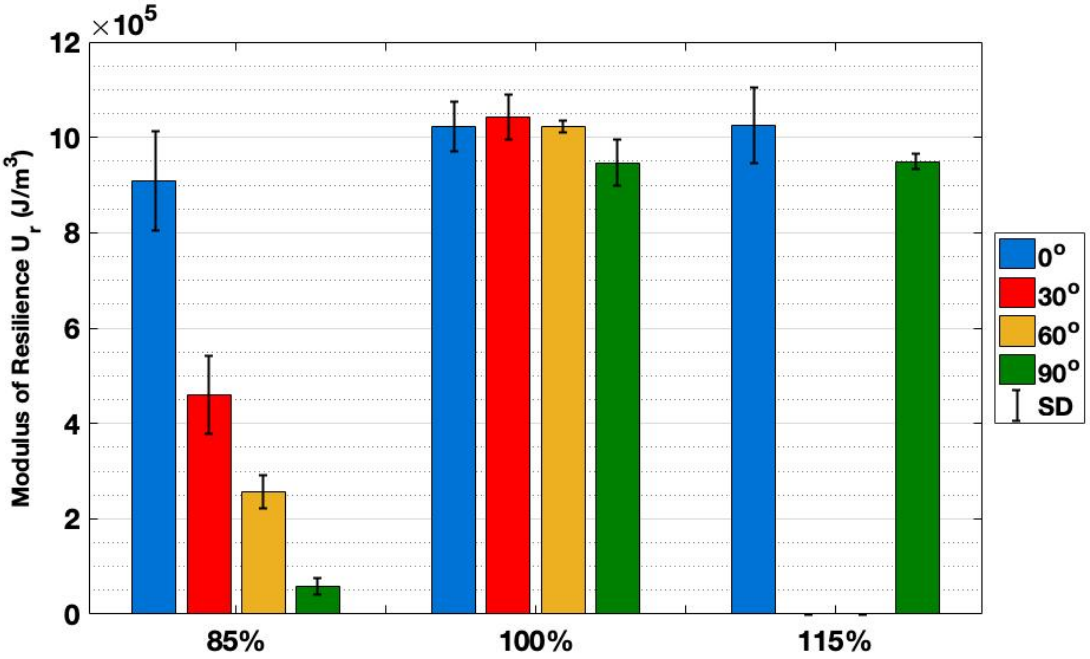

Figure 3.24: Modulus of resilience (U_r) grouped under different infill percentages.

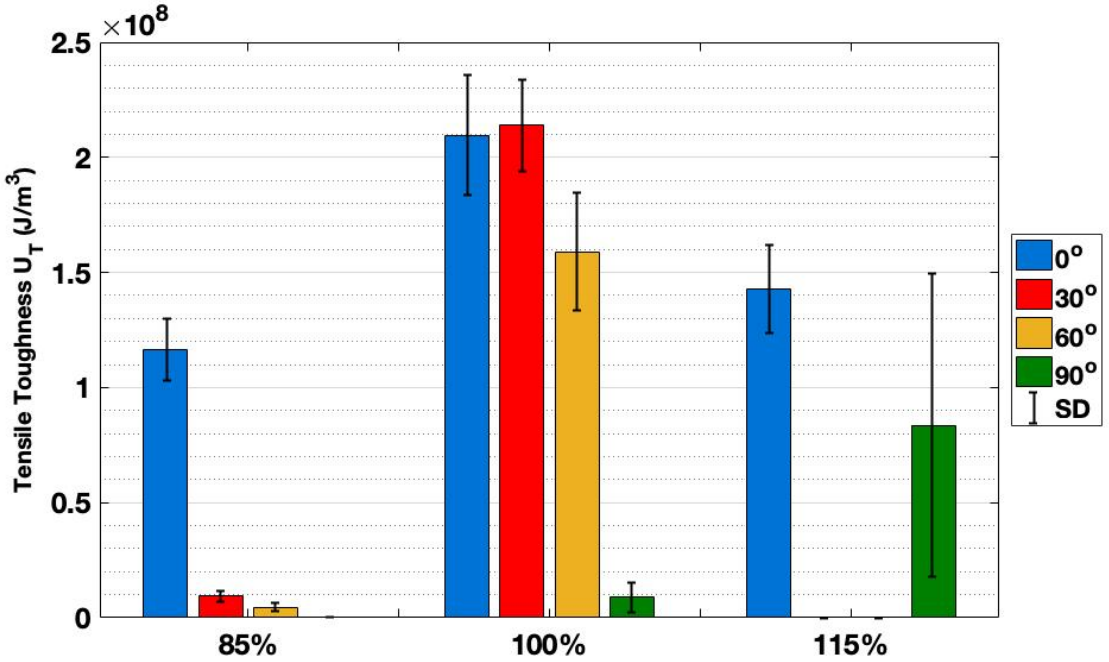

Figure 3.25: Tensile toughness (U_T) grouped under different infill percentages.

observed in maximum elongation percentage (Figure 3.22. This shows that the maximum elongation ($EL\%$) of the sample is the main governing factor in the tensile toughness of the sample. However, despite the similarities, the influence of raster an-

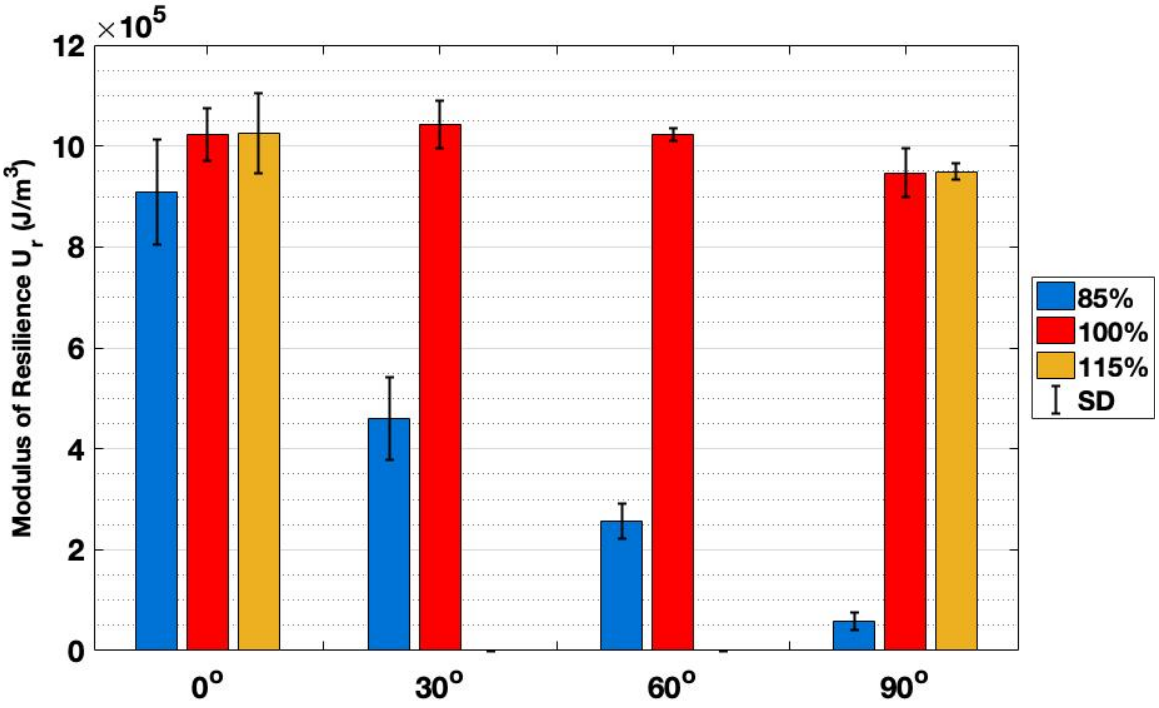

Figure 3.26: Modulus of resilience (U_r) under different raster angle.

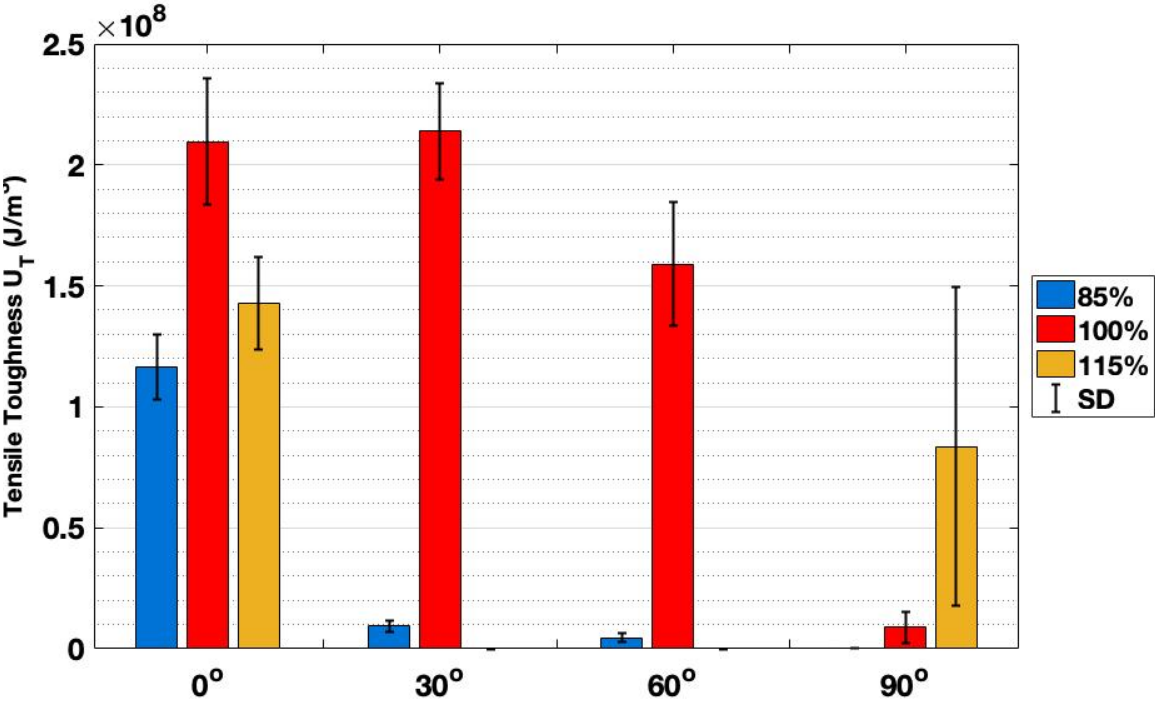

Figure 3.27: Tensile toughness (U_T) under different raster angle.

gle is slightly more expressive in Figure 3.25 compared Figure 3.22. Moreover, 100% infill samples reach higher elongation percentage with 0° raster angle than with 30°

raster angle. Whereas in Figure 3.25 for 100% infill, 30° raster angle obtain greater U_T value than 0° raster angle. Although none of the mentioned differences is significant considering the standard deviation for 100% infill samples with 0° and 30° raster angles.

In summary, it can be concluded that U_r and U_T show the same trend as of yield strength and elongation ($EL\%$), respectively, with minor differences in some details.

3.6 Conclusions

In this chapter the influence of infill percentage and raster angle on mechanical properties of MM4520 shape memory polymer (SMP), produced by extrusion-based additive manufacturing (EBAM) is investigated. In order to do so 120 samples in four different raster angle levels (0°, 30°, 60° and 90°) and three different infill percentage levels (85%, 100% and 115%) were produced and tested. From the tensile test measurements, elastic modulus (E), yield strength (σ_y), maximum elongation percentage ($EL\%$), modulus of resilience (U_r) and tensile toughness (U_T) are determined. According to the tensile test results, elastic modulus (E) does not show a remarkable variations with respect to the raster angle in both 100% and 115% infill samples. However in 85% infill percentage, notable drop in elastic modulus (E) is observed at 90° raster angle. The impact of infill percentage on elastic modulus is considerable in all raster angles. Moreover, the elastic modulus of different infill percentages in any raster angle is approximately proportional to the density of the product. Hence, for the applications that an isotropic load is applied, either infill percentage of 100% and above, or a criss-cross raster patterns between 30° to 60° raster angle is suggested. On the other hand, low infill samples with uni-directional raster patterns, exhibit an extremely anisotropic elastic modulus. Same suggestions is applied for tensile strength. However, criss-cross raster patterns are suggested to have an infill level close to 100% for the applications which require high tensile strength.

To summarize, elastic modulus (E), resilience (U_r) and yield strength (σ_y) of SMP

material produced by EBAM is not highly sensitive to the raster angle in 100% infill percentage and above.

Unlike elastic modulus, yield strength and resilience (E, σ_y,U_r), raster angle causes dramatic variation in maximum elongation ($EL\%$) and tensile toughness (U_T) of the produced sample. However, the impact of raster angle magnifies with the reduction of infill percentage. Also, 100% infill samples with 0°, 30° and 60° raster angles, are superior compared to 85% and 115% infill samples in terms of deformability. Hence, for high energy absorption, 100% infill with 0° raster angle for uni-directional loading condition and 100% infill with criss-cross raster patter such as 30° and 60° are suggested.

Chapter 4

Classical Laminated Plates Theory for Shape Memory Polymers Produced by Extrusion-Based Additive Manufacturing

4.1 Introduction

As a result of recent technological advancements in extrusion-based additive manufacturing (EBAM), potential applications of this technique are not just limited to creation of concept models and visualization aids. Instead, there are growing appeals for functional parts fabricated by EBAM [4, 97]. In order to design and create a viable functional product with EBAM method, it is crucial to have a deep understanding of mechanical behaviour of fabricated end-parts. Thus, mechanical properties of EBAM produced parts are getting increasing attention [98]. However, understanding these properties is typically a complex task since each combination of numerous fabrication parameters in EBAM (such as layer thickness, infill, raster angle, raster pattern, air gaps, etc.) may lead to a different mechanical behaviour in the product [2]. Hence, in recent years, several researchers have been working on this issue [50, 85–88]. However, the correlation between EBAM designated fabrication parameters and the mechanical behaviour of product has rarely been studied using analytical approach. The majority of studies in this field attempt to tackle this issue by experimental inves-

tigation (see the review paper [2] and the references therein). Although empirical approach can provide a comprehensive solution to this matter, it is often associated with several disadvantages. First of all the process is time consuming and thus it requires a significant amount of effort to be devoted to that. Besides experimental setups are often expensive and obtaining meaningful experimental results is generally costly. Furthermore, with the obtained experimental results, it is quite difficult to extrapolate the results to different EBAM parameters [12]. Thus, a handful of studies in literature develop an analytical model to predict the final mechanical behaviour of the specimens according to some of the production parameters [12, 81].

In this context, classical laminated plate theory (CLPT), can be used as a simple yet effective pathway to a realistic solution to an analytically predictive model for mechanical behaviour of EBAM parts. CLPT is a well known theory which has been applied to similar domains [43]. The main reason of using CLPT on this subject is the fact that EBAM parts are built in layers which are known to have anisotropic mechanical behaviour [99]. Using CLPT, elastic modulus of equivalent single layer of a multi-layered part can be obtained from stiffness matrix $[Q]$ and the stack sequence of layers. In order to form $[Q]$ four mechanical properties (E_1, E_2, G_{12} and ν_{12}) from a single layer is required. Hence, in order to use CLPT for EBAM samples, E_1, E_2, G_{12} and ν_{12} of EBAM single layer is needed.

To the best of my knowledge, only one study used CLPT to describe the mechanical behaviour of EBAM produced parts [12]. In this study, Casavola et al. [12] used CLPT to express the mechanical behaviour of PLA (polylactic acid) and ABS (polyacrylonitrile butadiene styrene) created by EBAM technique. Additionally, Casavola et al. [12] compared the CLPT predictions with the experimental results of [30/-30/0/-30/30] stack sequence on both materials and conclude that the CLPT has demonstrated a high capacity to predict the elastic modulus of EBAM parts made by PLA and ABS [12]. However, the model presented in [12] requires all four aforementioned mechanical properties to be obtained experimentally. This impacts

the simplicity of using CLPT model since values of G_{12} and ν_{12} are often difficult to obtain experimentally [12]. Whereas in this work, only E_1, E_2 are required to be obtained experimentally.

Another major drawback of [12] is that their experimental samples are produced in dogbone shape with two contour lines for the shell. Note that the contour lines are independent of raster angle as described in Chapter 3. Thus, in the dogbone gauge length, contour lines are always parallel to the direction of the force. Having different filament orientations in the gauge length leads to fundamental error in experimental investigation of the effect of raster angle on mechanical properties of the produced part. This issue is addressed in this work by removing the outer shell of the samples with machining. Additionally, some modifications for CLPT is suggested using two compensation factors in order to achieve more accurate predictions for EBAM samples.

4.2 Methodology

CLPT is the simplest equivalent single layer (ESL) model and it has been developed to predict the mechanical properties of the EBAM sample (or laminate) based on the mechanical properties of each single ply (or lamina) [43].

4.2.1 Assumptions for the Analysis

The following assumptions are considered in this study:

Assumption (A1): The CLPT model is based on the Kirchhoff–Love hypothesis [100], assuming that a straight line perpendicular to the mid-plane still remain straight and perpendicular to the mid-plane after deformation. This means that both shear and normal deformation effects are ignored [41]. Moreover, in CLPT the laminate is thin and under a plane stress state.

Assumption (A1) is that elastic properties of a **single ply** can be characterized by the following four parameters [43]:

- E_1 : elastic modulus in raster direction.
- E_2 : elastic modulus perpendicular to raster direction.
- G_{12} : in-plane shear modulus.
- ν_{12} : major Poisson's ratio

Note that minor Poisson's ratio (ν_{21}) can be calculated from E_1, E_2 and ν_{12} as follows:

$$\frac{\nu_{12}}{E_1} = \frac{\nu_{21}}{E_2}$$

Given E_1, E_2, G_{12} and ν_{12}, the stiffness matrix Q of a single ply is then computed as follows [43]:

$$Q = \begin{bmatrix} Q_{11} & Q_{12} & 0 \\ Q_{12} & Q_{22} & 0 \\ 0 & 0 & Q_{66} \end{bmatrix}, \tag{4.1}$$

where

$$\begin{aligned} Q_{11} &= \frac{E_1}{1 - \nu_{12}\nu_{21}}, \\ Q_{12} &= \frac{\nu_{21}E_1}{1 - \nu_{12}\,\nu_{21}} = \frac{\nu_{12}E_2}{1 - \nu_{12}\,\nu_{21}}, \\ Q_{22} &= \frac{E_2}{1 - \nu_{12}\,\nu_{21}}, \\ Q_{66} &= G_{12} \end{aligned}$$

Out of these 4 parameters, E_1 and E_2 are directly determined from the tensile test results of 0° and 90° raster angle, respectively. These values, reported before in Chapter 3, are presented again in Table 4.1 for ease of reference.

G_{12} can be determined with lamina micro-mechanical analysis using a few assumptions. In this study, uni-directional raster pattern are used. With this raster pattern, each printed layer is built by stacking deposited beads side by side as shown in Figure 4.1. As a natural consequence of this manufacturing approach, adhesive force

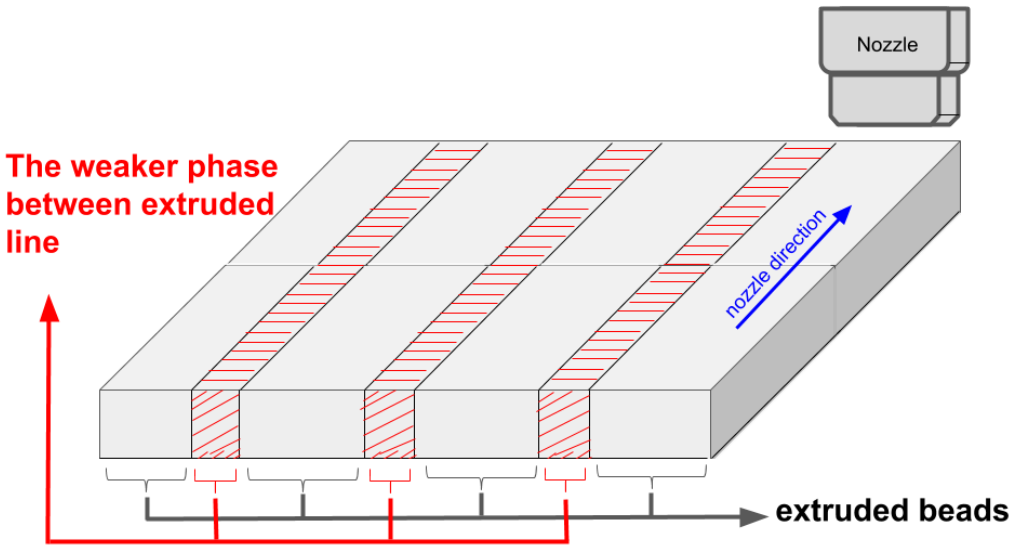

Figure 4.1: Illustration of a single printed layer (ply) and the weaker phase between the extruded lines.

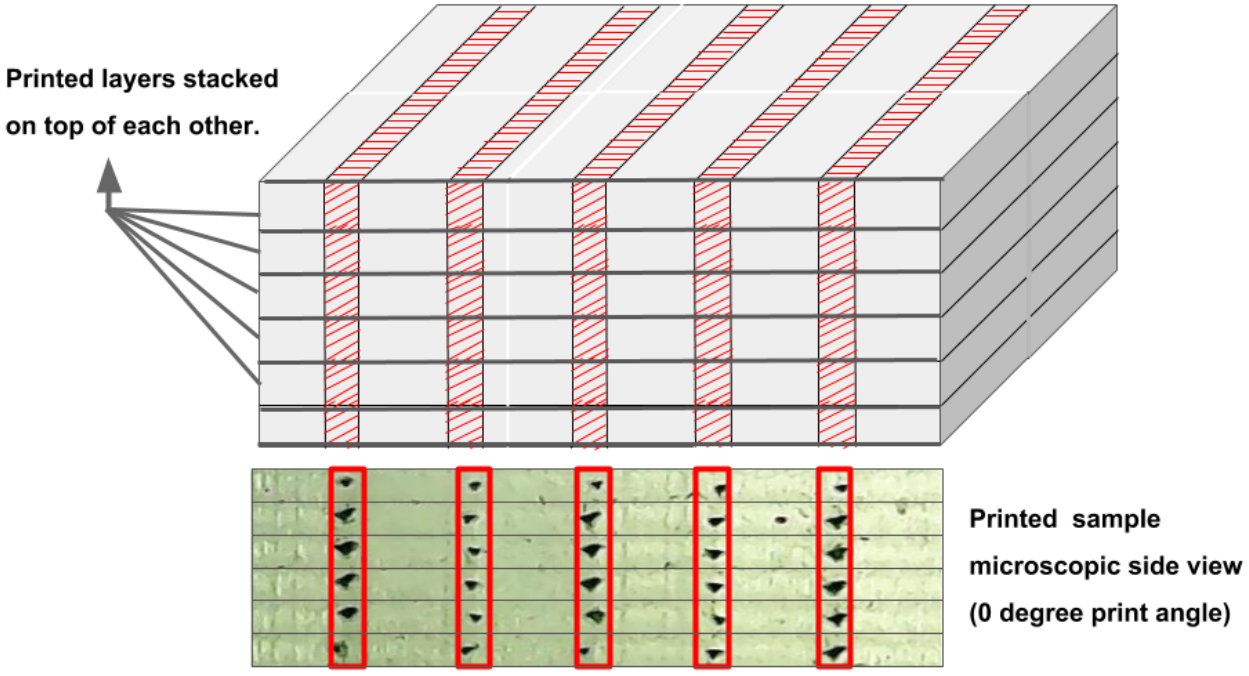

Figure 4.2: Stack of printed layers (top), and microscopic cross section of stack of layers produced by EBAM (bottom). Red rectangles contain the weak phases. Air gaps (black irregular holes) can be observed in weak phases.

Table 4.1: E_1 and E_2 values obtained from experimental results at 0° and 90° raster angle.

Infill Percentage	E_1 (GPa)	E_2 (GPa)
85%	2.07	1.30
100%	2.24	2.22
115%	2.31	2.29

acting at the interface between neighboring beads is typically weaker compared to the extruded material [101]. In addition, depending on the infill percentage, air gap can be formed in the weak phase between neighboring beads as shown in Figure 4.2.

Assumption (A2): It is assumed that each printed layer consists of two continuous and isotropic phases: (i) *extruded beads* and (ii) *weak-phase* between extruded beads, as illustrated in Figures 4.1 and 4.2. Subscript b is used hereafter to denote extruded beads properties and subscript w is used hereafter to denote weak-phase properties.

Assumption (A3): Elastic modulus of extruded beads (E_b) is assumed to be equal to the elastic modulus of samples with 115% infill and 0° raster angle. In other words, $E_b = E_1$(@115% Infill), where this value can be read from Table 4.1.

Let E_w and v_w denote the elastic modulus and volume fraction of the weak phase, respectively. Based on assumptions (A1)-(A3) and the rule of mixture for a single ply, it follows that [43]:

$$E_1 = E_b(1 - v_w) + E_w v_w \tag{4.2}$$

$$\frac{1}{E_2} = \frac{1 - v_w}{E_b} + \frac{v_w}{E_w} \tag{4.3}$$

Since E_1 and E_2 are known (from Table 4.1), there are two unknown variables (E_w, v_w) in Equations (4.2) and (4.3). Numerical values of E_w and v_w can be obtained by simultaneously solving Equations (4.2) and (4.3). The computed values are reported in Table 4.2 for different infill percentages.

Note that v_w values from Table 4.2 implies that, the weak phase takes 10.9 % and

Table 4.2: E_w and v_w obtained by solving Equations (4.2) and (4.3).

Infill Percentage	E_w(MPa)	v_w
85%	261.2	0.1090
100%	1723.6	0.0959

9.5 % of the volume of a single ply in 85 % and 100 % infills, respectively. Also, as expected E_w at 85% infill is much lower than that of 100% infill. These values signify that assumption (A3) is reasonable.

Assumption (A4): ν_{12} of the ply is assumed to be the same as the Poisson's ratio of an extruded bead (ν_b), i.e.

$$\nu_{12} = \nu_b \tag{4.4}$$

From the rule of mixture and using the fact that $v_b = 1 - v_w$, it follows that

$$\nu_{12} = \nu_w \, v_w + \nu_b(1 - v_w) \tag{4.5}$$

Substituting Equation (4.4) in Equation (4.5), results in

$$\nu_w = \nu_b \tag{4.6}$$

Later in Section 4.3.3, this assumption will be examined with experimental results and modified accordingly.

Let G_w and G_b denote shear modulus of weak phase and extruded beads, respectively. Then, from Assumption (A2) [43] it follows that

$$G_b = \frac{E_b}{2(1 + \nu_b)} \tag{4.7}$$

$$G_w = \frac{E_w}{2(1 + \nu_w)} \tag{4.8}$$

Now, substituting Equation (4.6) in Equations (4.7) and (4.8), it can be concluded the ratio of G_w to G_b is equal to the ratio of E_w to E_b. In other words:

$$\frac{E_w}{E_b} = \frac{G_w}{G_b} \tag{4.9}$$

With the given G_b and G_w, the shear modulus of a single ply (G_{12}) can be obtained according to the rule of mixture as [43]:

$$\frac{1}{G_{12}} = \frac{1 - v_w}{G_b} + \frac{v_w}{G_w} \tag{4.10}$$

Assumption (A5): As the final assumption, ν_b of an extruded bead is assumed to be the same as the material Poisson's ratio (ν), i.e.

$$\nu_b = \nu \tag{4.11}$$

The material used in this study is MM4520, a polyurethane-based shape memory polymer. However, the exact value of Poisson ratio of MM4520 has not been reported. It is assumed that ν of MM4520 is equal to the Poisson's ratio of its base polymer, which is polyurethane, and thus from [102, 103]:

$$\nu_b = \nu_{MM4520} = \nu_{polyurethane} = 0.42 \tag{4.12}$$

While $\nu = 0.42$ is used, later in Section 4.3.1 sensitivity analysis of the results with respect to ν is performed where the analysis justifies the choice of ν.

With the given ν, value for G_{12} can now be computed from Equations (4.7) and (4.10) based on assumptions (A4) and (A5). The numerical results of shear modulus of ply are reported in Table 4.3.

Table 4.3: Calculated shear modulus (G_{12}) for different infill percentages.

Infill Percentage	G_b (MPa)	G_w (MPa)	G_{12} (MPa)
85%	807	91.3	435.2
100%	807	602.6	781.6
115%	807	-	807

4.2.2 Analysis of the EBAM Sample by Stacking Plies

Having all four parameters of a ply (E_1, E_2, G_{12}, ν_{12}), the stiffness matrix Q of a ply can be computed from Equation (4.1).

Assumption (A1) signifies that for the laminate only three in-plane stress components, σ_x, σ_y and τ_{xy} are considered. The stresses σ_x, σ_y and τ_{xy} can be integrated over the thickness into resultant forces (N) and moments (M) per unit length as follows [43]:

$$N = \begin{bmatrix} N_x \\ N_y \\ N_{xy} \end{bmatrix} = \int_h \begin{bmatrix} \sigma_x \\ \sigma_y \\ \tau_{xy} \end{bmatrix} dz \tag{4.13}$$

$$M = \begin{bmatrix} M_x \\ M_y \\ M_{xy} \end{bmatrix} = \int_h \begin{bmatrix} \sigma_x \\ \sigma_y \\ \tau_{xy} \end{bmatrix} z dz \tag{4.14}$$

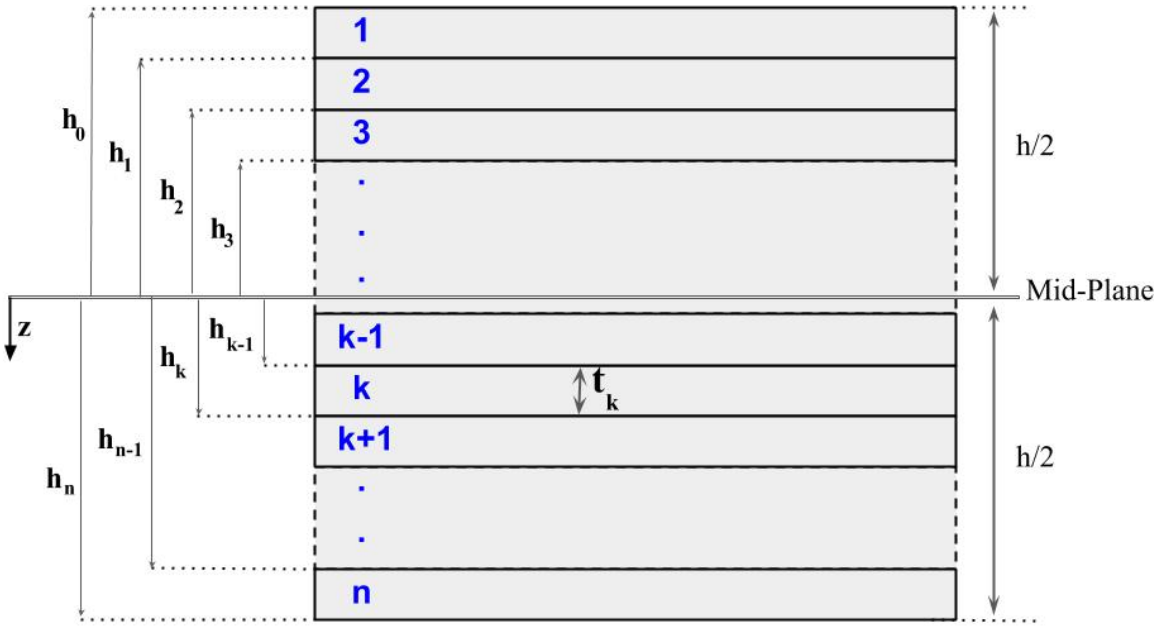

Figure 4.3: Coordinate locations of plies.

Consider n plies, stacked on top of each other with the total thickness of h as shown in Figure 4.3. Then, set the mid-plane as an x-y plane in the middle of top and bottom surface of stacked plies with the z-axis downward (see Figure 4.3). The z-coordinate of ply k, is expressed with the distance between mid-plane to its top surface h_{k-1} and bottom surface h_k:

$$
\begin{array}{lll}
ply\,1 & \text{between} & h_0, h_1 \\
ply\,2 & \text{between} & h_1, h_2 \\
 & \vdots & \\
ply\,k & \text{between} & h_{k-1}, h_k \\
 & \vdots & \\
ply\,n & \text{between} & h_{n-1}, h_n
\end{array}
$$

Based on assumption (A1), CLPT relates the applied forces N and moments M to the resulting strains ϵ^0 and the curvatures κ of the mid-plane [43]:

$$
\begin{bmatrix} N \\ M \end{bmatrix} = \begin{bmatrix} A & B \\ B & D \end{bmatrix} \begin{bmatrix} \epsilon^0 \\ \kappa \end{bmatrix} \tag{4.15}
$$

with

$$
A = \sum_{k=1}^{n} \bar{Q}(\theta_k)(h_k - h_{k-1}) \tag{4.16}
$$

$$
B = \frac{1}{2} \sum_{k=1}^{n} \bar{Q}(\theta_k)(h_k^2 - h_{k-1}^2) \tag{4.17}
$$

$$
D = \frac{1}{3} \sum_{k=1}^{n} \bar{Q}(\theta_k)(h_k^3 - h_{k-1}^3) \tag{4.18}
$$

The A, B, and D matrices are called the extensional, coupling, and bending stiffness matrices, respectively [43]. Note that $\bar{Q}(\theta_k)$ for k-th ply in Equations (4.16) to (4.18), is the transformed reduced stiffness matrix according to the ply angle θ_k. Hence, for a given θ_k, $\bar{Q}(\theta_k)$ can be computed from the stiffness matrix Q in Equation (4.1) from the following transformation [43]:

$$
\bar{Q}(\theta_k) = \begin{bmatrix} \bar{Q}_{11} & \bar{Q}_{12} & \bar{Q}_{16} \\ \bar{Q}_{12} & \bar{Q}_{22} & \bar{Q}_{26} \\ \bar{Q}_{16} & \bar{Q}_{26} & \bar{Q}_{66} \end{bmatrix} \tag{4.19}
$$

where,

$$\bar{Q}_{11} = Q_{11}c^4 + Q_{22}s^4 + 2(Q_{12} + 2Q_{66})s^2c^2 \tag{4.20}$$

$$\bar{Q}_{12} = (Q_{11} + Q_{22} - 4Q_{66})s^2c^2 + Q_{12}(c^4 + s^2) \tag{4.21}$$

$$\bar{Q}_{22} = Q_{11}s^4 + Q_{22}c^4 + 2(Q_{12} + 2Q_{66})s^2c^2 \tag{4.22}$$

$$\bar{Q}_{16} = (Q_{11} - Q_{12} - 2Q_{66})c^3s - (Q_{22} - Q_{12} - 2Q_{66})s^3c \tag{4.23}$$

$$\bar{Q}_{26} = (Q_{11} - Q_{12} - 2Q_{66})s^3c - (Q_{22} - Q_{12} - 2Q_{66})c^3s \tag{4.24}$$

$$\bar{Q}_{66} = (Q_{11} + Q_{22} - 2Q_{12} - 2Q_{66})c^2s^2 + Q_{66}(s^4 + c^4) \tag{4.25}$$

with $c = \cos(\theta_k)$, $s = \sin(\theta_k)$.

When the thickness of all plies are constant, i.e. $t_k = \frac{h}{n}$, Equations (4.16) to (4.18) for A, B, and D matrices can be simplified as follows:

$$A = \frac{h}{n}\sum_{k=1}^{n}\bar{Q}(\theta_k) \tag{4.26}$$

$$B = \frac{h^2}{2n^2}\sum_{k=1}^{n}(2k - n - 1)\,\bar{Q}(\theta_k) \tag{4.27}$$

$$D = \frac{h^3}{12n^3}\sum_{k=1}^{n}\big[12k(k - n - 1) + 4 + 3n(n + 2)\big]\bar{Q}(\theta_k) \tag{4.28}$$

Then by inverting Equation (4.15), the deformation can be calculated from N and M. To simplify the notations, the three matrices that appear in Equation (4.15), A, B and D, can be directly inverted as follows [12].

$$\begin{bmatrix}\epsilon^0\\ \kappa\end{bmatrix} = \begin{bmatrix} A & B\\ B & D\end{bmatrix}^{-1}\begin{bmatrix}N\\ M\end{bmatrix} = \begin{bmatrix} A^* & B^*\\ B^{*T} & D^*\end{bmatrix}\begin{bmatrix}N\\ M\end{bmatrix} \tag{4.29}$$

where B^{*T} is the transpose of B^* and

$$A^* = (A - BD^{-1}B)^{-1} \tag{4.30}$$

$$B^* = (D - BA^{-1}B)^{-1} \tag{4.31}$$

$$D^* = -A^*BD^{-1} \tag{4.32}$$

Finally, equivalent elastic modulus of the laminate in the longitudinal direction ($E_{1_{equivalent}}$) can be obtained from [12]:

$$E_{1_{equivalent}} = \frac{1}{h\, A^*_{11}} \tag{4.33}$$

where A^*_{11} is the element in the first row and first column of A^*.

Note that in this study, a symmetric stack sequence is used for printing the EBAM samples. Hence, for θ =30° and θ =60° raster angle samples, symmetric stack sequence is:

$$[\theta/\text{-}\theta]_{4s} := [\underbrace{\theta/\text{-}\theta/\cdots/\theta/\text{-}\theta}_{8} \;/\; \underbrace{\text{-}\theta/\theta/\cdots/\text{-}\theta/\theta}_{8}] \tag{4.34}$$

Figure 4.4 illustrates the symmetric stack-sequence for different raster angles used in this thesis.

Algorithm 1 summarizes the detailed steps in computation of equivalent elastic modulus of EBAM sample based on CLPT model.

Algorithm 1 Computation of equivalent elastic modulus $E_{1_{equivalent}}$ using CLPT model

`Input:` number of ply: n
total thickness: h
stack sequence: [θ/-θ]
shape memory polymer Poisson's ratio: ν
infill percentage parameter

`Output:` $E_{1_{equivalent}}$

1. For the given infill percentage parameter, set E_1, E_2 from Table 4.1
2. Set E_b to be equal to E_1 from step 1
3. Compute E_w, v_w by simultaneously solving Equations (4.2) and (4.3)
4. set $\nu_{12} = \nu$ from Equations (4.4) and (4.12) based on Poisson's ratio of the shape memory polymer
5. Compute G_b from Equation (4.7)
6. Compute G_w from Equation (4.9)
7. Compute G_{12} from Equation (4.10)
8. Compute Q from Equation (4.1)
9. Based on the given stack sequence, find θ_k for each ply and then compute $\bar{Q}(\theta_k)$ from Equations (4.19)-(4.25)
10. Compute A, B, D from Equations (4.26)-(4.28)
11. Compute A^* from Equation (4.30)
12. Compute $E_{1_{equivalent}}$ from Equation (4.33)

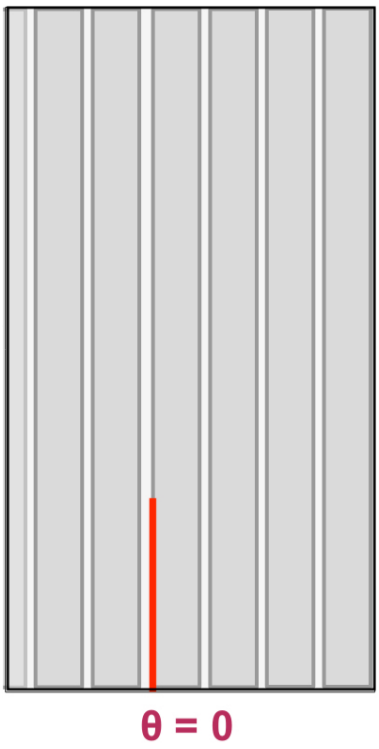

(a) 0° raster angle.

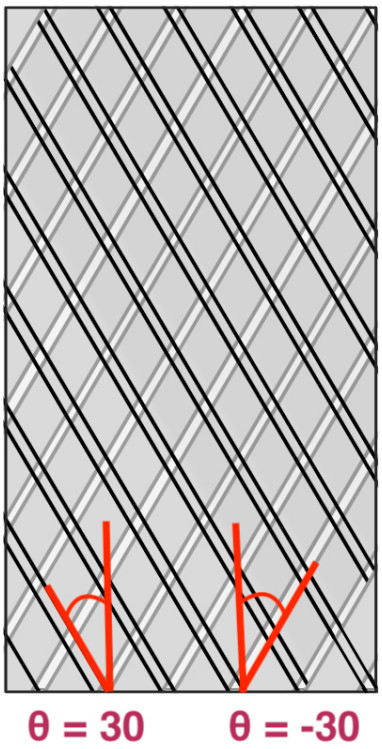

(b) 30° raster angle.

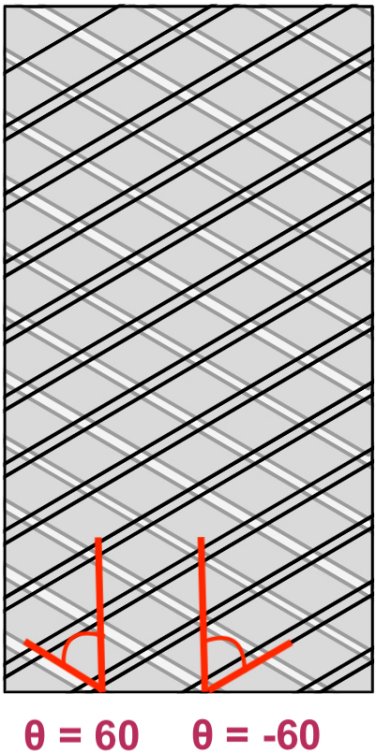

(c) 60° raster angle.

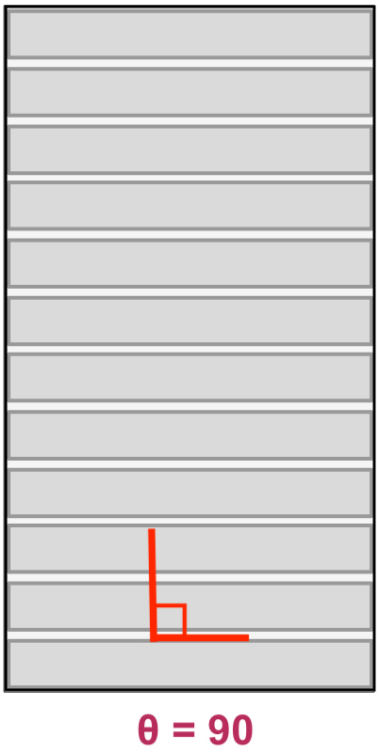

(d) 90° raster angle.

Figure 4.4: Illustrations of symmetric stack sequence $[\theta/\text{-}\theta]_{4s}$ for different raster angles.

4.3 Results and Discussion

A Matlab code[1] has been developed to calculate the equivalent longitudinal elastic modulus ($E_{1_{equivalent}}$) of EBAM sample with stack sequence $[\theta/\text{-}\theta]_{4s}$. The code is written according to the procedure described step by step in Algorithm 1. The results of the CLPT model are then compared with the experimental results from the samples printed with different raster angles (θ = 0°, 30°, 60°, 90°). Note that in this thesis, EBAM samples with raster angle θ are printed with symmetric stack sequence $[\theta/\text{-}\theta]_{4s}$ according to Equation (4.34) as shown in Equation (4.34).

4.3.1 Sensitivity Analysis of CLPT Results with Respect to Poisson's Ratio

In order to use Algorithm 1, it is required to set the materials Poisson's ratio (ν) as one of the inputs. To assess the sensitivity of the results with respect to ν, different values of ν ranged from $\nu_{min} = 0.3$ to $\nu_{max} = 0.5$ have been examined, as presented in this section. The minimum and maximum feasible values are chosen based on the reported Poisson's ratio of polymers given in [104].

The $E_{1_{equivalent}}$ results obtained from CLPT model for ν between $\nu_{min} = 0.3$ to $\nu_{max} = 0.5$ for different raster angle ranged from 0° to 90° are shown in Figures 4.5 and 4.7, respectively for 85% and 100% infill. Note that results for $0.3 \leq \nu \leq 0.5$ lies in between the blue curve and the red curve in Figures 4.5 and 4.7, hence not shown in these figures for better visibility of the plots.

It can be seen in Figures 4.5 and 4.7 that variation of the results with respect to ν is not significant. To further illustrate this, Figures 4.6 and 4.8 show the percentage difference between results for $\nu = 0.3$ and $\nu = 0.5$. Maximum difference is 1.663% and 0.036%, respectively for 85% and 100% infill percentage. The 1.663% and 0.036% differences signifies that Poisson's ratio does not have a significant impact on the predicted elastic modulus of CLPT model. Hence, using $\nu = 0.42$ in assumption

[1]The code is presented in Appendix B.

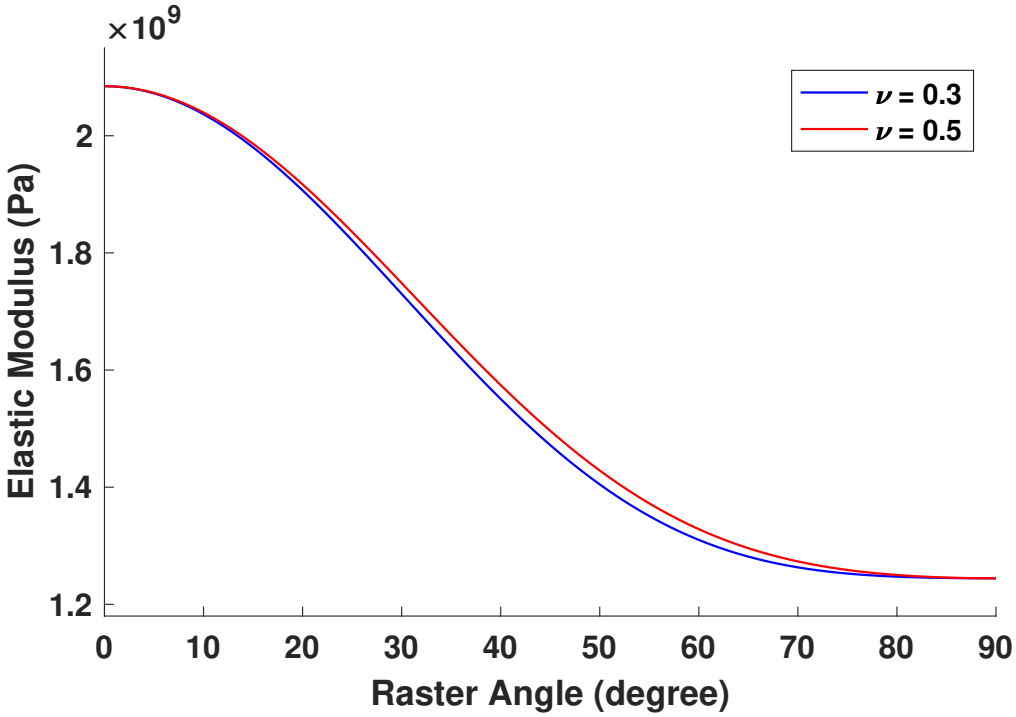

Figure 4.5: Calculated longitudinal elastic modulus $E_{1_{equivalent}}$ for different raster angles for $\nu = 0.3$ and $\nu = 0.5$ for 85% infill.

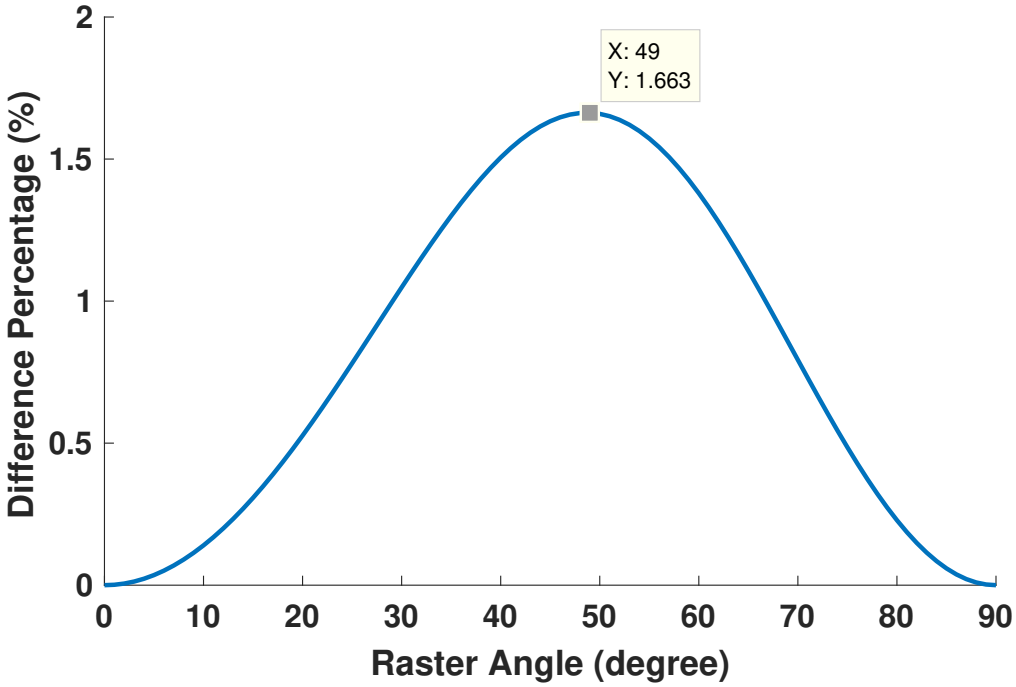

Figure 4.6: Percentage Difference between $E_{1_{equivalent}}$ results of $\nu = 0.3$ and $\nu = 0.5$ for different raster angles for 85% infill.

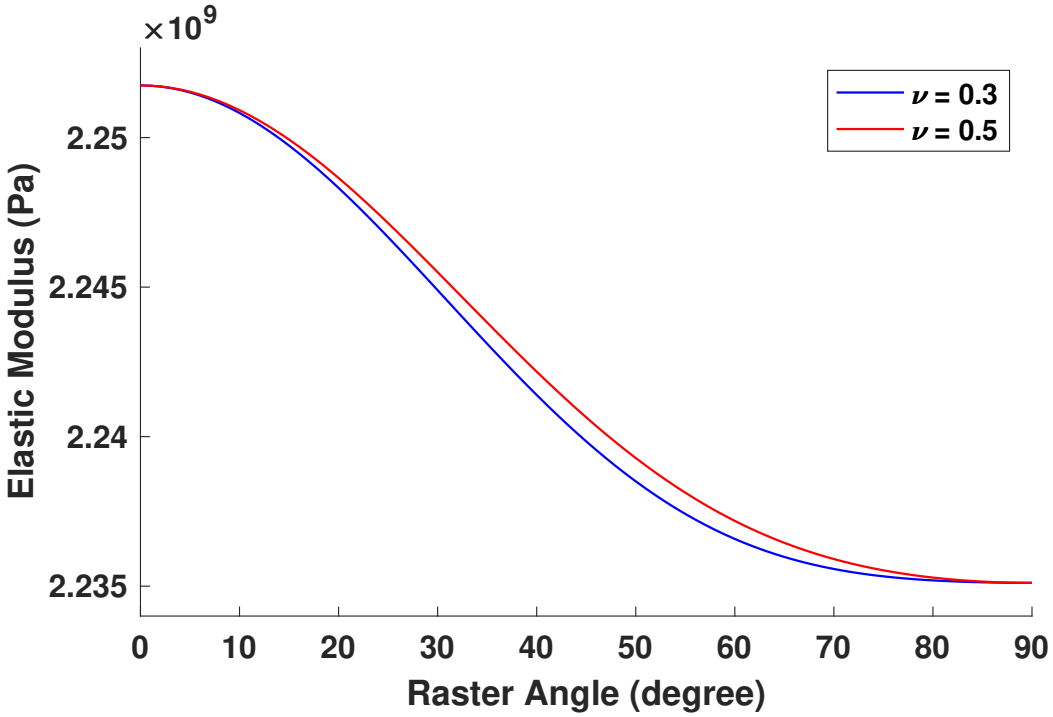

Figure 4.7: Calculated longitudinal elastic modulus $E_{1_{equivalent}}$ for different raster angles for $\nu = 0.3$ and $\nu = 0.5$ for 100% infill.

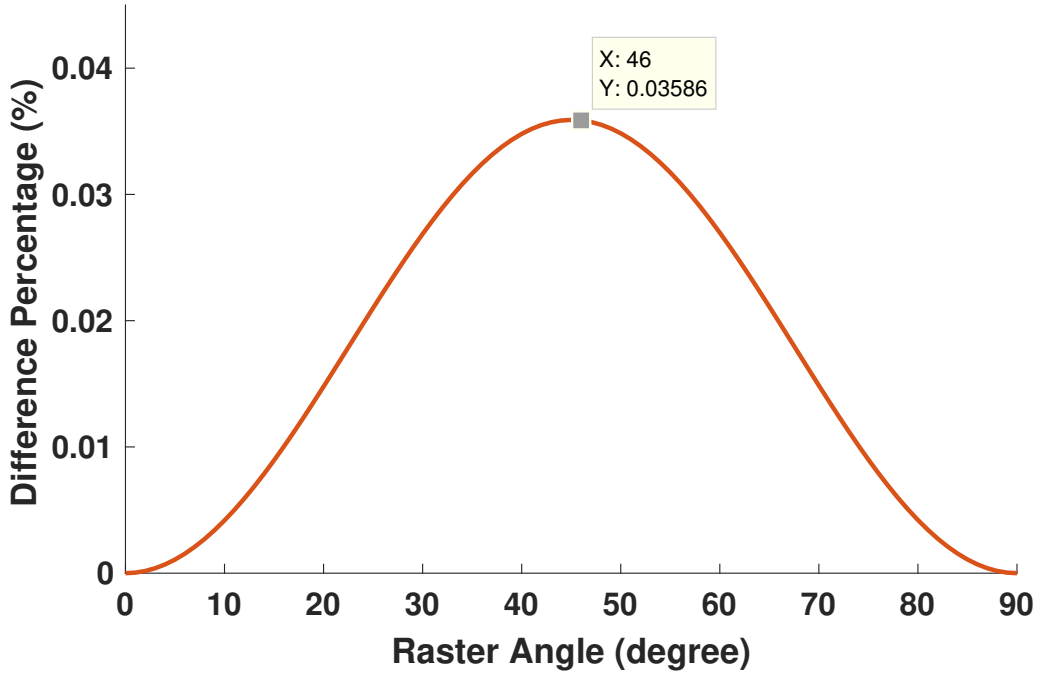

Figure 4.8: Percentage Difference between $E_{1_{equivalent}}$ results of $\nu = 0.3$ and $\nu = 0.5$ for different raster angles for 100% infill.

(A5), which is the Poisson's ratio of pure polyurethane [102, 103], is a reasonable assumption.

4.3.2 Comparision of the CLPT Model and Experimental Results

The experimental results obtained from 30° and 60° raster angle samples (see Chapter 3 for more details) as well as CLPT predicted results for different raster angles are shown in Figures 4.9 and 4.10 for 85% and 100% infill, respectively.

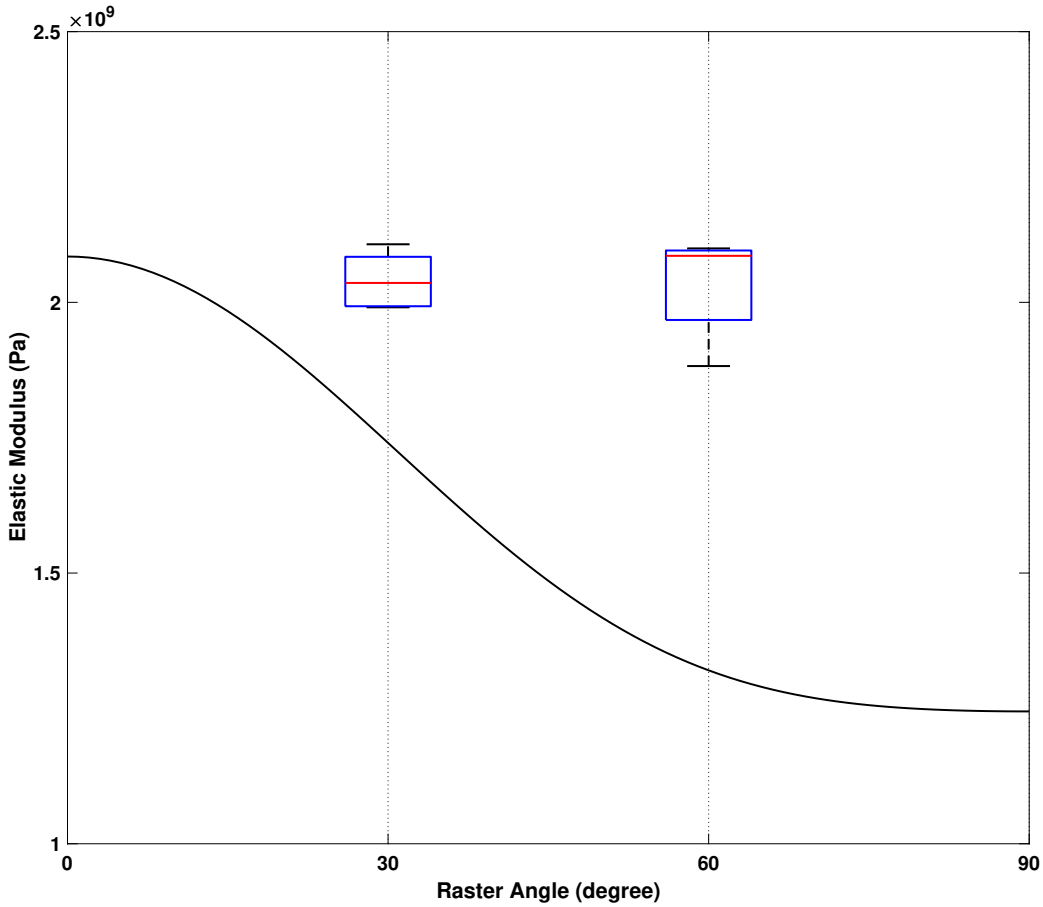

Figure 4.9: CLPT results (solid black curve) vs expermental results (box plot) for 85% samples.

In Figures 4.9 and 4.10 black solid curve represents the results of CLPT model for different raster angles. The box plots show the experimental results including: the minimum, first quartile, median (second quartile), third quartile and maximum

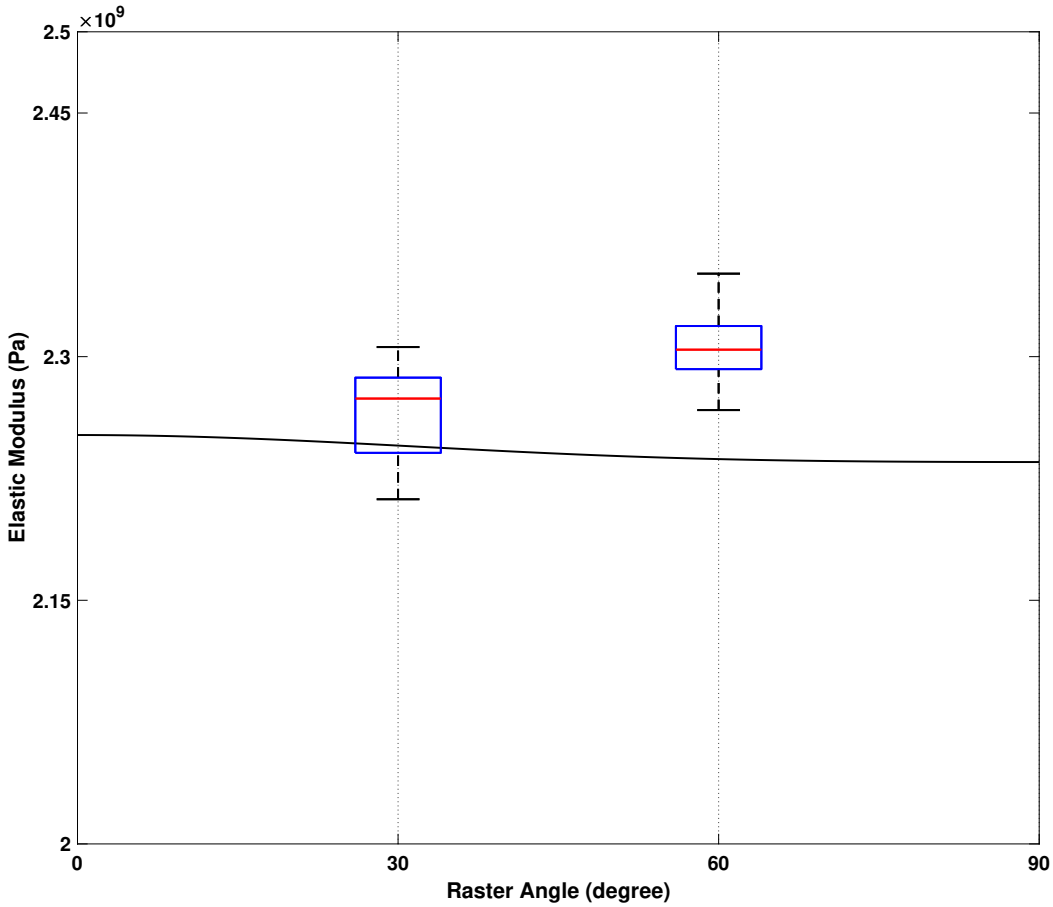

Figure 4.10: CLPT results vs experimental results for 100% samples.

values obtained from 30° and 60° raster angle samples.

Figure 4.10 shows 0.86% and 3.01% difference between CLPT and experimental results for 30° and 60° raster angle in 100% infill. As a comparison, Casavola et al. [12], reported the difference between experimental and CLPT results to be 1.07% for ABS and 5.37% for PLA samples with 100% infill. Note that in [12], [30/-30/0/-30/30] stack sequence and 0.35 mm layer thickness were used.

As illustrated in Figure 4.9, the difference between CLPT and experimental results is higher for 85% infill samples. This is mainly due to the fact that the air gap is much larger at 85% infill level compared to 100% infill. Having large air gap increase the amount of material that can penetrate into the air gap from the upper layer. Thus, at 85% criss-cross raster patterns such as 30° and 60° raster angles show much

higher elastic modulus compared to the value predicted in CLPT as the reinforcement provided by criss-cross raster patterns are not concidered in CLPT predictions.

The difference between experimental results and CLPT prediction is 14.72% and 35.01% for 30° and 60° raster angle samples in 85% infill. Unfortunately, in the work of Casavola et al [12] no data is reported for other infill percentages. Hence, results in [12] are not comparable here.

While CLPT results have a small difference with experimental results in 100% infill samples, CLPT predictions do not show a perfect agreement with the test results for 85% sample results. Hence, in order to use CLPT predictions for EBAM parts, some necessary adjustments are needed in CLPT model based on the experimental results and the nature of EBAM process.

4.3.3 Modification of CLPT Model

This first adjustment is mainly due to the difference between the nature of EBAM production and laminated composites which CLPT is designed for. In laminated composite, the production of each lamina is independent from the neighboring laminae. Therefore, the mechanical properties of each lamina is independent of the rest of the laminate [43]. On the contrary, in EBAM process each layer act as a mold for the next layer [2]. In other words, in EBAM process each layer is produced by deposition of the fused material on top of the last layer. As a natural consequence of this process, it is possible for the fused extruded material to partially penetrate into the underneath layer air gaps. The chance of penetration increases when the raster angle differs between the base layer and the top layer, particularly if these layers are perpendicular to each other. This effect can serve as a reinforcement for the base layer leading to improvement of mechanical behaviour of the weak phase. This is mainly due to the nature of EBAM process. The melting temperature of MM4520 is 158.5°C [29]. In order to provide a suitable viscosity for the material during the EBAM deposition process, filaments are heated to 225°C (more than 65°C above the

melting temperature). However, in most of the commercial EBAM materials such as ABS or PLA, material is heated around 20°C-30°C above the melting point temperature [104]. This higher temperature than the material melting point used for EBAM of MM4520, makes it more probable for the fused extruded material to penetrate into the air gaps during EBAM process. Additionally, the thickness of each layer is chosen to be 0.1 mm in this study, which is considerably lower compared to similar studies [50, 85–88]. For example Casavola et al [12] uses 0.35 mm as layer thickness. The lower layer thickness of 0.1 mm results in EBAM parts with much higher resolution, which also increases the probability of penetrations of layers and hence increases the reinforcement of the weak phase.

In order to take the reinforcement effect into account in the CLPT model, a compensation term is introduced for the material properties of weak phase (E_w, G_w) as described in the following section.

Weak phase compensation in CLPT model: Based on assumption (A2), the mechanical properties of weak phase (E_w, G_w) are smaller than the extruded beads (E_b, G_b), i.e. $E_w < E_b$ and $G_w < G_b$. However, because of the aforementioned reinforcement phenomenon, a mechanism is needed to increase the E_w (possibly up to E_b). This motivates the introduction of a compensation function $\Psi_E(\cdot)$ that modifies E_w to E_w^{mod} as follows:

$$E_w^{mod} = E_w + \Psi_E(\Delta\theta) \tag{4.35}$$

$$\Psi_E(\Delta\theta) = (E_b - E_w) * \Phi(\Delta\theta) * \lambda \tag{4.36}$$

where $\Phi(\Delta\theta)$ and λ are both scaling factors ranged from zero to one ($0 \leq \Phi(\Delta\theta) \leq 1$, $0 \leq \lambda \leq 1$). When both $\Phi(\Delta\theta) = 1$ and $\lambda = 1$, from Equations (4.35) and (4.36) it follows that $E_w^{mod} = E_b$. Similarly, when $\Phi(\Delta\theta) = 0$ or $\lambda = 0$, then $E_w^{mod} = E_w$ and properties of weak phase are not modified.

λ is a coefficient that conceptually represents the reinforcement effect of perpen-

dicular plies. In other words, $\lambda = 0$ when deposition of a perpendicular layer causes no reinforcement on the adjacent ply beneath it. Also $\lambda = 1$ corresponds to the case where deposition of a perpendicular layer fully reinforces the weak phase of beneath layer and hence $E_w^{mod} = E_b$. In general, the value of λ depends on a variety of fabrication conditions, such as printing temperature, layer thickness, material properties, etc. Due to the complexity of λ, it is later obtained empirically from the experimental results.

$\Phi(\Delta\theta)$ represents the influence of stack sequence and is a function of $\Delta\theta$ given by:

$$\Phi(\Delta\theta) = 1 - \left(\frac{90-|\Delta\theta|}{90}\right)^2 \tag{4.37}$$

$$\Delta\theta = \theta_{k+1} - \theta_k \tag{4.38}$$

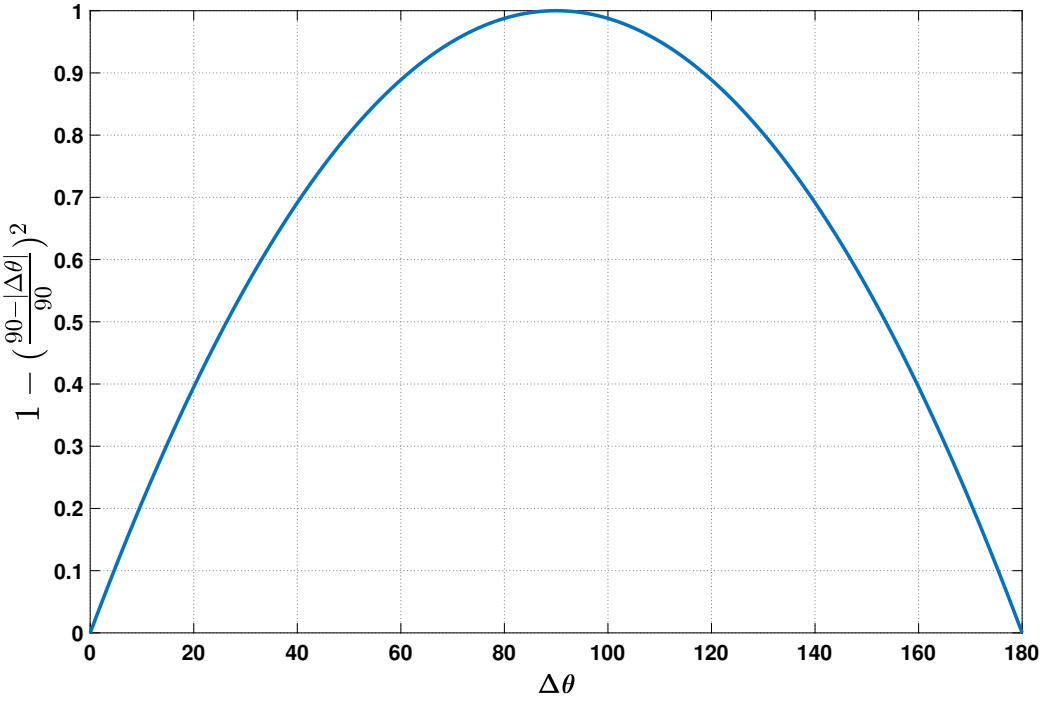

Figure 4.11: Illustration of compensation function $\Phi(\Delta\theta)$ for different $\Delta\theta$.

where $\Delta\theta$ is the difference between the raster angle of k-th layer and its adjacent layer as shown in Equation (4.38). As shown in Figure 4.11, the function $\Phi(\Delta\theta)$ is

designed in such a way that it is maximum ($\Phi = 1$) when $\Delta\theta$=90° or in other words adjacent layers are perpendicular to the each other. On the contrary, $\Phi = 0$ when $\Delta\theta$ is equal to 0° or 180° which means that adjacent layers are parallel to each other.

Following assumption (A4), similar compensation function $\Psi_G(\cdot)$ is defined to modify G_w to G_w^{mod} from:

$$G_w^{mod} = G_w + \Psi_G(\Delta\theta) \tag{4.39}$$

$$\Psi_{G_w}(\Delta\theta) = (G_b - G_w) * \Phi(\Delta\theta) * \lambda \tag{4.40}$$

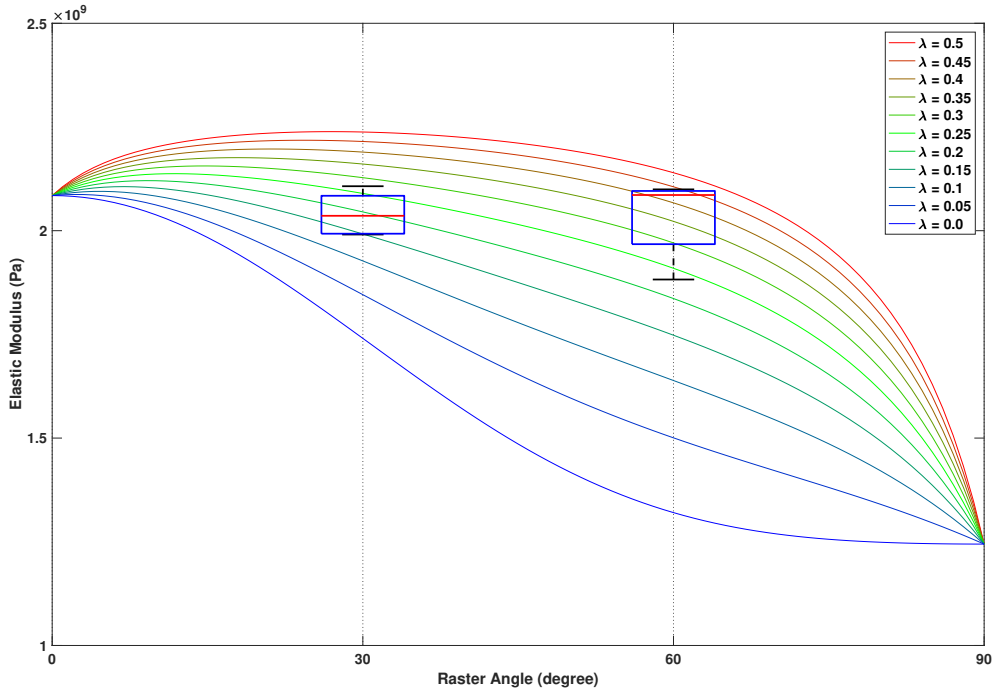

Figure 4.12: The influence of different λ values ranged from 0 to 0.5 on CLPT prediction results vs. experimental results for 85% infill samples.

Figures 4.12 and 4.13 show the impact of aforementioned compensation factors on predictions, using different λ values for 85% and 100% infill samples, respectively. In these charts, experimental results for 30° and 60° are shown with the box plot.

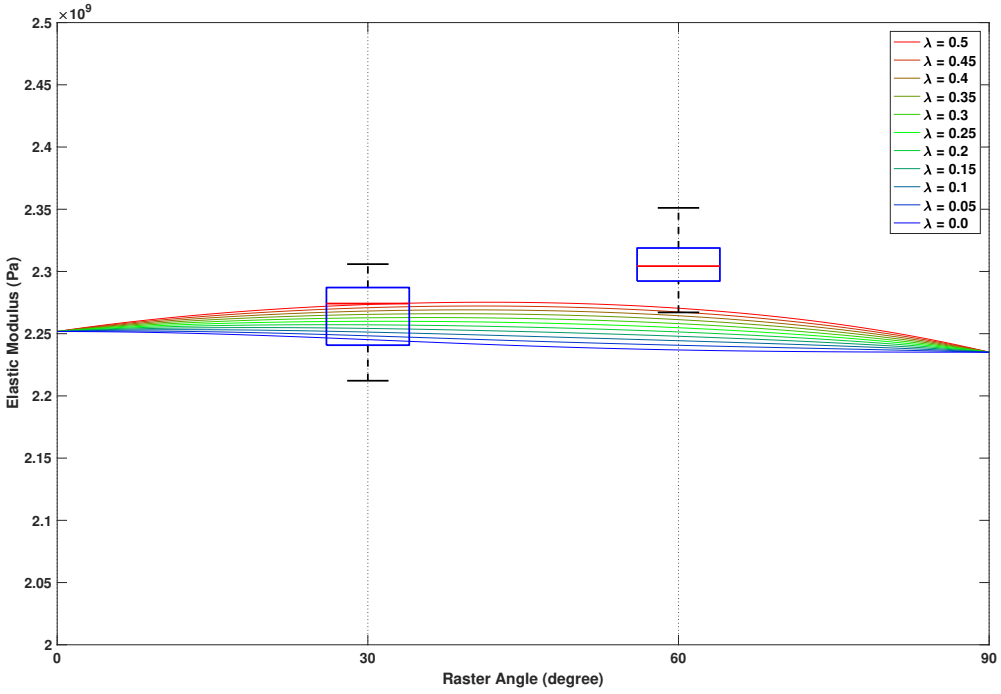

Figure 4.13: The influence of different λ values ranged from 0 to 0.5 on CLPT prediction results vs. experimental results for 100% infill samples.

Poisson's ratio compensation for CLPT model: In assumption (A5) the major Poisson's ratio of a single printed layer (ν_{12}) is assumed to be same as material's Poisson's ratio (ν). However, in reality the major Poisson's ratio of a single ply might be bigger than the one of material due to the empty spaces between individual filaments [2]. This is the motivation to introduce a compensation parameter to modify the major Poisson's ratio of a single ply as follows:

$$\nu_{12}^{mod} = \nu + \Delta\nu \tag{4.41}$$

where $\Delta\nu$ is the compensation parameter.

Figures 4.14 and 4.15 show the CLPT predictions of elastic modulus using different $\Delta\nu$ values vs. the experimental results for 85% and 100% infill samples, respectively.

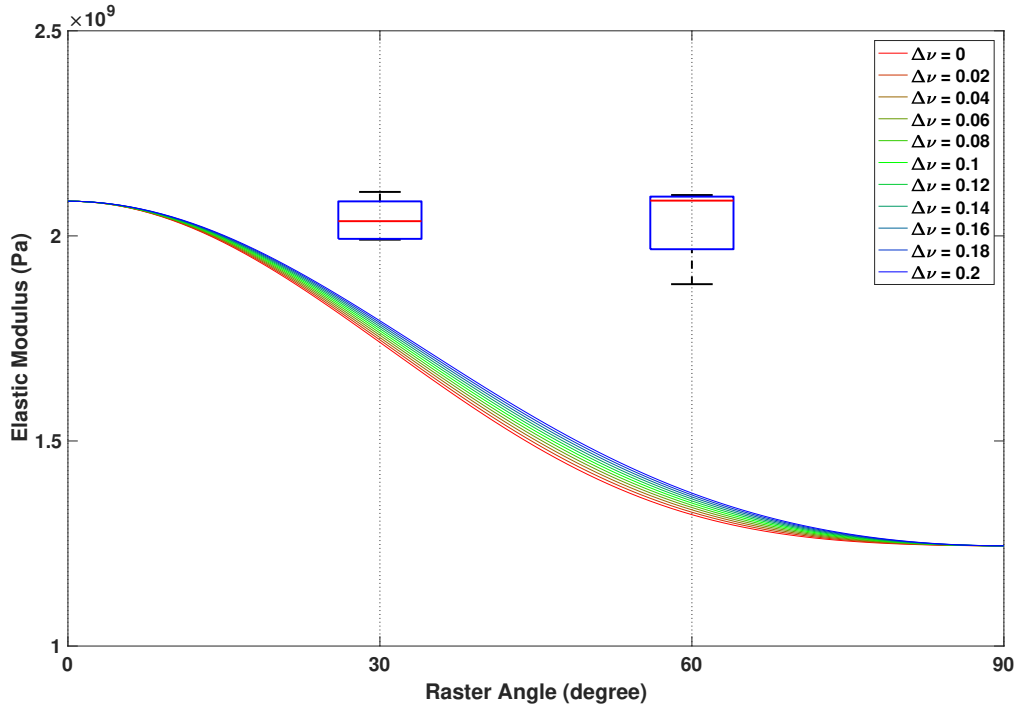

Figure 4.14: The influence of different $\Delta\nu$ values ranged from 0 to 0.2 on CLPT prediction results vs. experimental results for 85% infill samples.

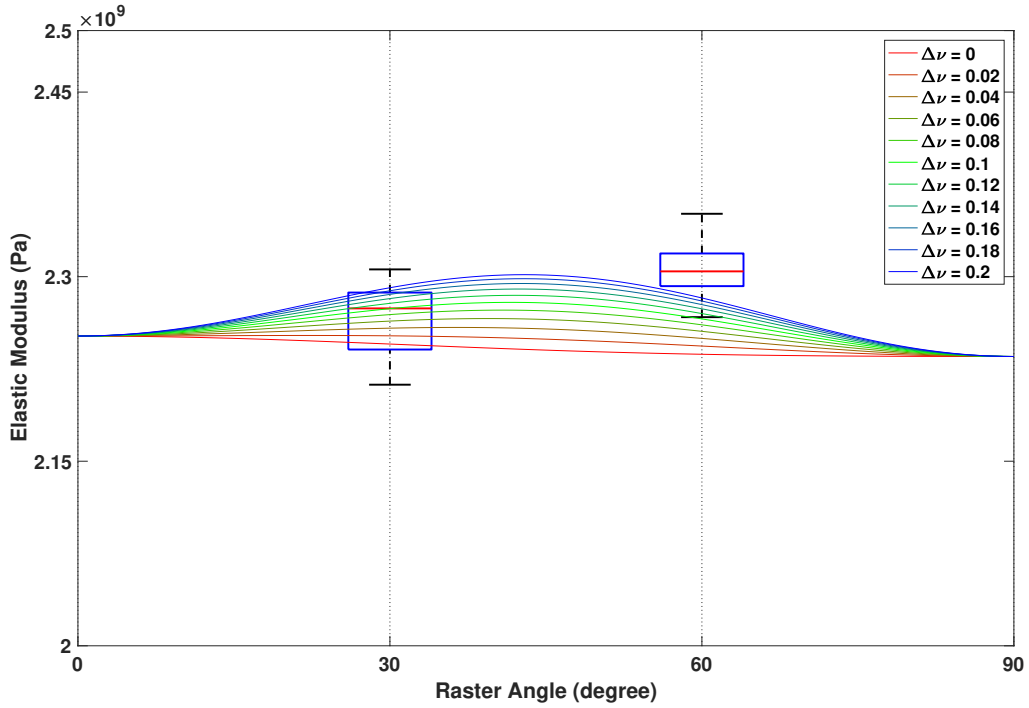

Figure 4.15: The influence of different $\Delta\nu$ values ranged from 0 to 0.2 on CLPT prediction results vs. experimental results for 100% infill samples.

Error calculations using compensation factors: With compensation functions in Equations (4.36), (4.40) and (4.41), it is necessary to find a modification to CLPT model that better matches all experimental results. Note that modified-CLPT results is dependant on the choice of λ and $\Delta\nu$. Since experimental results for samples with raster angles 30° and 60° for both 85% and 100% infill samples are available, we compute the modified E_{CLPT} at different $\Delta\nu$ and λ with raster angles 30° and 60° for both 85% and 100% infill. Then, for a given λ and $\Delta\nu$ the total error is calculated as the difference between the modified-CLPT results and experimental results as follows:

$$\%\, error(\lambda, \Delta\nu) = \sqrt{e_1^2 + e_2^2 + e_3^2 + e_4^2} \times 100 \tag{4.42}$$

where,

$$e_1 = \frac{E_{expt}(85\%,30°) - E_{CLPT}(85\%,30°,\lambda,\Delta\nu)}{E_{expt}(85\%,30°)}$$

$$e_2 = \frac{E_{expt}(85\%,60°) - E_{CLPT}(85\%,60°,\lambda,\Delta\nu)}{E_{expt}(85\%,60°)}$$

$$e_3 = \frac{E_{expt}(100\%,30°) - E_{CLPT}(100\%,30°,\lambda,\Delta\nu)}{E_{expt}(100\%,30°)}$$

$$e_4 = \frac{E_{expt}(100\%,60°) - E_{CLPT}(100\%,60°,\lambda,\Delta\nu)}{E_{expt}(100\%,60°)}$$

Figure 4.16 shows the error % for different λ and $\Delta\nu$ values. For better visualization, projection of the errors into λ-$\Delta\nu$ plane is also shown in Figure 4.17. The minimum value of error % among different λ and $\Delta\nu$ values is chosen as the best empirical values for λ and $\Delta\nu$. From Figures 4.16 and 4.17 it is concluded that the combination of $\lambda = 0.36$ and $\Delta\nu = 0.027$ results in minimum error of 5.96%.

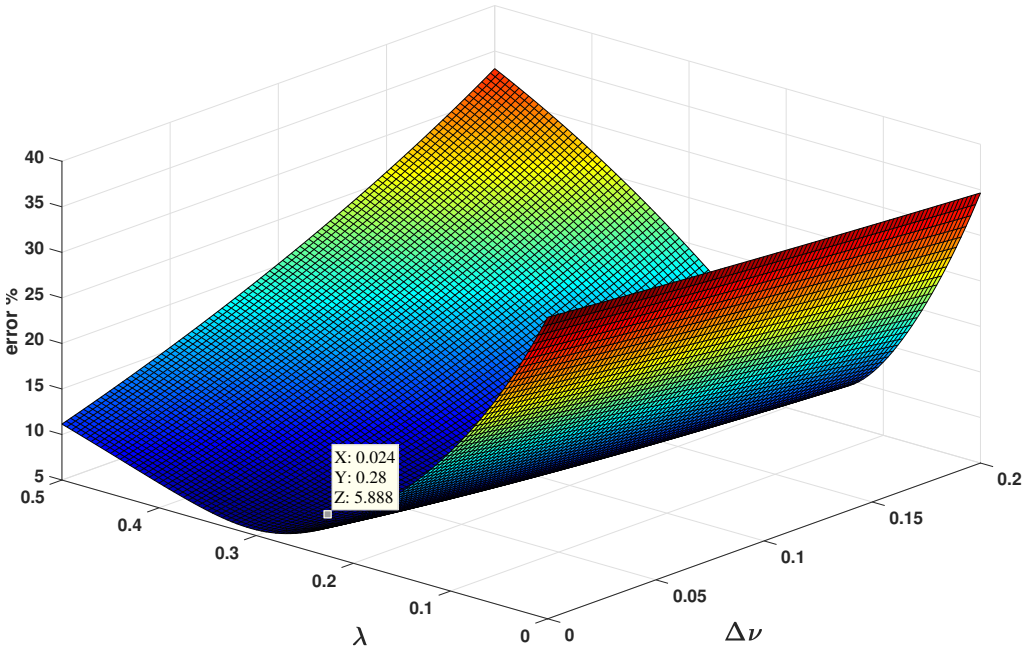

Figure 4.16: Illustration of error for different $\Delta\nu$ compensation and different λ.

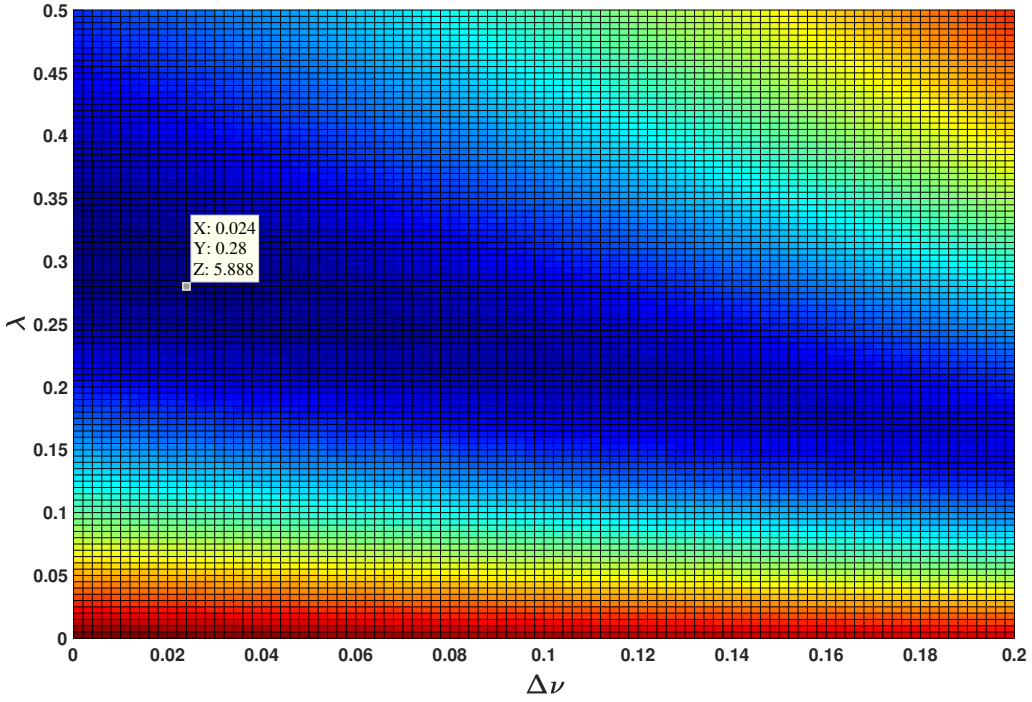

Figure 4.17: Projection of the errors on λ-$\Delta\nu$ plane. The minimum error of 5.89% is found to be at $\lambda = 0.28$ and $\Delta\nu = 0.024$.

Prediction of EBAM samples elastic modulus with modified CLPT model

Having empirical values of λ and $\Delta\nu$, the modified weak phase E_w^{mod}, E_w^{mod} and ν_{12}^{mod} are used in Algorithm 1 and the results of modified CLPT model are shown in Figures 4.18 and 4.19 for 85% and 100% infill samples, respectively.

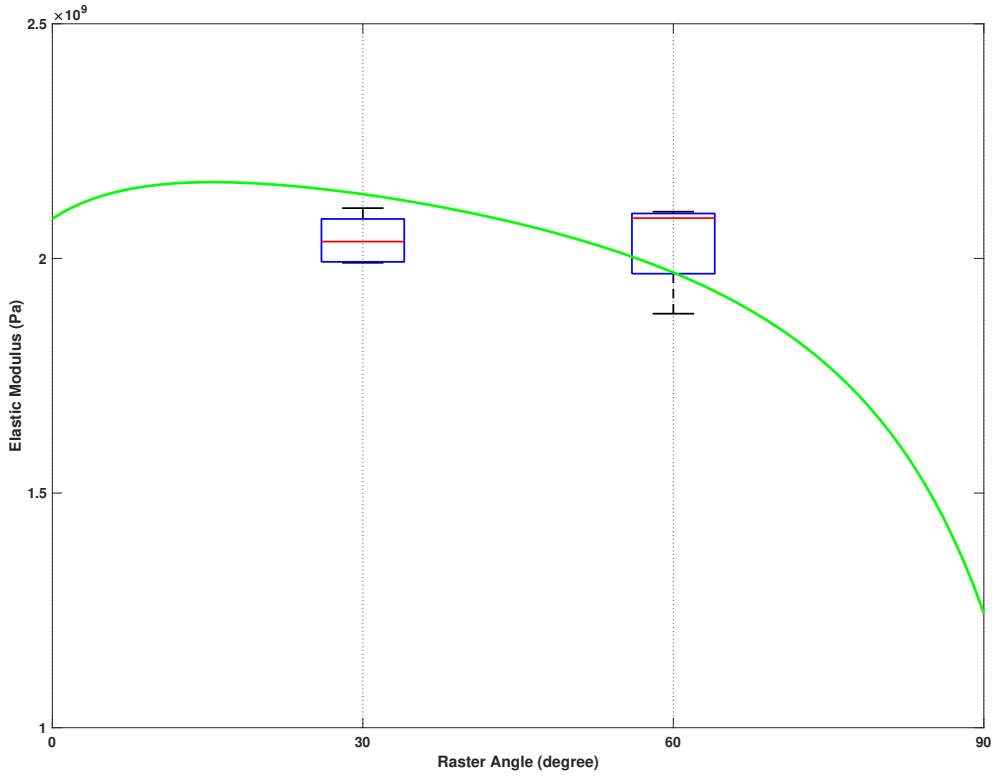

Figure 4.18: Comparison of prediction of modified-CLPT model ($E_{1_{equivalent}}$) vs experimental results of EBAM samples with 85% infill.

Figures 4.18 and 4.19 demonstrate a significant improvement in the accuracy of the predictions compared to Figures 4.9 and 4.10. The error between experimental and predicted results is presented in Table 4.4 for different infill percentages and raster angles. Note that, Figures 4.18 and 4.19 do not represent a usual CLPT curve. Instead, these curves are generated from the modified model based on CLPT to better fit the EBAM sample behaviour.

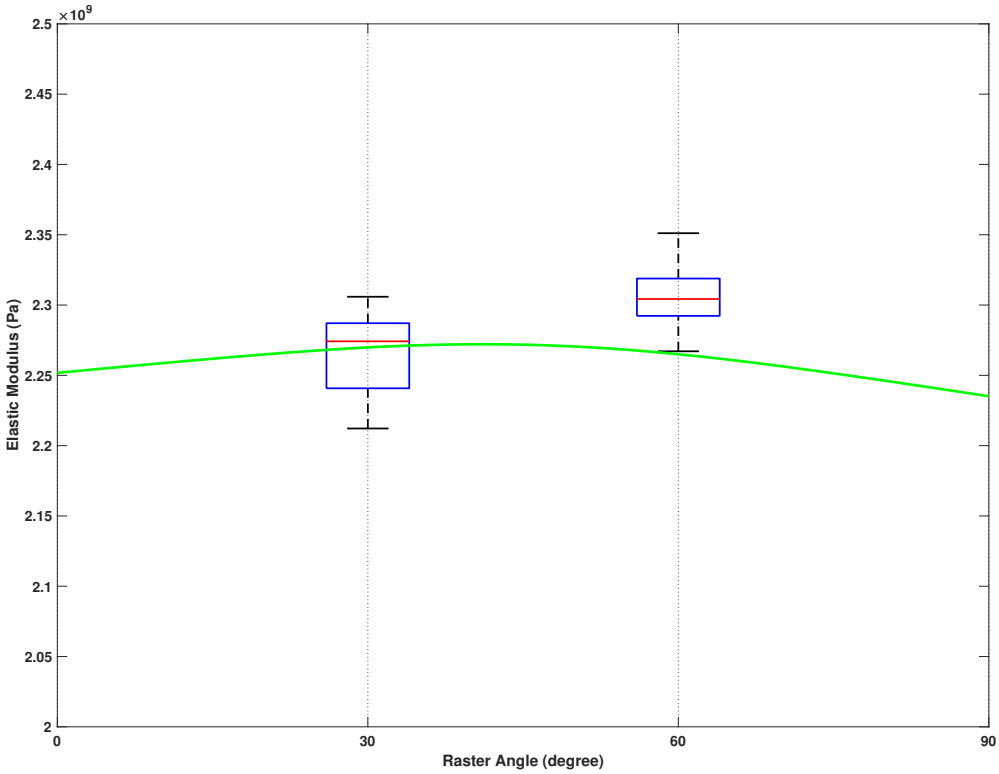

Figure 4.19: Comparison of prediction of modified-CLPT model ($E_{1_{equivalent}}$) vs experimental results of EBAM samples with 100% infill.

Table 4.4: The improvement in difference percentage between experimental and predicted results.

infill %	raster angle	error before adjustments	error after adjustments
85%	30°	14.72%	4.71%
85%	60°	35.01%	3.04%
100%	30°	1.07%	0.23%
100%	60°	5.37%	1.79%

Although predictions of the modified-CLPT model show a satisfactory agreement with the experimental results, there is still a minimal error between experimental and predicted results. The possible sources of this error are listed as follows:

- **Residual stress:** EBAM manufacturing is associated with heating/melting followed by rapid cooling/solidifying cycles which lead to non-uniform thermal residual stresses and strains in the created parts. Residual stresses caused by the EBAM process are controlled by selected printing parameters. Raster angle is among the most important printing parameters which have a significant influence on the stress build-up in the final sample [105]. Such residual stresses are not considered in CLPT model.

- **Average mechanical properties:** The macro-mechanical analysis of a lamina in CLPT is based on the assumption that lamina is homogeneous [106]. However, this assumption does not perfectly match with a layer created by EBAM technique.

- **Ignoring thickness stress components:** CLPT is developed under the plane-stress condition in which the stress components in the thickness direction are ignored in this theory. This condition is only applicable for thin plates with significantly small thickness compared to their width [107]. Although in this study, thickness of each layer is 0.1 mm which is considerably smaller than that in similar studies [50, 85–88], still the aspect ratio of cross-section of the samples for the tensile test is about 0.5 (thickness= $16 \times 0.1 = 1.6$ mm and width=3.18 mm). Hence, assuming plane-stress condition might be another source of error. This is due to the fact that 0.5 aspect ratio is not small enough for plain-stress condition.

4.4 Conclusions

In this chapter, a general algorithm is presented based on CLPT to predict elastic modulus of the EBAM parts. This algorithm requires elastic modulus of EBAM produced samples with 0° and 90° raster angle as the input. The longitudinal elastic modulus of the sample for any stack sequence is obtained as the output of the algorithm. The accuracy of the algorithm is investigated using the experimental results obtained from EBAM of MM4520 shape memory polymer. In order to do so, the average elastic modulus of the samples with 30° and 60° raster angles is compared with the predicted values from the algorithm for both 85% and 100% infill. Despite having small differences for 100% infill samples, the predicted values does not show a satisfactory agreement with the experimental results. Hence, two different compensation terms are introduced to modify the CLPT model. With these modifications, the difference between experimental and predicted values decreased significantly to a minimal range of 0.25% to 4.47%. Other models present in literature report the difference between analytical model and experimental results as 4.7% to 6.6% [81] and 1.07% to 5.37% [12]. In summary, for MM4520 shape memory polymer, it is suggested to use CLPT-based Algorithm 1 with the adjustments mentioned in Equations (4.35), (4.39) and (4.41) with $\lambda = 0.36$ and $\Delta\nu = 0.027$.

Chapter 5

Conclusions, Recommendations and Future Work

5.1 Conclusions and Recommendations

In this thesis, the influence of infill percentage and raster angle on mechanical properties of MM4520 shape memory polymer, produced by extrusion-based additive manufacturing (EBAM) was investigated. One hundred and twenty samples in four different raster angles (0°, 30°, 60° and 90°) and three different infill percentage levels (85%, 100% and 115%) were produced and tested. From the tensile test measurements, elastic modulus (E), yield strength (σ_y), maximum elongation percentage ($EL\%$), modulus of resilience (U_r) and tensile toughness (U_T) were determined.

According to the tensile test results, no significant variation in elastic modulus (E) of different raster angles is observed except for 85% infill samples with 90° raster angle which show about 35% decrease in elastic modulus compared to other raster angles of the same infill. Moreover, increasing infill percentage from 85% to 100% causes a significant increase in elastic modulus.

Similarly, yield strength of 100% and 115% infill samples is not significantly influenced by the raster angle. However, at 85% infill level, increasing the raster angle leads to a clear drop in the yield strength. Hence, variation in yield strength with respect to the infill percentage is heavily dependent on the raster angle. Moreover, modulus of resilience (U_r) shows nearly identical trends to yield strength (σ_y).

Unlike elastic modulus, yield strength and resilience (E, σ_y, U_r), raster angle causes dramatic variation in maximum elongation ($EL\%$) and tensile toughness (U_T) at any infill percentage level. However, the impact of raster angle magnifies with the reduction of infill percentage. Also 100% infill samples are superior compared to 85% and 115% infill samples, in terms of deformability and tensile toughness except at 90° raster angle.

Hence, for unidirectional loading systems , 100% infill and 0° or 30° raster angle is suggested for the applications which requires high plastic deformation. However, if the principal requirement for the product is the stiffness of the part, 115% infill and 0° raster angle is suggested. It should be emphasized that, in conditions that lateral loading is also involved, criss-cross raster patterns such as 30° or 60° are preferable over 0° in both 85% and 100% infill levels. That is due the higher mechanical properties of criss-cross raster patterns considering the average between longitudinal and lateral direction.

In addition to the experimental findings, a generic algorithm is presented based on CLPT theory to predict elastic modulus of the EBAM parts. This algorithm requires elastic modulus of EBAM produced samples with 0° and 90° raster angle as the input. The equivalent longitudinal elastic modulus of the sample for any stack sequence is obtained as the output of the algorithm. Furthermore, the accuracy of the algorithm is compared with the experimental results at 85% and 100% infill level. Despite having small differences for 100% infill samples, the predicted values did not show a satisfactory agreement with the experimental results. Hence, two different compensation terms are introduced to modify the CLPT model according to the EBAM process principals. With these modifications, the difference between experimental and predicted values decreased significantly to a minimal range of 0.25% to 4.47%. Additional studies needs to be done in order to validate the model and the modifications used in this thesis to validate the usability of the model under different conditions.

5.2 Contributions

The main contributions of this work are as follows:

Experimental Investigation: The influence of raster angle and infill percentage on SMP samples is investigated experimentally in this thesis.

- The reliability of experimental results is improved compared to previous studies by removing outer shell of the samples.
- Unlike previous studies, one infill percentage level above 100% is also investigated. This provides a reference point to EBAM samples with the maximum density (no air gap) that can be achieved with EBAM.
- Compared to previous studies, additional mechanical properties including yield strength and tensile toughness are included.

Analytical Investigation: In this work, CLPT is used for SMP samples in order to predict the elastic modulus for different raster angles and stack sequences. Compared to previous studies:

- CLPT model predictions are reported for all raster angles in two different infill percentages. Moreover, predictions are compared with experimental results in 4 different combinations of raster angle and infill percentage. (Note that in the previous studies only one infill percentage and raster angle was compared with the predictions.)
- The CLPT model is modified using two compensation factors in order to achieve more accurate predictions for EBAM samples.
- Based on the modified CLPT, a specific model is provided that characterizes the elastic modulus of SMP parts for any raster angle and any stack sequence.

5.3 Future Work

This thesis provides important experimental (Chapter 3) and analytical (Chapter 4) foundations on which further research can be built on.

First of all, customization of mechanical properties of EBAM samples with infill percentage and raster angle can be further investigated with respect to other key slicing parameters, such as layer thickness and stack sequence. An experimental setup that investigates the effect of layer thickness and stack sequence on mechanical properties of EBAM parts is highly desirable. Additionally, other mechanical properties such as impact toughness can be analyzed. This would provide a comprehensive understanding of mechanical behaviour of SMP parts produced by EBAM under different loading scenarios.

Another promising future direction is the investigation of effect of printing/nozzle temperature on the SMP end-parts. This could provide a temperature guideline for printing MM4520 in different applications.

Regarding analytical modeling of EBAM, more investigation is needed in to validate the analytical model presented in this thesis. Also, this thesis is the first study that introduced adjustments on CLPT to better fit the EBAM results. Hence it can serve as a foundation for future additional modifications in order to achieve a general model to predict mechanical properties of EBAM parts with respect to the raster angle. Also, Similar analytical analysis can be done in future studies to predict the mechanical behaviour of EBAM parts with respect to the infill percentage or porosity volume.

Bibliography

[1] O. A. Mohamed, S. H. Masood, and J. L. Bhowmik, "Optimization of fused deposition modeling process parameters: A review of current research and future prospects," *Advances in Manufacturing*, vol. 3, no. 1, pp. 42–53, 2015.

[2] D. Popescu, A. Zapciu, C. Amza, F. Baciu, and R. Marinescu, "FDM process parameters influence over the mechanical properties of polymer specimens: A review," *Polymer Testing*, vol. 69, pp. 157 –166, 2018.

[3] J. Kietzmann, L. Pitt, and P. Berthon, "Disruptions, decisions, and destinations: Enter the age of 3D printing and additive manufacturing," *Business Horizons*, vol. 58, no. 2, pp. 209–215, 2015.

[4] J. Y. Wong and A. C. Pfahnl, "3D printing of surgical instruments for long-duration space missions," *Aviation, Space, and Environmental Medicine*, vol. 85, no. 7, pp. 758–763, 2014.

[5] A. Kreemer and Z. H. Moe, "Rapid manufacturing using FDM systems," *Handbook of Manufacturing Engineering and Technology*, pp. 1–11, 2013.

[6] X. Kuang, K. Chen, C. K. Dunn, J. Wu, V. C. F. Li, and H. J. Qi, "3D printing of highly stretchable, shape-memory, and self-healing elastomer toward novel 4d printing," *ACS Applied Materials & Interfaces*, vol. 10, no. 8, pp. 7381–7388, 2018.

[7] Q. Meng and J. Hu, "A review of shape memory polymer composites and blends," *Composites Part A: Applied Science and Manufacturing*, vol. 40, no. 11, pp. 1661–1672, 2009.

[8] H. Meng and G. Li, "A review of stimuli-responsive shape memory polymer composites," *Polymer*, vol. 54, no. 9, pp. 2199–2221, 2013.

[9] M. Zarek, M. Layani, I. Cooperstein, E. Sachyani, D. Cohn, and S. Magdassi, "3D printing of shape memory polymers for flexible electronic devices," *Advanced Materials*, vol. 28, no. 22, pp. 4449–4454, 2015.

[10] C.-S. Zhang and Q.-Q. Ni, "Bending behavior of shape memory polymer based laminates," *Composite Structures*, vol. 78, no. 2, pp. 153–161, 2007.

[11] J. Villacres, D. Nobes, and C. Ayranci, "Additive manufacturing of shape memory polymers: Effects of print orientation and infill percentage on mechanical properties," *Rapid Prototyping Journal*, R. I. Campbell and D. Bourell, Eds., pp. 00–00, 2018.

[12] C. Casavola, A. Cazzato, V. Moramarco, and C. Pappalettere, "Orthotropic mechanical properties of fused deposition modelling parts described by classical laminate theory," *Materials & Design*, vol. 90, pp. 453–458, 2016.

[13] Reprinted from Publication title, D. Popescu, A. Zapciu, C. Amza, F. Baciu, and R. Marinescu, "FDM process parameters influence over the mechanical properties of polymer specimens: A review," Polymer Testing, vol. 69, pp. 157–166, 2018, with permission from Elsevier.

[14] *Ultimaker Cura: Advanced 3D printing software, made accessible — ultimaker*. [Online]. Available: `https://ultimaker.com/en/products/ultimaker-cura-software`.

[15] *3D printing software - Simplify3D*. [Online]. Available: `https://www.simplify3d.com/`.

[16] *Slic3r - g-code generator for 3D printers*. [Online]. Available: `https://slic3r.org/`.

[17] L. Vernon and H. Vernon, "Producing molded articles such as dentures from thermoplastic synthetic resins," *US Pat*, vol. 2234993, 1941.

[18] K. Otsuka and C. M. Wayman, *Shape memory materials*. Cambridge university press, 1999.

[19] A. Lendlein and S. Kelch, "Shape-memory polymers," *Angewandte Chemie International Edition*, vol. 41, no. 12, pp. 2034–2057, 2002.

[20] Z. Wei, R Sandstroröm, and S Miyazaki, "Shape-memory materials and hybrid composites for smart systems: Part i shape-memory materials," *Journal of Materials Science*, vol. 33, no. 15, pp. 3743–3762, 1998.

[21] J. Leng, X. Lan, Y. Liu, and S. Du, "Shape-memory polymers and their composites: Stimulus methods and applications," *Progress in Materials Science*, vol. 56, no. 7, pp. 1077 –1135, 2011, ISSN: 0079-6425. DOI: `https://doi.org/10.1016/j.pmatsci.2011.03.001`. [Online]. Available: `http://www.sciencedirect.com/science/article/pii/S0079642511000429`.

[22] J. Guo, Z. Wang, L. Tong, H. Lv, and W. Liang, "Shape memory and thermomechanical properties of shape memory polymer/carbon fiber composites," *Composites Part A: Applied Science and Manufacturing*, vol. 76, pp. 162–171, 2015.

[23] C Liu, H Qin, and P. Mather, "Review of progress in shape-memory polymers," *Journal of materials chemistry*, vol. 17, no. 16, pp. 1543–1558, 2007.

[24] Z. X. Khoo, J. E. M. Teoh, Y. Liu, C. K. Chua, S. Yang, J. An, K. F. Leong, and W. Y. Yeong, "3D printing of smart materials: A review on recent progresses in 4d printing," *Virtual and Physical Prototyping*, vol. 10, no. 3, pp. 103–122, 2015.

[25] S. Tibbits, "The emergence of "4d printing"," in *TED conference*, 2013.

[26] C.-S. Zhang and Q.-Q. Ni, "Bending behavior of shape memory polymer based laminates," *Composite Structures*, vol. 78, no. 2, pp. 153–161, 2007.

[27] X. Ma, "Bending of a polyurethane based shape memory polymer: modeling and experiment," Master's thesis, University of Alberta, 2018.

[28] W. M. Huang, B. Yang, and Y. Q. Fu, *Polyurethane shape memory polymers*. CRC Press, 2011.

[29] J. F. Villacres, "Additive manufacturing of shape memory polymers : Effects of print orientation and infill percentage on mechanical and shape memory recovery properties," Master's thesis, University of Alberta, 2017.

[30] P. E. Anuta, "Spatial registration of multispectral and multitemporal digital imagery using fast fourier transform techniques," *IEEE transactions on Geoscience Electronics*, vol. 8, no. 4, pp. 353–368, 1970.

[31] T. J. Keating, P. Wolf, and F. Scarpace, "An improved method of digital image correlation," *Photogrammetric Engineering and Remote Sensing*, vol. 41, no. 8, pp. 993–1002, 1975.

[32] W. Peters and W. Ranson, "Digital imaging techniques in experimental stress analysis," *Optical engineering*, vol. 21, no. 3, p. 213 427, 1982.

[33] T. Chu, W. Ranson, and M. A. Sutton, "Applications of digital-image-correlation techniques to experimental mechanics," *Experimental mechanics*, vol. 25, no. 3, pp. 232–244, 1985.

[34] H. Bruck, S. McNeill, M. A. Sutton, and W. Peters, "Digital image correlation using newton-raphson method of partial differential correction," *Experimental mechanics*, vol. 29, no. 3, pp. 261–267, 1989.

[35] H. Schreier, J.-J. Orteu, and M. A. Sutton, *Image correlation for shape, motion and deformation measurements*. Springer US, 2009.

[36] B. Pan, K. Qian, H. Xie, and A. Asundi, "Two-dimensional digital image correlation for in-plane displacement and strain measurement: A review," *Measurement Science and Technology*, vol. 20, no. 6, p. 062 001, 2009.

[37] P.-C. Hung and A. Voloshin, "In-plane strain measurement by digital image correlation," *Journal of the Brazilian Society of Mechanical Sciences and Engineering*, vol. 25, no. 3, pp. 215–221, 2003.

[38] B. Pan, H. Xie, Z. Wang, K. Qian, and Z. Wang, "Study on subset size selection in digital image correlation for speckle patterns," *Optics express*, vol. 16, no. 10, pp. 7037–7048, 2008.

[39] T. Chu, W. Ranson, and M. A. Sutton, "Applications of digital-image-correlation techniques to experimental mechanics," *Experimental mechanics*, vol. 25, no. 3, pp. 232–244, 1985.

[40] D. Turner, P. Crozier, and P. Reu, *Digital image correlation engine, version 00*, 2015.

[41] H.-T. Thai and S.-E. Kim, "A review of theories for the modeling and analysis of functionally graded plates and shells," *Composite Structures*, vol. 128, pp. 70–86, 2015.

[42] M. Shokrieh and S. K. Shahri, "Modeling residual stresses in composite materials," in *Residual Stresses in Composite Materials*, Elsevier, 2014, pp. 173–193.

[43] J. N. Reddy, *Mechanics of Laminated Composite Plates, Theory and Analysis*. Boca Raton: CRC Press, 1997.

[44] A. K. Kaw, *Mechanics of composite materials*. CRC press, 2005.

[45] N. G. Tanikella, B. Wittbrodt, and J. M. Pearce, "Tensile strength of commercial polymer materials for fused filament fabrication 3D printing," *Additive Manufacturing*, vol. 15, pp. 40–47, 2017.

[46] B. Tymrak, M. Kreiger, and J. Pearce, "Mechanical properties of components fabricated with open-source 3-d printers under realistic environmental conditions," *Materials & Design*, vol. 58, pp. 242–246, 2014.

[47] A Bagsik and V Schöppner, "Mechanical properties of fused deposition modeling parts manufactured with ultem," *DMRC. Germany*, 2011.

[48] S.-H. Ahn, M. Montero, D. Odell, S. Roundy, and P. K. Wright, "Anisotropic material properties of fused deposition modeling abs," *Rapid prototyping journal*, vol. 8, no. 4, pp. 248–257, 2002.

[49] I. Durgun and R. Ertan, "Experimental investigation of fdm process for improvement of mechanical properties and production cost," *Rapid Prototyping Journal*, vol. 20, no. 3, pp. 228–235, 2014.

[50] A. K. Sood, R. K. Ohdar, and S. S. Mahapatra, "Parametric appraisal of mechanical property of fused deposition modelling processed parts," *Materials & Design*, vol. 31, no. 1, pp. 287–295, 2010.

[51] H. Li, T. Wang, and Z. Yu, "The quantitative research of interaction between key parameters and the effects on mechanical property in fdm," *Advances in Materials Science and Engineering*, vol. 2017, 2017.

[52] W. Wu, P. Geng, G. Li, D. Zhao, H. Zhang, and J. Zhao, "Influence of layer thickness and raster angle on the mechanical properties of 3D-printed peek and a comparative mechanical study between peek and abs," *Materials*, vol. 8, no. 9, pp. 5834–5846, 2015.

[53] J. T. Cantrell, S. Rohde, D. Damiani, R. Gurnani, L. DiSandro, J. Anton, A. Young, A. Jerez, D. Steinbach, C. Kroese, *et al.*, "Experimental characterization of the mechanical properties of 3D-printed abs and polycarbonate parts," *Rapid Prototyping Journal*, vol. 23, no. 4, pp. 811–824, 2017.

[54] S. H. Masood, K. Mau, and W. Song, "Tensile properties of processed fdm polycarbonate material," in *Materials Science Forum*, Trans Tech Publ, vol. 654, 2010, pp. 2556–2559.

[55] J. F. Rodríguez, J. P. Thomas, and J. E. Renaud, "Mechanical behavior of acrylonitrile butadiene styrene (abs) fused deposition materials. experimental investigation," *Rapid Prototyping Journal*, vol. 7, no. 3, pp. 148–158, 2001.

[56] Q Sun, G. Rizvi, C. Bellehumeur, and P Gu, "Effect of processing conditions on the bonding quality of fdm polymer filaments," *Rapid Prototyping Journal*, vol. 14, no. 2, pp. 72–80, 2008.

[57] S. Xiaoyong, C. Liangcheng, M. Honglin, G. Peng, B. Zhanwei, and L. Cheng, "Experimental analysis of high temperature peek materials on 3D printing test," in *Measuring Technology and Mechatronics Automation (ICMTMA), 2017 9th International Conference on*, IEEE, 2017, pp. 13–16.

[58] L. Baich, G. Manogharan, and H. Marie, "Study of infill print design on production cost-time of 3D printed abs parts," *International Journal of Rapid Manufacturing*, vol. 5, no. 3-4, pp. 308–319, 2015.

[59] G. C. Onwubolu and F. Rayegani, "Characterization and optimization of mechanical properties of abs parts manufactured by the fused deposition modelling process," *International Journal of Manufacturing Engineering*, vol. 2014, 2014.

[60] J. Torres, M. Cole, A. Owji, Z. DeMastry, and A. P. Gordon, "An approach for mechanical property optimization of fused deposition modeling with polylactic acid via design of experiments," *Rapid Prototyping Journal*, vol. 22, no. 2, pp. 387–404, 2016.

[61] J. Chacón, M. Caminero, E. García-Plaza, and P. Núñez, "Additive manufacturing of pla structures using fused deposition modelling: Effect of process parameters on mechanical properties and their optimal selection," *Materials & Design*, vol. 124, pp. 143–157, 2017.

[62] H. Li, T. Wang, J. Sun, and Z. Yu, "The effect of process parameters in fused deposition modelling on bonding degree and mechanical properties," *Rapid Prototyping Journal*, vol. 24, no. 1, pp. 80–92, 2018.

[63] R Hernandez, D Slaughter, D Whaley, J Tate, and B Asiabanpour, "Analyzing the tensile, compressive, and flexural properties of 3D printed abs p430 plastic based on printing orientation using fused deposition modeling," in *27th Annual International Solid Freeform Fabrication Symposium, Austin, TX*, 2016, pp. 939–950.

[64] S. Ziemian, M. Okwara, and C. W. Ziemian, "Tensile and fatigue behavior of layered acrylonitrile butadiene styrene," *Rapid Prototyping Journal*, vol. 21, no. 3, pp. 270–278, 2015.

[65] A. Fatimatuzahraa, B Farahaina, and W. Yusoff, "The effect of employing different raster orientations on the mechanical properties and microstructure of fused deposition modeling parts," in *Business, Engineering and Industrial Applications (ISBEIA), 2011 IEEE Symposium on*, IEEE, 2011, pp. 22–27.

[66] X. Liu, M. Zhang, S. Li, L. Si, J. Peng, and Y. Hu, "Mechanical property parametric appraisal of fused deposition modeling parts based on the gray taguchi method," *The International Journal of Advanced Manufacturing Technology*, vol. 89, no. 5-8, pp. 2387–2397, 2016.

[67] O. Es-Said, J Foyos, R Noorani, M. Mendelson, R Marloth, and B. Pregger, "Effect of layer orientation on mechanical properties of rapid prototyped samples," *Materials and Manufacturing Processes*, vol. 15, no. 1, pp. 107–122, 2000.

[68] C Alvarez, L Kenny, C Lagos, F Rodrigo, and M. Aizpun, "Investigating the influence of infill percentage on the mechanical properties of fused deposition modelled abs parts," *Ingeniería e Investigación*, vol. 36, no. 3, pp. 110–116, 2016.

[69] D. Croccolo, M. De Agostinis, and G. Olmi, "Experimental characterization and analytical modelling of the mechanical behaviour of fused deposition processed parts made of abs-m30," *Computational Materials Science*, vol. 79, pp. 506–518, 2013.

[70] S. Mahmood, A. Qureshi, K. L. Goh, and D. Talamona, "Tensile strength of partially filled fff printed parts: Experimental results," *Rapid Prototyping Journal*, vol. 23, no. 1, pp. 122–128, 2017.

[71] M. S. Hossain, J. Ramos, D. Espalin, M. Perez, and R. Wicker, "Improving tensile mechanical properties of FDM-manufactured specimens via modifying build parameters," in *International Solid Freeform Fabrication Symposium: An Additive Manufacturing Conference. Austin, TX*, vol. 2013, 2013, pp. 380–392.

[72] M Bertoldi, M. Yardimci, C. Pistor, S. Guceri, and G. Sala, "Mechanical characterization of parts processed via fused deposition," *Solid Freeform Fabrication Proceedings, Austin, TX*, pp. 557–565, 1998.

[73] A. K. Sood, R. K. Ohdar, and S. S. Mahapatra, "Experimental investigation and empirical modelling of FDM process for compressive strength improvement," *Journal of Advanced Research*, vol. 3, no. 1, pp. 81–90, 2012.

[74] K. P. Motaparti, "Effect of build parameters on mechanical properties of ultem 9085 parts by fused deposition modeling," 2016.

[75] M. Domingo-Espin, J. M. Puigoriol-Forcada, A.-A. Garcia-Granada, J. Lluma, S. Borros, and G. Reyes, "Mechanical property characterization and simulation of fused deposition modeling polycarbonate parts," *Materials & Design*, vol. 83, pp. 670–677, 2015.

[76] F Knoop, V Schoeppner, F. Knoop, and V Schoeppner, "Mechanical and thermal properties of FDM parts manufactured with polyamide 12," in *Proceedings of the 26th Annual International Solid Freeform Fabrication Symposium—An Additive Manufacturing Conference, Austin, TX, USA*, 2015, pp. 10–12.

[77] B. Rankouhi, S. Javadpour, F. Delfanian, and T. Letcher, "Failure analysis and mechanical characterization of 3D printed abs with respect to layer thickness and orientation," *Journal of Failure Analysis and Prevention*, vol. 16, no. 3, pp. 467–481, 2016.

[78] T. Letcher, B. Rankouhi, and S. Javadpour, "Experimental study of mechanical properties of additively manufactured abs plastic as a function of layer parameters," in *ASME 2015 International Mechanical Engineering Congress and Exposition*, American Society of Mechanical Engineers, 2015, V02AT02A018–V02AT02A018.

[79] J. Raasch, M. Ivey, D. Aldrich, D. S. Nobes, and C. Ayranci, "Characterization of polyurethane shape memory polymer processed by material extrusion additive manufacturing," *Additive Manufacturing*, vol. 8, pp. 132–141, 2015.

[80] Y. Yang, Y. Chen, Y. Wei, and Y. Li, "3D printing of shape memory polymer for functional part fabrication," *The International Journal of Advanced Manufacturing Technology*, vol. 84, no. 9-12, pp. 2079–2095, 2015.

[81] D. Croccolo, M. D. Agostinis, and G. Olmi, "Experimental characterization and analytical modelling of the mechanical behaviour of fused deposition processed parts made of ABS-m30," *Computational Materials Science*, vol. 79, pp. 506–518, 2013.

[82] T. Lv, Z. Cheng, E. Zhang, H. Kang, Y. Liu, and L. Jiang, "Self-restoration of superhydrophobicity on shape memory polymer arrays with both crushed microstructure and damaged surface chemistry," *Small*, vol. 13, no. 4, p. 1 503 402, 2016.

[83] Y. Y. C. Choong, S. Maleksaeedi, H. Eng, J. Wei, and P.-C. Su, "4d printing of high performance shape memory polymer using stereolithography," *Materials & Design*, vol. 126, pp. 219–225, 2017.

[84] Z. X. Khoo, J. E. M. Teoh, Y. Liu, C. K. Chua, S. Yang, J. An, K. F. Leong, and W. Y. Yeong, "3D printing of smart materials: A review on recent progresses in 4d printing," *Virtual and Physical Prototyping*, vol. 10, no. 3, pp. 103–122, 2015.

[85] J. F. Rodríguez, J. P. Thomas, and J. E. Renaud, "Mechanical behavior of acrylonitrile butadiene styrene (ABS) fused deposition materials. experimental investigation," *Rapid Prototyping Journal*, vol. 7, no. 3, pp. 148–158, 2001.

[86] S.-H. Ahn, M. Montero, D. Odell, S. Roundy, and P. K. Wright, "Anisotropic material properties of fused deposition modeling ABS," *Rapid Prototyping Journal*, vol. 8, no. 4, pp. 248–257, 2002.

[87] B. Lee, J. Abdullah, and Z. Khan, "Optimization of rapid prototyping parameters for production of flexible ABS object," *Journal of Materials Processing Technology*, vol. 169, no. 1, pp. 54–61, 2005.

[88] Q. Sun, G. Rizvi, C. Bellehumeur, and P. Gu, "Effect of processing conditions on the bonding quality of FDM polymer filaments," *Rapid Prototyping Journal*, vol. 14, no. 2, pp. 72–80, 2008.

[89] A. K. Sood, R. K. Ohdar, and S. S. Mahapatra, "Experimental investigation and empirical modelling of FDM process for compressive strength improvement," *Journal of Advanced Research*, vol. 3, no. 1, pp. 81–90, 2012.

[90] *Ultimaker 3 specification sheet*, `https://ultimaker.com/en/products/ultimaker-3`, Accessed: 2018-11-19.

[91] "Representation of surface roughness in fused deposition modeling," *Journal of Materials Processing Technology*, vol. 209, no. 15, pp. 5593 –5600, 2009.

[92] A. International, *ASTM D638-14, Standard Test Method for Tensile Properties of Plastics*. ASTM International, 2015.

[93] C. Ziemian, M. Sharma, and S. Ziemian, "Anisotropic mechanical properties of abs parts fabricated by fused deposition modelling," in *Mechanical engineering*, InTech, 2012.

[94] H. Li, T. Wang, and Z. Yu, "The quantitative research of interaction between key parameters and the effects on mechanical property in FDM," *Advances in Materials Science and Engineering*, vol. 2017, pp. 1–15, 2017.

[95] Y.-L. Huang and N. Brown, "Dependence of slow crack growth in polyethylene on butyl branch density: Morphology and theory," *Journal of Polymer Science Part B: Polymer Physics*, vol. 29, no. 1, pp. 129–137, 1991.

[96] D. Roylance, "Stress-strain curves," *Massachusetts Institute of Technology study, Cambridge*, 2001.

[97] B. Caulfield, P. McHugh, and S. Lohfeld, "Dependence of mechanical properties of polyamide components on build parameters in the sls process," *Journal of Materials Processing Technology*, vol. 182, no. 1, pp. 477 –488, 2007.

[98] M. K. Thompson, G. Moroni, T. Vaneker, G. Fadel, R. I. Campbell, I. Gibson, A. Bernard, J. Schulz, P. Graf, B. Ahuja, and F. Martina, "Design for additive manufacturing: Trends, opportunities, considerations, and constraints," *CIRP Annals*, vol. 65, no. 2, pp. 737 –760, 2016.

[99] S.-H. Ahn, M. Montero, D. Odell, S. Roundy, and P. K. Wright, "Anisotropic material properties of fused deposition modeling ABS," *Rapid Prototyping Journal*, vol. 8, no. 4, pp. 248–257, 2002.

[100] G. Kirchhoff, "Über das gleichgewicht und die bewegung einer elastischen scheibe.," *Journal für die reine und angewandte Mathematik (Crelles Journal)*, vol. 1850, no. 40, pp. 51–88, 1850.

[101] A. Bellini and S. Güçeri, "Mechanical characterization of parts fabricated using fused deposition modeling," *Rapid Prototyping Journal*, vol. 9, no. 4, pp. 252–264, 2003.

[102] J. H. Collier, J. P. Camp, T. W. Hudson, and C. E. Schmidt, "Synthesis and characterization of polypyrrole–hyaluronic acid composite biomaterials for tissue engineering applications," *Journal of Biomedical Materials Research*, vol. 50, no. 4, pp. 574–584,

[103] T. Rivers, T. Hudson, and C. Schmidt, "Synthesis of a novel, biodegradable electrically conducting polymer for biomedical applications," *Advanced Functional Materials*, vol. 12, no. 1, pp. 33–37,

[104] J. Bicerano, *Prediction of Polymer Properties*. CRC Press, 2002.

[105] "Fiber bragg grating based investigation of residual strains in abs parts fabricated by fused deposition modeling process," *Materials & Design*, vol. 50, pp. 44 –50, 2013.

[106] W. Yung-Ming and T. Jiann-Quo, "A three-dimensional analysis of anisotropic inhomogeneous and laminated plates," *International Journal of Solids and Structures*, vol. 31, no. 4, pp. 497 –515, 1994, ISSN: 0020-7683.

[107] J. N. Reddy, "A generalization of two-dimensional theories of laminated composite plates," *Communications in Applied Numerical Methods*, vol. 3, no. 3, pp. 173–180,

Appendix A: Representative Stress-Strain Curves of Each Raster Angle and Infill Percentage

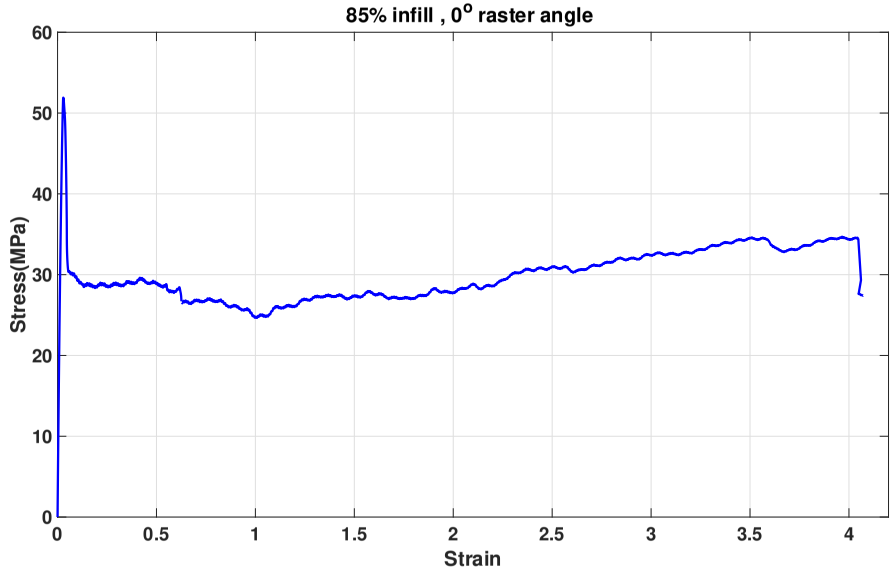

(a) 85% infill and 0° raster angle.

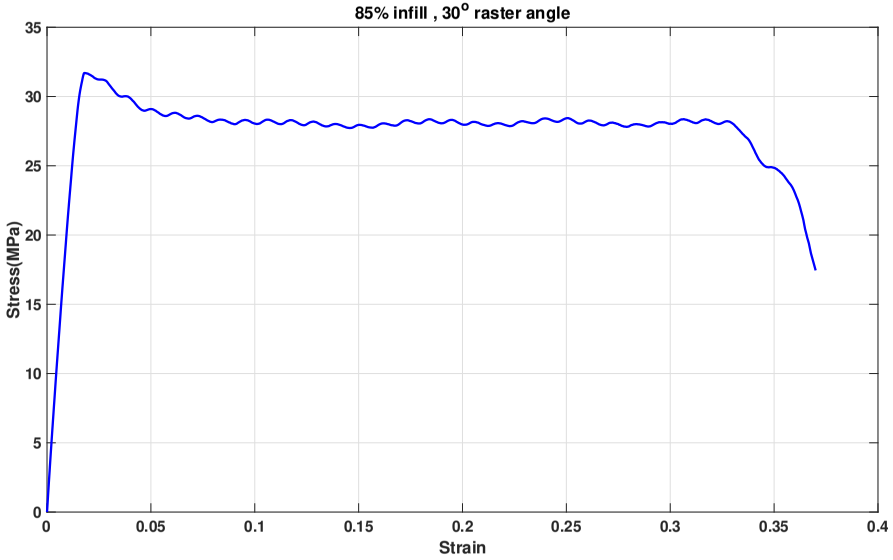

(b) 85% infill and 30° raster angle.

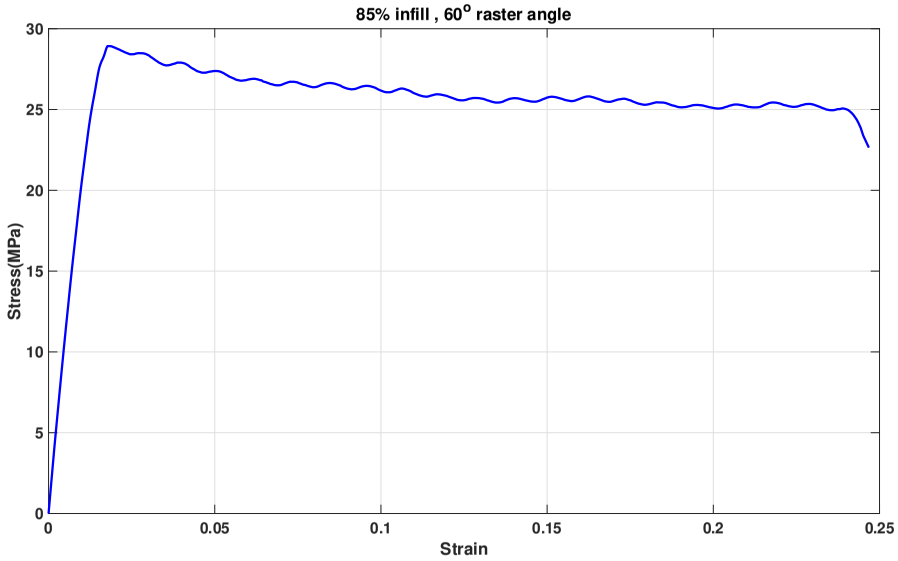

(c) 85% infill and 60° raster angle.

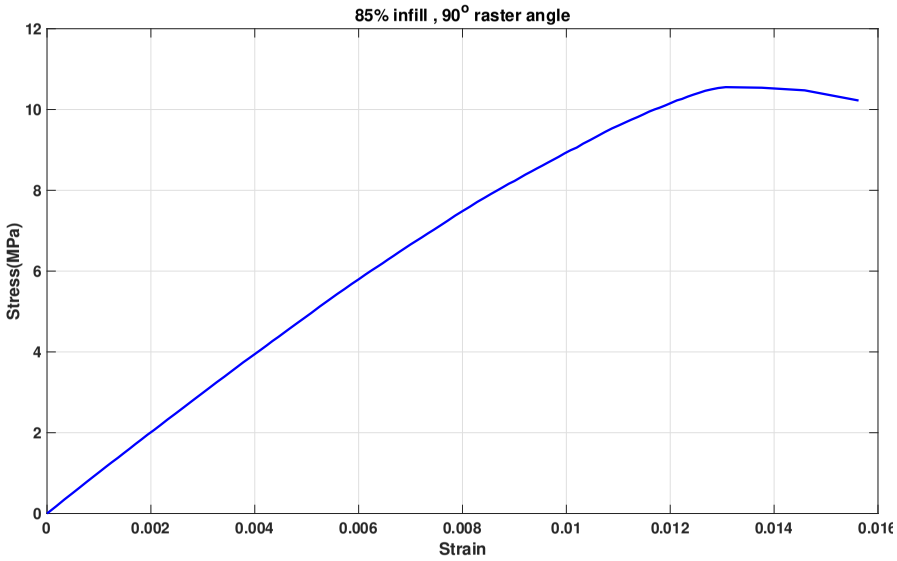

(d) 85% infill and 90° raster angle.

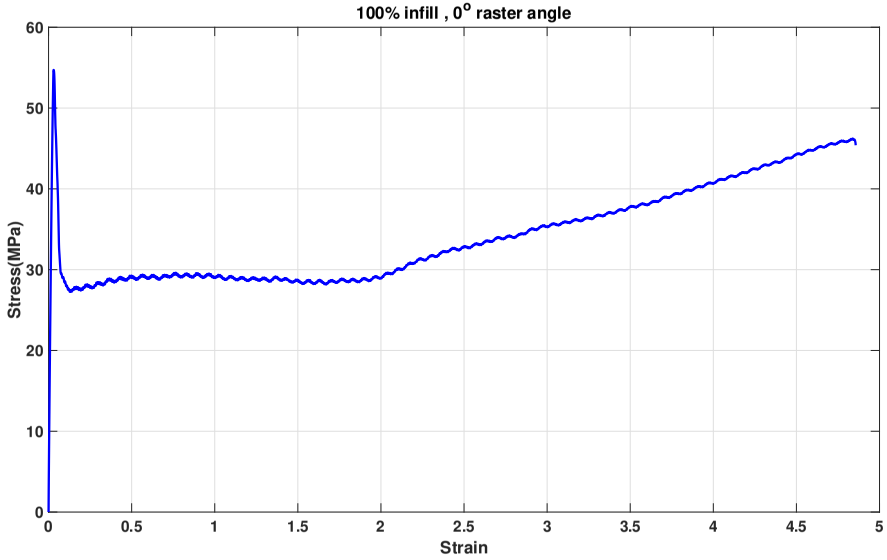

(e) 100% infill and 0° raster angle.

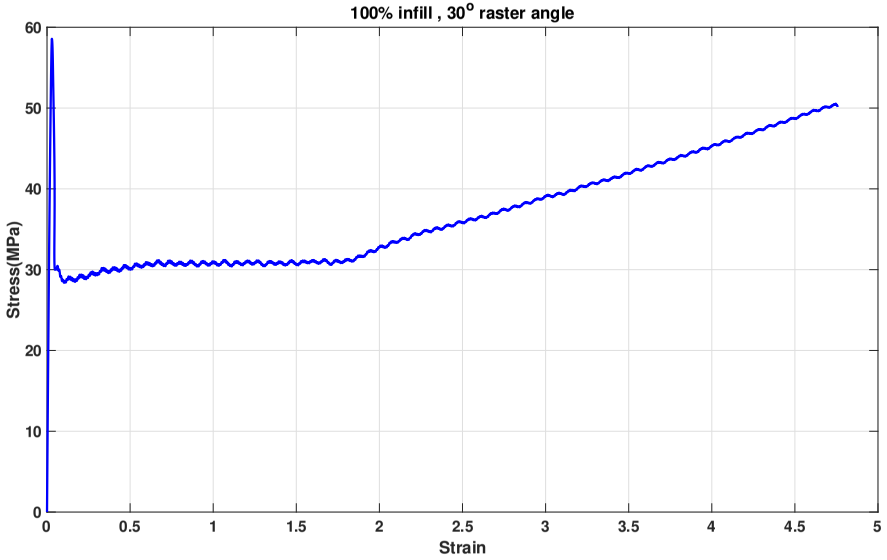

(f) 100% infill and 30° raster angle.

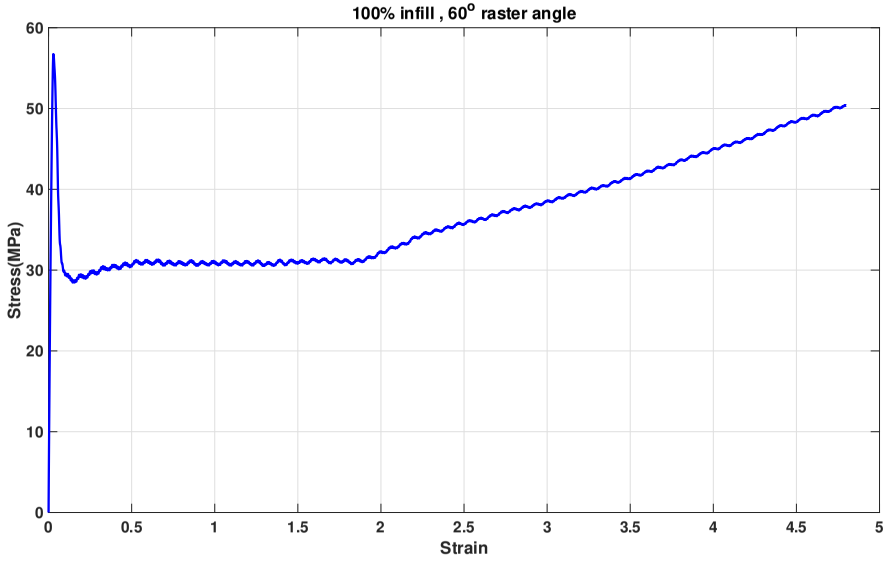

(g) 100% infill and 60° raster angle.

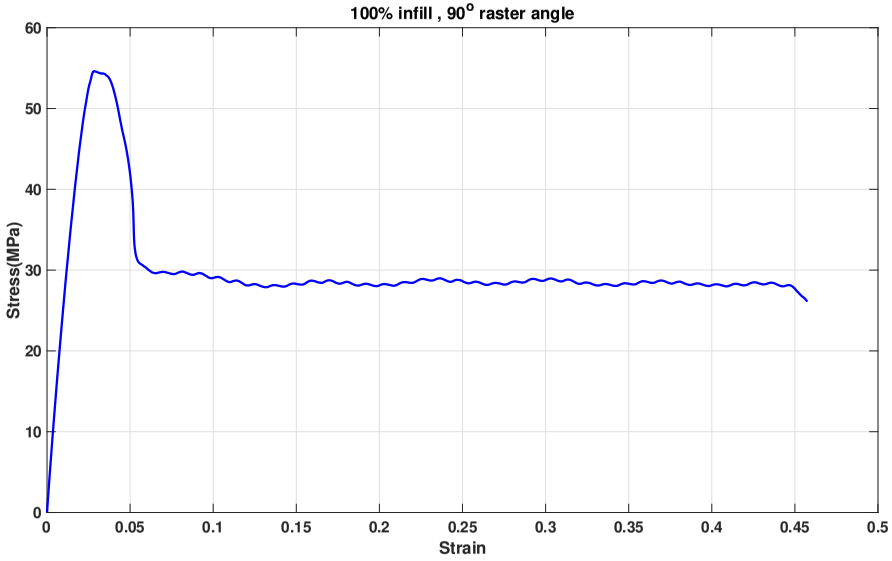

(h) 100% infill and 90° raster angle.

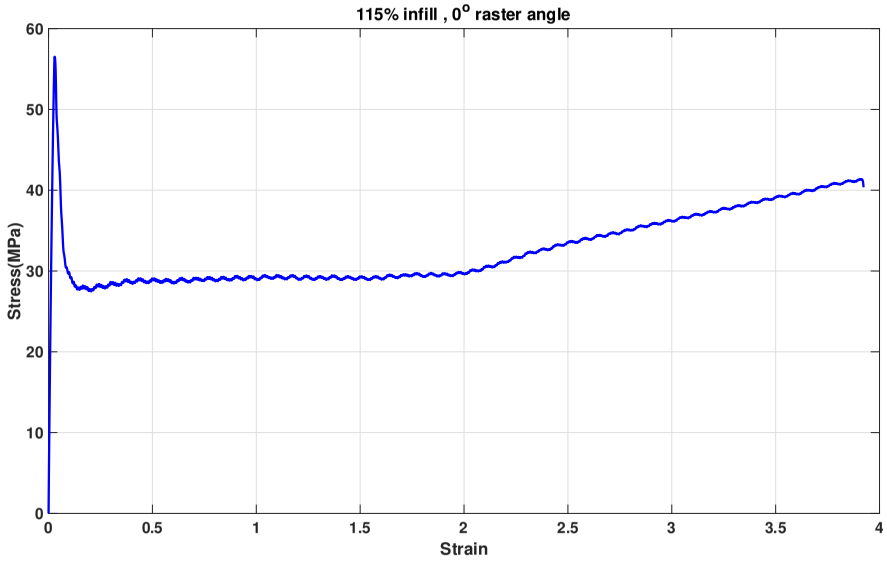

(i) 115% infill and 0° raster angle.

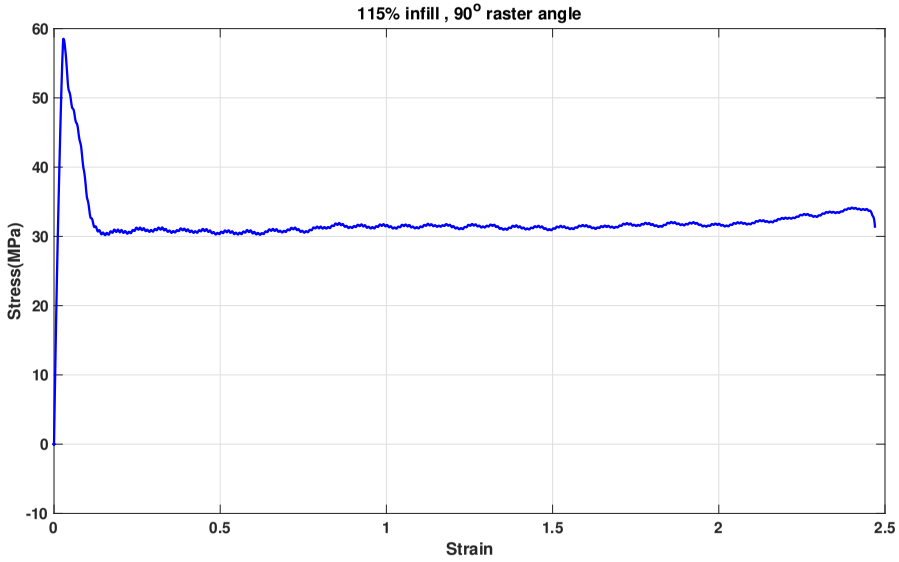

(j) 115% infill and 90° raster angle.

Figure A.1: Representative stress-strain curves of each raster angle and infill percentage used in this thesis.

Appendix B: Matlab program for calculation of equivalent elastic modulus based on CLPT model

```
function QQ1list = clpt1(input_l,input_j)

Nplies = 16;
j = input_j;
l = input_l;

k = 1 ;
for V = 0:1:90

    thetadt = [V -V V -V V -V V -V -V V -V V -V V -V V]; % V
       is the raster angle in degrees
    thetadb = fliplr(thetadt);
    h_ply  = 0.0001;           % SI units, meters
    h      = Nplies * h_ply ;

    for i = 1:Nplies
      zbar(i) = - (h + h_ply)/2 + i*h_ply;
    end




    A = zeros(3,3);
    B = zeros(3,3);
    D = zeros(3,3);
    ABD = zeros(6,6);
    ABDt = zeros(6,6);
    for i = 1:Nplies

        %Vm = 0.10902 ; %85% infill values
        %a = 0.11315 ; %85% infill values
```

```
31          Vm = 0.09590 ; %100% infill values
32          a = 0.74681 ; %100% infill values
33          b = a;
34          t = j*(1 - a);
35          theta  = thetadb(i);
36          if i <= 15
37          thetaT = thetadb(i+1);
38          else
39          thetaT = theta ;
40          end
41
42          nu = .42;
43          DT = abs(thetaT-theta);
44          a = a + t*(1-((DT-90)/90)^2);
45          Gf = 2.30778e9 /(2*(1+nu));
46          Ef = 2.30778e9;
47          Em = Ef*a;
48          Gm = Em/(2*(1+nu+(1/Vm)));
49          E1   = Ef*(1-Vm)+Em*Vm; % Pa
50          nu12 = nu+1 ;
51          E2   = ((1-Vm)/Ef+Vm/Em)^-1 ; % Pa
52          nu21 = nu12 * E2 / E1 ;
53
54          G12  = (Gf*Gm)/((Gm*(1 - Vm))+(Gf*Vm)) ; % Pa
55
56          % Q matrix
57          denom = 1 - nu12 * nu21 ;
58          Q11 = E1 / denom        ;
59          Q12 = nu12 * E2 / denom ;
60          Q22 = E2 / denom        ;
61          Q66 = G12               ;
62
63          Q = [ Q11 Q12 0; Q12 Q22 0; 0 0 Q66] ;
64          S=inv(Q) ;
65
66          m = cosd(theta) ;
67          n = sind(theta) ;
68          T = [ m^2 n^2 2*m*n; n^2 m^2 -2*m*n; -m*n m*n (m^2 -
                n^2)];
69          Qbar = inv(T) * Q * (inv(T))' ;
70          Sbar = inv(Qbar);
71
72
73          A = A + Qbar * h_ply;
74          B = B + Qbar * h_ply * zbar(i);
```

```
75          D = D + Qbar * (h_ply * zbar(i)^2  + h_ply^3 / 12);
76          ABD = [A(1,1:3),B(1,1:3);A(2,1:3),B(2,1:3);A(3,1:3),B
                (3,1:3);B(1,1:3),D(1,1:3);B(2,1:3),D(2,1:3);B
                (3,1:3),D(3,1:3)];
77          ABDt = inv(ABD);
78
79      end
80
81      QQ1list(k) = 1/(ABDt(1,1)*1.6e-3);
82      k = k+1;
83
84  end
85  end
```

Appendix C: Matlab Program for Generating Stress-Strain Curve From Machine Results

```

clear Stress
clear Strain
filename = ['1.TXT'];
j = 8;
    M = csvread(filename, 2 , 0);

Force = M(:,5);
Disp = M(:,9);
%%%%%%%%%%%%%%%%%%%%%%%%%%%%%%%%%%


m = find(Force(100:end)<10);
if isempty(m)
    min_m = max(size(Force));
    else
    min_m = (100+ min(m))-2;
end
mp = find(Force>0);
min_positive = min(mp);
Stress(min_positive:min_m ) = (Force(min_positive:min_m )-Force(min_positive))./(3.33*1.67);

[a,MaxF_i] = max(Force(1:(floor(min_m*.8))));

Disp = Disp - Disp(min_positive);


Strain(1:MaxF_i) = Disp(1:MaxF_i)./(5.556*7.62);
Strain(MaxF_i+1:min_m ) = ((Disp(MaxF_i+1:min_m)-Disp(MaxF_i))./7.62)+Strain(MaxF_i);
```

```
30
31   plot(Strain(min_positive:end),Stress(min_positive:end));
32   xlabel('Strain')
33   ylabel('Stress(MPa)')
34   title('85%-0')
35   grid on
36   hold on;
37
38  Toughness(j) = trapz(Strain(min_positive:MaxF_i)*10^6,Stress(
       min_positive:MaxF_i))
39  hold on
40  E = (Stress(floor(MaxF_i*.8))-Stress(floor(MaxF_i*.2)))/(
       Strain(floor(MaxF_i*.8))-Strain(floor(MaxF_i*.2)));
41  UTS = max(Stress((floor(min_m*.8)):end));
42  Yield = max(Stress(1:(floor(min_m*.9))));
43  Max_Elongation = (Disp(min_m)/9.54)*100;
44  Toughness = trapz(Strain(min_positive:end),Stress(
       min_positive:end));
45  Flow_Stress = mean(Stress(floor(MaxF_i*1.5):floor(MaxF_i*2.5)
       ));
46  Results(6,:) = [E UTS Yield Max_Elongation Toughness
       Flow_Stress]
47  hold on
```

Appendix D: CNC Machining G-Code

O0003 N10 G90 G94 G17 G49 G40 G80 N15 G20 N20 G28 G91 Z0. N25 G90 N40 G54 N60 G00 X0.4701 Y1.2499 N65 G00 G43 Z0.7874 H09 N70 G00 Z0.4331 N75 G01 Z0.1181 F13.1 N80 G01 Z-0.3543 N85 G01 Y0.5184 F10 N90 G02 X0.3995 Y0.3316 I-0.2825 N95 G03 X0.3451 Y0.1877 I0.1631 J-0.1439 N100 G01 Y-0.1875 N105 G03 X0.3995 Y-0.3314 I0.2175 N110 G02 X0.4701 Y-0.5182 I-0.2119 J-0.1868 N115 G01 Y-1.2499 N120 G02 X0.1876 Y-1.5324 I-0.2825 N125 G01 X-0.1876 N130 G02 X-0.4701 Y-1.2499 J0.2825 N135 G01 Y-0.5182 N140 G02 X-0.3995 Y-0.3314 I0.2825 N145 G03 X-0.3451 Y-0.1875 I-0.1631 J0.1439 N150 G01 Y0.1877 N155 G03 X-0.3995 Y0.3316 I-0.2175 N160 G02 X-0.4701 Y0.5184 I0.2119 J0.1868 N165 G01 Y1.2499 N170 G02 X-0.1876 Y1.5324 I0.2825 N175 G01 X0.1876 N180 G02 X0.4457 Y1.3646 J-0.2825 N185 G02 X0.4701 Y1.2499 I-0.2581 J-0.1147 F10 N190 G02 X0.4504 Y1.2204 I-0.032 F10 N195 G03 X0.4307 Y1.1909 I0.0123 J-0.0295 N200 G01 Y0.5184 N205 G02 X0.3699 Y0.3576 I-0.2431 N210 G03 X0.3057 Y0.1877 I0.1927 J-0.1699 N215 G01 Y-0.1875 N220 G03 X0.3699 Y-0.3574 I0.2569 N225 G02 X0.4307 Y-0.5182 I-0.1823 J-0.1608 N230 G01 Y-1.2499 N235 G02 X0.1876 Y-1.493 I-0.2431 N240 G01 X-0.1876 N245 G02 X-0.4307 Y-1.2499 J0.2431 N250 G01 Y-0.5182 N255 G02 X-0.3699 Y-0.3574 I0.2431 N260 G03 X-0.3057 Y-0.1875 I-0.1927 J0.1699 N265 G01 Y0.1877 N270 G03 X-0.3699 Y0.3576 I-0.2569 N275 G02 X-0.4307 Y0.5184 I0.1823 J0.1608 N280 G01 Y1.2499 N285 G02 X-0.1876 Y1.493 I0.2431 N290 G01 X0.1876 N295 G02 X0.4307 Y1.2499 J-0.2431 N300 G01 Y1.1909 N305 G02 X0.411 Y1.1613 I-0.032 N310 G03 X0.3913 Y1.1318 I0.0123 J-0.0295 N315 G01 Y0.5184 N320 G02 X0.3404 Y0.3836 I-0.2037 N325 G03 X0.2663 Y0.1877 I0.2222 J-0.196 N330 G01 Y-0.1875 N335 G03 X0.3404 Y-0.3835 I0.2963 N340 G02 X0.3913 Y-0.5182 I-0.1528 J-0.1348 N345 G01 Y-1.2499 N350 G02 X0.1876 Y-1.4536 I-0.2037 N355 G01 X-0.1876 N360 G02 X-0.3913 Y-1.2499 J0.2037 N365 G01 Y-0.5182 N370 G02 X-0.3404 Y-0.3835 I0.2037 N375 G03 X-0.2663 Y-0.1875 I-0.2222 J0.196 N380 G01 Y0.1877 N385 G03 X-0.3404 Y0.3836 I-0.2963 N390 G02 X-0.3913 Y0.5184 I0.1528 J0.1348 N395 G01 Y1.2499 N400 G02 X-0.1876 Y1.4536 I0.2037 N405 G01 X0.1876 N410 G02 X0.3913 Y1.2499 J-0.2037 N415 G01 Y1.1318 N420 G02 X0.3717 Y1.1023 I-0.032 N425 G03 X0.352 Y1.0727 I0.0123 J-0.0295 N430 G01 Y0.5184 N435 G02 X0.3109 Y0.4097 I-0.1644 N440 G03 X0.227 Y0.1877 I0.2517 J-0.222 N445 G01 Y-0.1875 N450 G03 X0.3109 Y-0.4095 I0.3356 N455 G02 X0.352 Y-0.5182 I-0.1233 J-0.1087 N460 G01 Y-1.2499 N465 G02 X0.1876 Y-1.4143 I-0.1644 N470 G01 X-0.1876 N475 G02 X-0.352 Y-1.2499 J0.1644 N480 G01 Y-0.5182 N485 G02 X-0.3109 Y-0.4095 I0.1644 N490 G03 X-0.227 Y-0.1875 I-0.2517 J0.222 N495 G01 Y0.1877 N500 G03 X-0.3109 Y0.4097 I-0.3356 N505 G02 X-0.352 Y0.5184 I0.1233 J0.1087 N510 G01 Y1.2499 N515 G02 X-0.1876 Y1.4143 I0.1644 N520 G01 X0.1876 N525 G02 X0.352 Y1.2499 J-0.1644 N530 G01 Y1.0727 N535 G02 X0.3323 Y1.0432 I-0.032 N540 G03 X0.3126 Y1.0137 I0.0123 J-0.0295 N545 G01 Y0.5184 N550 G02 X0.2813 Y0.4357 I-0.125 N555 G03 X0.1876 Y0.1877 I0.2812 J-0.248 N560 G01 Y-0.1875 N565 G03 X0.2813 Y-0.4355 I0.375 N570 G02 X0.3126 Y-0.5182 I-0.0938 J-0.0827 N575 G01 Y-1.2499 N580 G02 X0.1876 Y-1.3749

I-0.125 N585 G01 X-0.1876 N590 G02 X-0.3126 Y-1.2499 J0.125 N595 G01 Y-0.5182 N600 G02 X-0.2813 Y-0.4355 I0.125 N605 G03 X-0.1876 Y-0.1875 I-0.2813 J0.248 N610 G01 Y0.1877 N615 G03 X-0.2813 Y0.4357 I-0.375 N620 G02 X-0.3126 Y0.5184 I0.0937 J0.0827 N625 G01 Y1.2499 N630 G02 X-0.1876 Y1.3749 I0.125 N635 G01 X0.1876 N640 G02 X0.3126 Y1.2499 J-0.125 N645 G01 Y1.0137 N650 G00 Z0.7874 N670 G28 G91 Z0. N675 G28 X0. Y0. N680 M30